Modeling Desalination and Energy Performance of Membrane Capacitive Deionization

by

Xin Zhang, B.Sc., M.Sc.

A Dissertation

In

Chemical Engineering

Submitted to the Graduate Faculty
of Texas Tech University in
Partial Fulfillment of
the Requirements for
the Degree of

DOCTOR OF PHILOSOPHY

Approved

Dr. Danny Reible
Chair of Committee

Dr. Chau-Chyun Chen

Dr. Mahdi Malmali

Dr. Chongzheng Na

Dr. Mark Sheridan
Dean of the Graduate School

May, 2021

ACKNOWLEDGMENTS

First and foremost, I would like to express heartfelt appreciation to my advisor, Dr. Danny Reible, for always being patient and providing inspirational supervision and constant support through my PhD journey. Though he has a pretty busy schedule, he is always reachable by email when needed. He has given me enough flexibility and freedom to explore the research topics that I am interested in pursuing, encouraging me to see things from different aspects and training me to be an independent researcher. His infectious humor and positive lifestyle have inspired me to face the challenges in research and life with optimistic attitude.

I would also like to express my sincere gratitude to my committee members, Dr. Chau-Chyun Chen, Dr. Mahdi Malmali and Dr. Chongzheng Na for their willingness to serve in my committee. I appreciate the time and efforts they have put in and have learnt a lot from every academic discussion with them. I would like to acknowledge the Donovan Maddox Distinguished Engineering Chair Endowment sponsored by Maddox Foundation for financially supporting my research.

My endless gratitude goes to my colleagues in Dr. Reible's group for their help, support and company. Thanks Xiaolong for getting me familiar with CAPSIM codes. I appreciate Soraya for insightful discussions as a colleague, and for useful suggestions and support in my life as a friend. I enjoy the scientific discussions a lot with our desalination group members including Soraya, Tianyu, Ashkan, Khurshida and Karlo. Plus, I love spending time with my marvelous colleagues so much in our happy-hour

gatherings and all the amazing parties. I will cherish the precious memories and our friendship forever.

Additionally, I would love to thank my friends in Lubbock who always accompany me and make my spare time colorful. I thank my old friends at a distance for all the holiday greetings and wishes. A special thank goes to Shaokun, who has provided continuous care, encouragement and support for me even from thousands of miles away throughout my graduate study.

Finally, I am immeasurably grateful for my dear parents, who always believe in me and want the best for me. Without their unconditional love, sacrifice, tolerance, and support, I would not be able to complete all these hard works and finally reach to an end. I dedicate my dissertation to my beloved parents!

TABLE OF CONTENTS

ABSTRACT

The fresh water crisis due to population increase, climate change and pollution encourages the development of alternative water sources. A particularly attractive alternative is brackish groundwaters which are abundant and contain less salt than seawater. Capacitive deionization (CDI) is an emerging desalination technique for removing salts from low-salinity brackish water and is scalable and potentially applicable to distributed water treatment systems. By introducing a pair of ion-exchange membranes (IEMs) into conventional CDI to form membrane CDI (MCDI), the desalination rate, salt removal efficiency, and energy efficiency can be improved. This dissertation develops a physics-based two-dimensional process model for depicting ion transport and adsorption dynamics in MCDI, and uses that model to evaluate the effects of cell geometry, cell cycle time, and operating conditions on salt removal efficiency, energy consumption, and selective ion removal.

A comprehensive CDI process model incorporating modified Donnan (mD) theory based CDI models was proposed to capture the effects of electrode surface charges, Faradaic reactions, solution pH, and various cell architectures on desalination performance and energy behaviors.

A fully coupled two-dimension MCDI process model was proposed by incorporating the hydraulic dispersion effects in the channel and co-ion penetration in the IEM. This model was quantitatively compared to available data and applied to evaluating the differences between MCDI over CDI in rate of desalination and ion adsorption capacity.

The effects of cell geometry, cell cycle mode and operating conditions on salt removal efficiency were explored and led to a conclusion that use of an IEM, increasing applied voltage, decreasing flow rate, prolonging electrode length and thickness, reducing dispersivity and channel thickness could enhance salt removal efficiency. An operating approach designed to maximize salt removal efficiency by rapidly switching between adsorption and desorption cycles (cut-off mode) was shown to have significant advantages compared to operating the system to equilibrium.

The MCDI process model was applied to evaluating the energy performance of constant voltage (CV) mode MCDI under cut-off and equilibrium cycle modes. Cut-off mode was generally found to achieve higher specific energy consumption (SEC) and thermodynamic energy efficiency (TEE) compared to equilibrium mode. Pump losses were dominant in equilibrium mode especially with long cell length, while external resistive losses were dominant under high water recovery in cut-off mode. Energy storage in the CDI cell during desalination accounted for 20-40% of SEC. TEE decreased with increasing water productivity, and was competitive with RO for desalinating near-fresh water at high water recovery. Overall, constant voltage (CV) mode MCDI was more energy efficient under moderate water recovery compared to constant current (CC) mode MCDI.

The MCDI process model was extended to capture ion exclusion effects and to predict ion selectivity in a multi-ion solution. Trade-offs between ion selectivity and ion removal efficiency were evaluated. Overall, MCDI was found to be feasible for partially

softening industrial cooling tower blowdown water and slightly softening domestic tap water with moderate water recovery with low energy consumption.

LIST OF TABLES

LIST OF FIGURES

CHAPTER 1

INTRODUCTION

1.1. Overview

The potential disruptions caused by population growth, a changing climate and environmental pollution suggests that water supply cannot meet increasing demand for freshwater [1]. This growing water crisis facilitates the development of desalinating abundant saline waters [2]. Capacitive deionization (CDI) is an emerging desalination technique with the advantages of easy assembling, portability, potential for selective removal of ions and partial desalination, and potentially low energy consumption for desalinating low concentration brackish water [3, 4].

1.1.1 CDI and its variants

1.1.1.1 CDI

Conventional CDI is assembled by separating a pair of porous capacitive electrodes with a porous spacer to enhance the mixing of the feed solution [3]. CDI involves alternating desalination and regeneration steps. During desalination (Figure 1.1), ions are attracted toward the oppositely charged electrodes and get temporarily adsorbed into the electric double layer (EDL), which forms near the surface of the electrode. Ion adsorption in a conventional CDI is similar to that in a charging capacitor. The porous electrode is usually modeled as containing macropores for ion transport, and micropores for ion adsorption [5, 6]. The EDL is expected to develop in the micropores. During regeneration, the electrode pair is either short-circuited or reversely charged to repel the

previously stored ions from the electrode back into the channel and restore the adsorption capacity of the electrode. The fractional water recovery can be controlled by the cycle times and the flow rate during regeneration compared to that during adsorption.

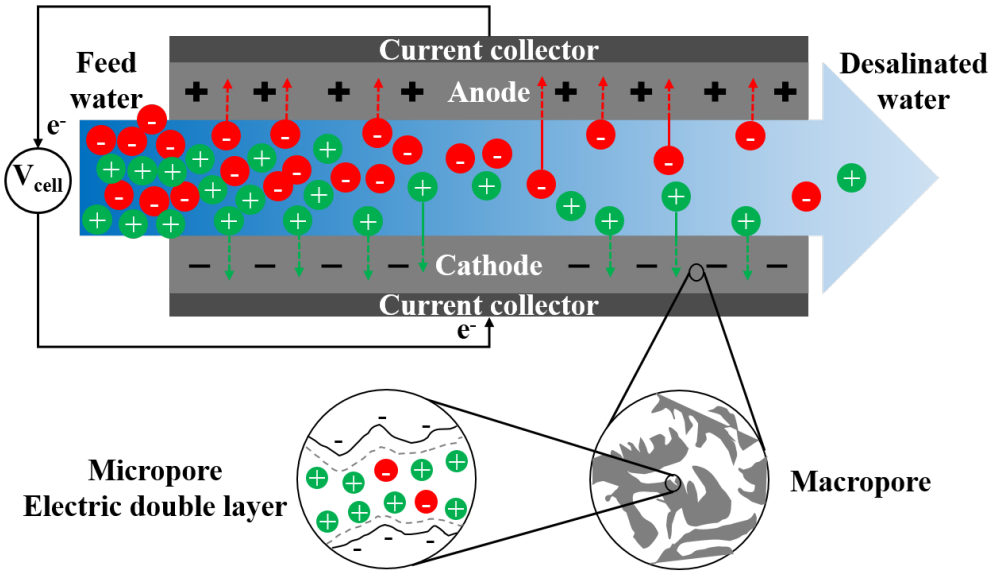

Figure 1.1. Schematic of desalination step in a conventional CDI [7].

1.1.1.2 MCDI

Membrane CDI (MCDI) includes ion-exchange membrane (IEM) to cover each electrode [8]. A cation-exchange membrane (CEM) is attached to cathode (defined as the electrode carrying extra electrons during desalination), while an anion-exchange membrane (AEM) is attached to the anode (Figure 1.2). IEM keeps co-ions (ions with the same sign as the fixed charges on the IEM) from leaving the electrode during desalination, and prevents co-ions from penetrating the IEM and entering the electrode

during regeneration. Hence, the adsorption capacity in MCDI is higher compared to conventional CDI. The relatively high fixed charges on the IEM also speeds counter-ion transport, improving salt removal rate of MCDI compared to conventional CDI [9].

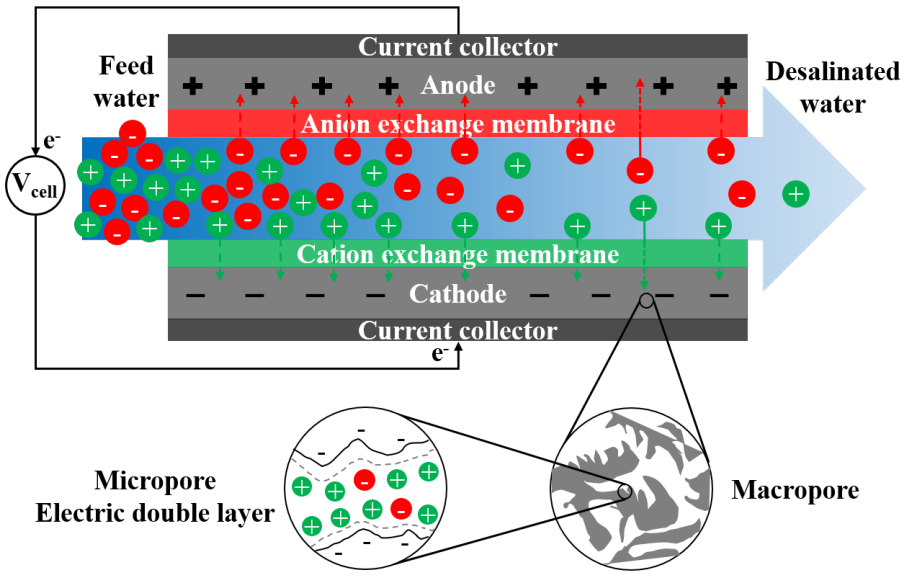

Figure 1.2. Schematic of desalination step in MCDI [7].

1.1.1.3 Membranes in MCDI

Commercial IEMs that are mechanically stable, resist corrosion and possessing high permselectivity were first used in MCDI [10]. Since IEMs in MCDI do not have to be free-standing, low resistance membranes such as thin IEMs and electrode-IEM composites have been successively developed and used to achieve a relatively high energy efficiency [10]. Functional IEMs, such as monovalent permselective IEMs, can be introduced in MCDI to preferentially remove lithium [11] and fluoride [12], or generate a solution mainly containing divalent-ions [13].

Fabrication techniques for relatively thin IEMs used in MCDI include casting [14-16], and pore-filling polymerization [17-21]. Pore-filling techniques were found to improve mechanical and chemical stability of the produced IEMs [17-20]. The electrode-IEM composites can be synthesized by functional solutions' immersing or spraying, in situ polymerization and chemical doping of the electrode [22].

Future research about IEM synthesis for MCDI should address the current challenges including the high cost of the polymeric IEMs from the multiple reagents involved in the synthetic process and the complicated synthesis and modification process [23]. Modifications to increase the lifetime of the IEM should also be investigated.

1.1.1.4 Key developments of CDI elements and architectures

Since the born of CDI in 1960s [24], various electrode and IEM materials and cell architectures have been explored (Figure 1.3).

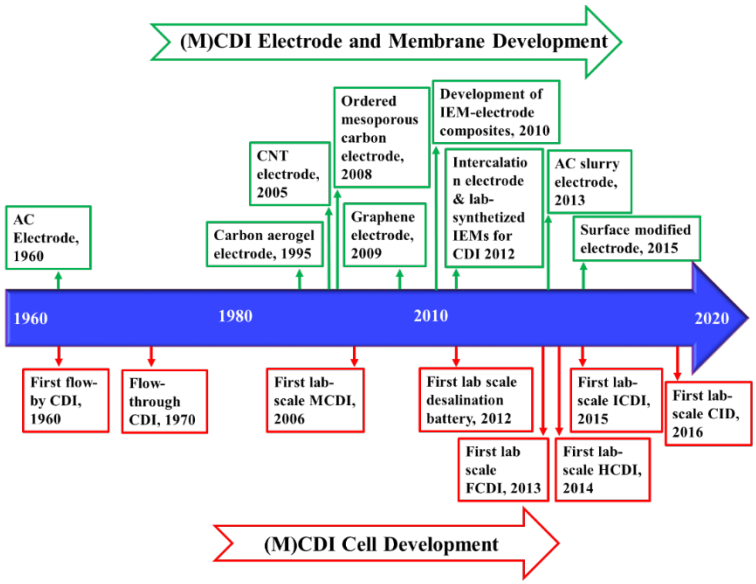

Figure 1.3. Timeline of the major developments of various electrode and IEM materials and cell architectures [7].

1.1.1.5 Alternative CDI architectures

Besides conventional CDI and MCDI, there are other alternative CDI architectures including flow-through CDI, inverted CDI (I-CDI), flow-electrode CDI (FCDI), and intercalation electrodes assembled CDI including desalination battery, hybrid CDI (HCDI), and cation intercalation desalination (CID) (Figure 1.4) [25]. These variants of CDI improve desalination performance and enhance energy efficiency, broadening the applications of CDI. Specific features, mechanisms, advantages, disadvantages and recent advances of each variant are described in the following paragraphs.

Flow-through CDI (Figure 1.4 (a)) is operated by pumping the flowing solution through the electrode pair. Hence, the electrode macropores serve as a transport path for both ions and flowing solution. Since the flow path is no longer limited to the spacer channel,

the thickness of the spacer can be narrowed to enable building compact cells, which enhances the salt removal rate and expands salt adsorption capacity [25]. However, due to the small permeability of the electrode, the pressure drop through the electrode increases and thus makes flow-through CDI less energy efficient [26]. Oxidation reactions also increase electrode degradation requiring pretreatment, such as nitrogen purging, of the feed water [25]. Recent advances enlarging electrode macropores with laser perforation can significantly reduce the hydraulic losses [26].

In I-CDI (Figure 1.4 (b)), positive and negative functional groups are modified on the surface of the electrode pair, respectively. Hence ion adsorption in I-CDI occurs without charging and desorption occurs with charging. Anode oxidation is inhibited in I-CDI, leading to a relatively long lifetime of the electrode [27]. However, the small range of applied voltage limits the adsorption capacity of the electrode [26]. By employing an amine-treated cathode [28], or introducing IEMs between the electrode pair and the spacer-filled channel to form inverted MCDI (I-MCDI) [29, 30], the salt removal degree and the energy efficiency can be enhanced.

FCDI (Figure 1.4 (c)) employs a flowing activated carbon (AC) slurry in the electrode channel to replace the fixed electrode film used in conventional CDI. An electrolyte in the electrode channel also serves as an ion storage site. FCDI significantly enhances cell adsorption capacity [25], enables continuous production of desalinated water [31], and expands the application scope toward medium to high salinity brackish water desalination [32]. However, the conductivity of the electrode channel needs to be improved to reduce the corresponding resistive losses [33]. By increasing the content of

AC in the flowing slurry [34], introducing conductive additives into the AC slurry [35-39], and increasing the flow rate of the flowing electrode [40], the conductivity of the electrode channel has been significantly improved.

Intercalation electrodes were first used as a desalination battery (Figure 1.4 (d)) by replacing the capacitive electrode in a conventional CDI. A hybrid CDI (Figure 1.4 (e)) was then developed by replacing the anion intercalation electrode in a desalination battery with a capacitive anode attached with an AEM. This is to avoid the relatively low conductivity of the anion intercalation electrodes, which is usually composed of Ag/AgCl, Bi/BiOCl or MnO_2 [41, 42]. Later on, CID (Figure 1.4 (f)) was developed by using cation intercalation electrodes as both cathode and anode, and using an AEM in-between to enable a simultaneous production of both dilute and concentrate streams. Adsorption in intercalation electrodes assembled CDI is mainly attributed to reversible Faradaic reactions, with a small amount of capacitive adsorption in EDL. Intercalation electrode improves adsorption capacity [42] and enables adsorption of specific ions [42]. However, the slow adsorption and desorption processes together with a relatively high capital cost limit applications [25]. By employing conductive additives into the intercalation electrodes, the salt removal rate can be improved [43]. By replacing the capacitive electrodes with intercalation electrodes in I-CDI, we can achieve a long lifetime of the electrodes and a high adsorption capacity simultaneously [44].

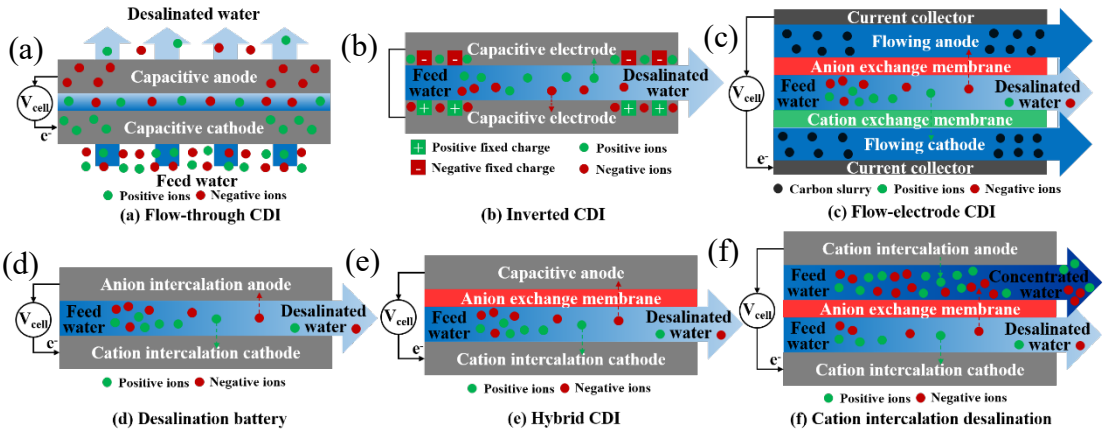

Figure 1.4. Alternative CDI architectures including: **(a)** flow-through CDI; **(b)** I-CDI; **(c)** FCDI; **(d)** desalination battery; **(e)** HCDI; **(f)** CID [7].

1.1.2 (M)CDI charging modes

(M)CDI can be classified into constant voltage (CV) mode and constant current (CC) mode based on the charging mode [45-47]. In a single-pass flow mode [4], a lower concentration is reached faster in CV mode but the effluent concentration returns to the feed water concentration as electrode saturation is approached. A hybrid CV-CC mode was proposed by Saleem et al. [48] by reaching a relatively low concentration first under CV mode, and then changing to CC mode to achieve a stable effluent concentration. The salt removal efficiency of this hybrid CC-CV mode was found to be larger than a single CC or CV mode when treating the same feed water.

1.1.3 (M)CDI applications

(M)CDI is energy efficient for desalinating brackish water below 3000 ppm for industrial, agricultural, and municipal water usage [3, 49, 50]. (M)CDI can produce

tunable effluents by adjusting the applied voltage or current, and hence is feasible for partial desalination. As (M)CDI possesses relatively high energy efficiency for treating near-fresh waters, (M)CDI can also be used for producing ultrapure water from tap water [48, 51, 52]. Due to the preferential adsorption toward ions with higher valences, MCDI can also be used for softening brackish waters [52], selective removal of heavy metal ions [52, 53], and recovery of nutrient ions [52]. In addition, CDI can be used for water disinfection by attaching antibacterial functional groups onto the electrode surface or operating CDI under high voltage to trigger Faradaic reactions to produce peroxide and chlorine [53].

MCDI has also been proposed to treat RO permeate for higher water recovery and a lower energy input [54]. Hybrid systems containing multiple desalination techniques such as RO-(M)CDI [52] and RO-MCDI-RED [55] have been developed to improve desalination performance and reduce energy consumption at the same time.

1.2 CDI performance indicators

1.2.1 Desalination performance

Desalination performance depends on the capacitance of the electrode, physiochemical properties of cell elements, applied voltage or current, flow rate and composition of the feed water, operating mode and cell architecture [56]. Desalination performance indicators include charge efficiency, adsorption capacity, desalination rate, and salt removal efficiency.

Charge efficiency is defined as the ratio of removed ions to transferred charges at equilibrium [57]. Charge efficiency can be reduced by co-ion repulsion together with irreversible Faradaic reactions [58]. By modifying the electrode surface with functional groups (see I-CDI), attaching IEM in front of the electrodes (see MCDI and FCDI) and employing intercalation electrodes (see intercalation electrodes assembled CDI), co-ion repulsion effects can be mitigated. Adsorption capacity is closely related to the physiochemical properties of the electrode and the operating conditions such as the charging mode, regeneration mode, and cycle mode. Those poorly interconnected pores and closed pores increase the ion transport resistance and reduce the accessible surface areas of electrodes, affecting the adsorption capacity [59]. The effective surface area of electrodes lies in micropores in the size range of 0.8-2 nm [60]. Due to the usage of fixed electrode film in conventional CDI and MCDI, the adsorption capacity is relatively low. However, by using flowing electrodes in FCDI or assembling intercalation electrodes in CDI, the adsorption capacity is improved. Desalination rate and salt removal efficiency both depend on the feed water quality, operating conditions and the properties of the electrode including the effective surface area, pore geometry, conductivity, hydrophilicity, and surface functional groups [61].

1.2.2 Fouling and scaling issues

1.2.2.1 Fouling and scaling in CDI

Fouling in CDI can cause electrode degradation, increase system resistance, reduce electrode capacitance, and decrease cell stability. The mechanisms of organic fouling in

CDI include electrode pore blocking by the foulants, decrease of effective adsorption sites due to the competitive adsorption between foulants and ions, hindered ion diffusion in electrode, and accelerated degradation of intercalation electrodes [62-66].

Scaling is less severe than fouling in CDI. Desalination performance is almost independent of the existence of hardness ions such as calcium and magnesium [62]. Since silica does not serve as charge carrier, it cannot be adsorbed during CDI operation, causing no scaling issues. However, ferric ions can deposit onto the electrode surface in the form of iron hydroxide, aggregating scaling issues in CDI [63, 64].

1.2.2.2 Strategies to address fouling and scaling issues in CDI

Appropriate electrode modification techniques such as producing photocatalytic (TiO_2) electrode composites [67] and attaching zwitterionic polymers [68] or ultrafiltration (UF) membranes [69] onto the electrode surface, to enhance anti-fouling ability and hydrophilicity, and prevent foulants from entering the electrode [68].

Hydraulic cleaning, acid cleaning and alkali cleaning have been used to remove foulants and scales formed on the electrode. Specifically, acid cleaning removes more of the accumulated scale, while alkali cleaning is more useful for removing organic foulants [62, 63]. However, the alkali solution can degrade electrodes especially those with a polyvinylidene difluoride (PVDF) binder, resulted in loss of adsorption capacity, aggravated Faradaic reactions and shorted lifetime of electrode [65]. Hence, proper pretreatment of the feed water containing organic compounds is necessary.

1.2.2.3 Fouling and scaling in MCDI

Due to the protection by the IEM in MCDI, the fouling and scaling issues are less than observed with CDI [65]. However, during long-term operations, organic foulants may slowly penetrate and clog the IEM, resulting in reduced salt adsorption capacity and increased energy consumption [70]. Although scaling is not an issue in MCDI, the existence of mineral ions can aggravate organic fouling in some cases [70, 71].

1.2.2.4 Strategies to address fouling and scaling issues in MCDI

By properly modifying the surface of IEM [72], applying reversed polarity on the electrode pair during regeneration [65], and using mild alkali agent for IEM cleaning [70, 72], fouling can be alleviated. Due to the negative charges on the foulants, fouling on AEM is much more severe compared to the CEM [65]. However, the weak tolerance of high pH environment brings the danger of membrane degradation when using alkali cleaning agents. Hence, proper pretreatment of feed water with high content of organic compounds is suggested for MCDI.

1.2.3 Energy and cost performance

1.2.3.1 Energy consumption

Energy consumption of (M)CDI depends on feed water salinity, water throughput, salt removal efficiency, flow mode, and charging mode [73, 74]. MCDI is more energy efficient than CDI under the same operating conditions [75, 76]. Energy consumption of CC mode is generally lower than CV mode [45-47].

Resistive losses become dominant when CDI is charged under relatively high current [77, 78]. By employing appropriate modification of the electrode [79, 80], using low-resistance IEMs or electrode-IEM composites, and applying conductive spacers such as mosaic membranes [81], granular activated carbons (GACs) [82], or ion-exchange resins [83], system resistance can be reduced. Inversely, parasitic losses from irreversible Faradaic reactions become dominant when CDI is charged under relatively low current due to the relatively long time under the relatively high potential drop range of the electrode pair [77, 78].

Compared to conventional desalination techniques such as reverse osmosis (RO) and electrodialysis (ED), (M)CDI consumes more energy under similar conditions [84-86]. However, with an intermittent operation in MCDI, a high water recovery was achieved without extra energy input, leading to an overall lower energy consumption of MCDI compared to RO [87].

Thermodynamic energy efficiency (TEE) represents the fraction of the reversible specific energy consumption (SEC) achieved by an ion separation process [88]. TEE has been used as a performance indicator to compare the energy efficiency between different desalination techniques. Although conventional CDI and MCDI can barely reach a TEE higher than 10%, FCDI and intercalation electrodes assembled CDI can reach up to 30% of TEE under low salinity of brackish water (1000-2000 ppm), which is comparable to RO and ED [88, 89]. TEE of CDI and its variants can be further improved by reducing system resistance, modifying cell architecture, optimizing

operating conditions and employing energy recovery devices (ERDs) to make CDI more competitive.

1.2.3.2 Energy recovery

Part of the input energy is temporarily stored in EDL as ions are adsorbed during desalination. This energy can be partially recovered during regeneration via a buck-boost converter into a supercapacitor or another cell [90]. Reverse electrodialysis (RED) [91-93] and pressure-retarded osmosis (PRO) [94] have also been theoretically implemented as ERDs in CDI. Energy recovery depends on operating conditions, charging mode, feed water quality, cell hydrodynamics, and capacitance of the electrodes [95-99]. The available energy recovery of CC mode is larger than that of CV mode [100]. Energy recovery is affected under relatively high current or voltage during regeneration due to the higher external resistive losses [95, 96]. Energy recovery can be improved by increasing the concentration of feed water and reducing the thickness of the channel due to the relatively low resistive losses [98]. The greater salt adsorption capacity of electrodes leads to more adsorbed ions, which in turn results in more recoverable energy [97]. ERDs have been widely employed in FCDI as well [101]. By increasing the content of the flowing electrodes, employing conductive additives, and enhancing the electrolyte concentration in the electrode channel, energy recovery in FCDI can be improved [102, 103].

1.2.3.3 Cost and cell lifetime

The capital cost of (M)CDI is less than RO, although the overall cost of RO is lower [104]. However, with length operating periods and keeping the salinity of feed water below 2000 ppm, (M)CDI can be comparable to RO [104]. If IEMs can be reduced in cost to below \$20/m^2 and prolonging the lifetime of MCDI, MCDI can be economically competitive compared to CDI [105].

The reported lifetime of IEM is between 5-8 years [106], and the electrode is between 0.5-10 years [104, 107]. Appropriate modification of cell elements, such as reducing the acidity on the electrode surface [108] and employing intercalation electrodes [109] can improve the longevity of (M)CDI. Proper pretreatment of feed water to remove foulants can also increase cell lifetime.

1.3 CDI modeling efforts

Simulation work of CDI is of vital importance for understanding the intrinsic mechanisms of electrosorption and optimizing cell design and operation [4]. The critical point lies in accurately simulating the key processes of CDI including ion adsorption in electrode and ion transport throughout the cell. Ion adsorption occurs together with the development of EDL, which has been simulated using a Helmholtz model [110], Gouy-Chapman-Stern (GCS) model [111], and modified Donnan (mD) model [6]. Macroscopic porous electrode (MPE) theory [112-114] has been developed by converting the variables to be volume-averaged to avoid dealing with the complex microstructure of electrode. A macroscopic transport equation coupling the adsorption

rate as a sink term is applicable for simulating ion transport and adsorption dynamics in electrode. Ion transport in the channel and IEM (if applied) can also be simulated by macroscopic transport equations.

The mD theory based CDI models have been applied to simulating the transient effluent concentration curves, dynamic external current or voltage curves in CV and CC modes, and the accumulated potential in EDL. These models can be used to evaluate the performance metrics including average salt adsorption rate, salt removal efficiency, salt adsorption capacity, charge efficiency, SEC, energy recovery and TEE. The mD theory based CDI models can also simulate the dynamics of capacitive mixing, which is an inverse process of CDI and can be employed for recovering energy from salinity gradients at estuary entry [115, 116]. With the aid of CDI models, the optimal electrode geometry, cell architecture, and operating conditions can be obtained efficiently.

1.4 Dissertation content

More research is needed to address the challenges of MCDI and optimize cell design and operating conditions for improving the competitiveness of MCDI. To investigate the abovementioned desalination and energy performance indicators in a quick, cheap and efficient way, mD theory based models are developed and applied to evaluating MCDI process in this work.

The objectives of this research include: 1) Evaluating the merits, drawbacks, and applications of mD theory based CDI models; 2) Incorporating hydraulic dispersion effects and ion exclusion effects in a fully coupled two-dimension MCDI process model;

3) Exploring the superiority of MCDI over CDI in desalination rate and salt removal efficiency under varying cycle modes; 4) Evaluating energy behavior, ion selectivity and water softening ability of MCDI.

In Chapter 2, a comprehensive review of CDI models is conducted by: 1) proposing a CDI process model incorporating the published extensions of mD theory based CDI models for capturing the effects of functionalized electrode, Faradaic reactions and various CDI architectures such as conventional CDI, MCDI, flow-through CDI, FCDI and I-CDI; 2) Introducing the development and key equations of other models that have been employed for CDI simulation; 3) Comparing the four types of CDI models studied regarding the capture of electrosorption mechanisms and Faradaic reactions, calculation simplicity and application scope.

In Chapter 3, a fully-coupled two-dimension MCDI process model is proposed by incorporating the hydraulic dispersion effects in a spacer-filled channel and considering co-ion penetration through the IEM. This model is quantitatively validated and is employed to show the advantages of MCDI over CDI in desalination rate, salt adsorption capacity and (maximal) salt removal efficiency. A cycle mode termed cut-off mode [9] is proposed for achieving the maximal salt removal efficiency in a cycle. Sensitivity analyses are conducted to evaluate the effects of feed water concentration, cell geometry and operating conditions such as flow rate and applied voltage.

In Chapter 4, the MCDI process model developed in Chapter 3 is employed to evaluate the SEC and TEE of CV mode MCDI under both cut-off and equilibrium modes, and

compared to that of CC mode MCDI. Trade-offs between water recovery and salt removal efficiency are investigated. The highlight of this work lies in including pump energy into the SEC, and intuitively comparing the SEC of pump to that of other components. The energy storage in EDL during desalination is calculated.

In Chapter 5, the MCDI process model developed in Chapter 3 is extended to incorporate ion exclusion effects to better depict ion selectivity in multicomponent solution, especially when under the same initial concentration and valence of different ions. This extended process model is employed to explore trade-offs between the selectivity and removal efficiency of calcium ions in a calcium-sodium-chloride solution under varying feed water concentration ratios of sodium to calcium and varying applied voltage. This extended model is then applied to evaluating the selectivity and removal efficiency of hardness ions, and SEC with industrial cooling tower blowdown water or domestic tap water to analyze the real water softening feasibility of MCDI.

In Chapter 6, the key conclusions are summarized and the future research trend of CDI simulation works are proposed.

1.5 References

[1] M. M. Mekonnen and A. Y. Hoekstra, "Four billion people facing severe water scarcity," *Science advances,* vol. 2, no. 2, p. e1500323, 2016.

[2] M. Elimelech and W. A. Phillip, "The future of seawater desalination: energy, technology, and the environment," *science,* vol. 333, no. 6043, pp. 712-717, 2011.

[3] M. Suss, S. Porada, X. Sun, P. Biesheuvel, J. Yoon, and V. Presser, "Water desalination via capacitive deionization: what is it and what can we expect from it?," *Energy & Environmental Science,* vol. 8, no. 8, pp. 2296-2319, 2015.

[4] S. Porada, R. Zhao, A. Van Der Wal, V. Presser, and P. Biesheuvel, "Review on the science and technology of water desalination by capacitive deionization," *Progress in Materials Science,* vol. 58, no. 8, pp. 1388-1442, 2013.

[5] S. Porada, L. Borchardt, M. Oschatz, M. Bryjak, J. Atchison, K. Keesman, S. Kaskel, P. Biesheuvel, and V. Presser, "Direct prediction of the desalination performance of porous carbon electrodes for capacitive deionization," *Energy & Environmental Science,* vol. 6, no. 12, pp. 3700-3712, 2013.

[6] P. Biesheuvel, R. Zhao, S. Porada, and A. Van der Wal, "Theory of membrane capacitive deionization including the effect of the electrode pore space," *Journal of colloid and interface science,* vol. 360, no. 1, pp. 239-248, 2011.

[7] S. Honarparvar, X. Zhang, T. Chen, A. Alborzi, K. Afroz, and D. Reible, "Frontiers of Membrane Desalination Processes for Brackish Water Treatment: A Review," *Membranes,* vol. 11, no. 4, p. 246, 2021.

[8] P. Biesheuvel and A. Van der Wal, "Membrane capacitive deionization," *Journal of Membrane Science,* vol. 346, no. 2, pp. 256-262, 2010.

[9] X. Zhang and D. Reible, "Exploring the Function of Ion-Exchange Membrane in Membrane Capacitive Deionization via a Fully Coupled Two-Dimensional Process Model," *Processes,* vol. 8, no. 10, p. 1312, 2020.

[10] A. Hassanvand, K. Wei, S. Talebi, G. Q. Chen, and S. E. Kentish, "The role of ion exchange membranes in membrane capacitive deionisation," *Membranes,* vol. 7, no. 3, p. 54, 2017.

[11] W. Shi, X. Liu, C. Ye, X. Cao, C. Gao, and J. Shen, "Efficient lithium extraction by membrane capacitive deionization incorporated with monovalent selective cation exchange membrane," *Separation and Purification Technology,* vol. 210, pp. 885-890, 2019.

[12] J. Pan, Y. Zheng, J. Ding, C. Gao, B. Van der Bruggen, and J. Shen, "Fluoride removal from water by membrane capacitive deionization with a monovalent anion selective membrane," *Industrial & Engineering Chemistry Research,* vol. 57, no. 20, pp. 7048-7053, 2018.

[13] J. Choi, H. Lee, and S. Hong, "Capacitive deionization (CDI) integrated with monovalent cation selective membrane for producing divalent cation-rich solution," *Desalination,* vol. 400, pp. 38-46, 2016.

[14] K. W. Kang, C. W. Hwang, and T. S. Hwang, "Synthesis and properties of sodium vinylbenzene sulfonate-grafted poly (vinylidene fluoride) cation exchange membranes for membrane capacitive deionization process," *Macromolecular Research,* vol. 23, no. 12, pp. 1126-1133, 2015.

[15] K. S. Jeong, W. C. Hwang, and T. S. Hwang, "Synthesis of an aminated poly (vinylidene fluride-g-4-vinyl benzyl chloride) anion exchange membrane for membrane capacitive deionization (MCDI)," *Journal of membrane science,* vol. 495, pp. 316-321, 2015.

[16] A. Jain, C. Weathers, J. Kim, M. D. Meyer, W. S. Walker, Q. Li, and R. Verduzco, "Self assembled, sulfonated pentablock copolymer cation exchange coatings for membrane capacitive deionization," *Molecular Systems Design & Engineering,* vol. 4, no. 2, pp. 348-356, 2019.

[17] Q. Qiu, J.-H. Cha, Y.-W. Choi, J.-H. Choi, J. Shin, and Y.-S. Lee, "Preparation of stable polyethylene membranes filled with crosslinked sulfonated polystyrene for membrane capacitive deionization by γ-irradiation," *Macromolecular Research,* vol. 25, no. 1, pp. 92-95, 2017.

[18] Q. Qiu, J.-H. Cha, Y.-W. Choi, J.-H. Choi, J. Shin, and Y.-S. Lee, "Preparation of polyethylene membranes filled with crosslinked sulfonated polystyrene for

cation exchange and transport in membrane capacitive deionization process," *Desalination,* vol. 417, pp. 87-93, 2017.

[19] D.-H. Kim, Y.-E. Choi, J.-S. Park, and M.-S. Kang, "Capacitive deionization employing pore-filled cation-exchange membranes for energy-efficient removal of multivalent cations," *Electrochimica Acta,* vol. 295, pp. 164-172, 2019.

[20] O. ul Haq, J.-H. Choi, and Y.-S. Lee, "Anion-exchange membrane for membrane capacitive deionization prepared via pore-filling polymerization in a porous polyethylene supporting membrane," *Reactive and Functional Polymers,* vol. 132, pp. 36-42, 2018.

[21] J. Ran, L. Wu, Y. He, Z. Yang, Y. Wang, C. Jiang, L. Ge, E. Bakangura, and T. Xu, "Ion exchange membranes: New developments and applications," *Journal of Membrane Science,* vol. 522, pp. 267-291, 2017.

[22] M. S. Gaikwad and C. Balomajumder, "Polymer coated capacitive deionization electrode for desalination: a mini review," *Electrochemical Energy Technology,* vol. 2, no. 1, 2016.

[23] R. McNair, G. Szekely, and R. A. Dryfe, "Ion-Exchange Materials for Membrane Capacitive Deionization," *ACS ES&T Water,* 2020.

[24] J. W. Blair and G. W. Murphy, "Electrochemical demineralization of water with porous electrodes of large surface area," ACS Publications, 1960.

[25] W. Tang, J. Liang, D. He, J. Gong, L. Tang, Z. Liu, D. Wang, and G. Zeng, "Various cell architectures of capacitive deionization: Recent advances and future trends," *Water Res.,* 2018.

[26] E. N. Guyes, A. Simanovski, and M. E. Suss, "Several orders of magnitude increase in the hydraulic permeability of flow-through capacitive deionization electrodes via laser perforations," *RSC advances,* vol. 7, no. 34, pp. 21308-21313, 2017.

[27] X. Gao, A. Omosebi, J. Landon, and K. Liu, "Surface charge enhanced carbon electrodes for stable and efficient capacitive deionization using inverted adsorption–desorption behavior," *Energy & Environmental Science,* vol. 8, no. 3, pp. 897-909, 2015.

[28] X. Gao, A. Omosebi, J. Landon, and K. Liu, "Enhanced salt removal in an inverted capacitive deionization cell using amine modified microporous carbon cathodes," *Environmental science & technology,* vol. 49, no. 18, pp. 10920-10926, 2015.

[29] P. A. Fritz, R. Boom, and K. Schroen, "Polyelectrolyte-activated carbon composite electrodes for inverted membrane capacitive deionization (iMCDI)," *Separation and Purification Technology,* vol. 220, pp. 145-151, 2019.

[30] P. A. Fritz, F. Zisopoulos, S. Verheggen, K. Schroën, and R. Boom, "Exergy analysis of membrane capacitive deionization (MCDI)," *Desalination,* vol. 444, pp. 162-168, 2018.

[31] A. Rommerskirchen, Y. Gendel, and M. Wessling, "Single module flow-electrode capacitive deionization for continuous water desalination," *Electrochemistry Communications,* vol. 60, pp. 34-37, 2015.

[32] S.-i. Jeon, H.-r. Park, J.-g. Yeo, S. Yang, C. H. Cho, M. H. Han, and D. K. Kim, "Desalination via a new membrane capacitive deionization process utilizing flow-electrodes," *Energy & Environmental Science,* vol. 6, no. 5, pp. 1471-1475, 2013.

[33] S. Yang, J. Choi, J.-g. Yeo, S.-i. Jeon, H.-r. Park, and D. K. Kim, "Flow-electrode capacitive deionization using an aqueous electrolyte with a high salt concentration," *Environmental science & technology,* vol. 50, no. 11, pp. 5892-5899, 2016.

[34] J. Ma, C. He, D. He, C. Zhang, and T. D. Waite, "Analysis of capacitive and electrodialytic contributions to water desalination by flow-electrode CDI," *Water Res.,* vol. 144, pp. 296-303, 2018.

[35] P. Liang, X. Sun, Y. Bian, H. Zhang, X. Yang, Y. Jiang, P. Liu, and X. Huang, "Optimized desalination performance of high voltage flow-electrode capacitive deionization by adding carbon black in flow-electrode," *Desalination,* vol. 420, pp. 63-69, 2017.

[36] K. Fang, H. Gong, W. He, F. Peng, C. He, and K. Wang, "Recovering ammonia from municipal wastewater by flow-electrode capacitive deionization," *Chemical Engineering Journal,* vol. 348, pp. 301-309, 2018.

[37] Y. Cho, C.-Y. Yoo, S. W. Lee, H. Yoon, K. S. Lee, S. Yang, and D. K. Kim, "Flow-electrode capacitive deionization with highly enhanced salt removal performance utilizing high-aspect ratio functionalized carbon nanotubes," *Water Res.,* vol. 151, pp. 252-259, 2019.

[38] K. Tang, S. Yiacoumi, Y. Li, and C. Tsouris, "Enhanced Water Desalination by Increasing the Electroconductivity of Carbon Powders for High-Performance Flow-Electrode Capacitive Deionization," *ACS Sustainable Chemistry & Engineering,* vol. 7, no. 1, pp. 1085-1094, 2018.

[39] S. Yang, H.-r. Park, J. Yoo, H. Kim, J. Choi, M. H. Han, and D. K. Kim, "Plate-shaped graphite for improved performance of flow-electrode capacitive deionization," *Journal of The Electrochemical Society,* vol. 164, no. 13, pp. E480-E488, 2017.

[40] A. Rommerskirchen, B. Ohs, K. A. Hepp, R. Femmer, and M. Wessling, "Modeling continuous flow-electrode capacitive deionization processes with ion-exchange membranes," *Journal of membrane science,* vol. 546, pp. 188-196, 2018.

[41] M. Li and H. G. Park, "Pseudocapacitive coating for effective capacitive deionization," *ACS applied materials & interfaces,* vol. 10, no. 3, pp. 2442-2450, 2018.

[42] K. Singh, S. Porada, H. De Gier, P. Biesheuvel, and L. De Smet, "Timeline on the application of intercalation materials in Capacitive Deionization," *Desalination,* vol. 455, pp. 115-134, 2019.

[43] E. R. Reale, A. Shrivastava, and K. C. Smith, "Effect of conductive additives on the transport properties of porous flow-through electrodes with insulative particles and their optimization for Faradaic deionization," *Water research,* vol. 165, p. 114995, 2019.

[44] Y.-H. Tu, C.-F. Liu, J.-A. Wang, and C.-C. Hu, "Construction of an inverted-capacitive deionization system utilizing pseudocapacitive materials," *Electrochemistry Communications,* p. 106486, 2019.

[45] J.-H. Choi, "Comparison of constant voltage (CV) and constant current (CC) operation in the membrane capacitive deionisation process," *Desalination and Water Treatment,* vol. 56, no. 4, pp. 921-928, 2015.

[46] J. Kang, T. Kim, K. Jo, and J. Yoon, "Comparison of salt adsorption capacity and energy consumption between constant current and constant voltage operation in capacitive deionization," *Desalination,* vol. 352, pp. 52-57, 2014.

[47] Y. Qu, P. G. Campbell, L. Gu, J. M. Knipe, E. Dzenitis, J. G. Santiago, and M. Stadermann, "Energy consumption analysis of constant voltage and constant current operations in capacitive deionization," *Desalination,* vol. 400, pp. 18-24, 2016.

[48] M. W. Saleem, Y. Jande, M. Asif, and W.-S. Kim, "Hybrid CV-CC operation of capacitive deionization in comparison with constant current and constant voltage," *Separation Science and Technology,* vol. 51, no. 6, pp. 1063-1069, 2016.

[49] S. Honarparvar, X. Zhang, T. Chen, C. Na, and D. Reible, "Modeling technologies for desalination of brackish waterΓÇËtoward a sustainable water supply," *Current Opinion in Chemical Engineering,* vol. 26, pp. 104-111, 2019.

[50] C. Bales, P. Kovalsky, J. Fletcher, and T. D. Waite, "Low cost desalination of brackish groundwaters by Capacitive Deionization (CDI)–Implications for irrigated agriculture," *Desalination,* vol. 453, pp. 37-53, 2019.

[51] J.-H. Lee and J.-H. Choi, "The production of ultrapure water by membrane capacitive deionization (MCDI) technology," *Journal of membrane science,* vol. 409, pp. 251-256, 2012.

[52] J. Choi, P. Dorji, H. K. Shon, and S. Hong, "Applications of capacitive deionization: Desalination, softening, selective removal, and energy efficiency," *Desalination,* vol. 449, pp. 118-130, 2019.

[53] A. Kalfa, B. Shapira, A. Shopin, I. Cohen, E. Avraham, and D. Aurbach, "Capacitive Deionization for Wastewater Treatment: Opportunities and Challenges," *Chemosphere,* p. 125003, 2019.

[54] P. Dorji, D. I. Kim, S. Hong, S. Phuntsho, and H. K. Shon, "Pilot-scale membrane capacitive deionisation for effective bromide removal and high water recovery in seawater desalination," *Desalination,* vol. 479, p. 114309, 2020.

[55] J. Choi, Y. Oh, S. Chae, and S. Hong, "Membrane capacitive deionization-reverse electrodialysis hybrid system for improving energy efficiency of reverse osmosis seawater desalination," *Desalination,* vol. 462, pp. 19-28, 2019.

[56] Z.-H. Huang, Z. Yang, F. Kang, and M. Inagaki, "Carbon electrodes for capacitive deionization," *Journal of Materials Chemistry A,* vol. 5, no. 2, pp. 470-496, 2017.

[57] R. Zhao, P. Biesheuvel, H. Miedema, H. Bruning, and A. Van der Wal, "Charge efficiency: a functional tool to probe the double-layer structure inside of porous electrodes and application in the modeling of capacitive deionization," *The Journal of Physical Chemistry Letters,* vol. 1, no. 1, pp. 205-210, 2009.

[58] J. Ma, L. Wang, F. Yu, and X. Dai, "Mesoporous amorphous FePO4 nanosphere@ Graphene as a faradic electrode in capacitive deionization for high-capacity and fast removal of NaCl from water," *Chemical Engineering Journal,* vol. 370, pp. 938-943, 2019.

[59] X. Liu, H. Liu, M. Mi, W. Kong, Y. Ge, and J. Hu, "Nitrogen-doped hierarchical porous carbon aerogel for high-performance capacitive deionization," *Separation and Purification Technology,* vol. 224, pp. 44-50, 2019.

[60] C. Lin, J. A. Ritter, and B. N. Popov, "Correlation of Double‐Layer Capacitance with the Pore Structure of Sol‐Gel Derived Carbon Xerogels," *Journal of the Electrochemical Society,* vol. 146, no. 10, pp. 3639-3643, 1999.

[61] K. Laxman, D. Kimoto, A. Sahakyan, and J. Dutta, "Nanoparticulate Dielectric Overlayer for Enhanced Electric Fields in a Capacitive Deionization Device," *ACS applied materials & interfaces,* vol. 10, no. 6, pp. 5941-5948, 2018.

[62] W. Zhang, M. Mossad, and L. Zou, "A study of the long-term operation of capacitive deionisation in inland brackish water desalination," *Desalination,* vol. 320, pp. 80-85, 2013.

[63] M. Mossad and L. Zou, "Study of fouling and scaling in capacitive deionisation by using dissolved organic and inorganic salts," *Journal of hazardous materials,* vol. 244, pp. 387-393, 2013.

[64] Z. Wang, Y. Wang, D. Ma, S. Xu, and J. Wang, "Investigations on the fouling characteristics of ion-doped polypyrrole/carbon nanotube composite electrodes in capacitive deionization by using half cycle running mode," *Separation and Purification Technology,* vol. 192, pp. 15-20, 2018.

[65] A. Hassanvand, G. Chen, P. Webley, and S. Kentish, "An investigation of the impact of fouling agents in capacitive and membrane capacitive deionisation," *Desalination,* vol. 457, pp. 96-102, 2019.

[66] X. Liu, J. F. Whitacre, and M. S. Mauter, "Mechanisms of humic acid fouling on capacitive and insertion electrodes for electrochemical desalination," *Environmental science & technology,* vol. 52, no. 21, pp. 12633-12641, 2018.

[67] W. Zhang and B. Jia, "Toward anti-fouling capacitive deionization by using visible-light reduced TiO 2/graphene nanocomposites," *MRS Communications,* vol. 5, no. 4, pp. 613-617, 2015.

[68] P. Zhang, P. A. Fritz, K. Schro ├½n, H. Duan, R. M. Boom, and M. B. Chan-Park, "Zwitterionic Polymer Modified Porous Carbon for High-Performance and Antifouling Capacitive Desalination," *ACS applied materials & interfaces,* vol. 10, no. 39, pp. 33564-33573, 2018.

[69] S. Liang, M. Li, J. Cao, K. Zuo, Y. Bian, K. Xiao, and X. Huang, "Integrated ultrafiltrationΓÇôcapacitive-deionization (UCDI) for enhanced antifouling performance and synchronous removal of organic matter and salts," *Separation and Purification Technology,* 2019.

[70] L. Chen, C. Wang, S. Liu, Q. Hu, L. Zhu, and C. Cao, "Investigation of the long-term desalination performance of membrane capacitive deionization at the presence of organic foulants," *Chemosphere,* vol. 193, pp. 989-997, 2018.

[71] C. Wang, L. Chen, and L. Zhu, "Effect of combined fouling on desalination performance of membrane capacitive deionization (MCDI) during long-term operation," *Journal of Dispersion Science and Technology,* pp. 1-10, 2019.

[72] S. Mikhaylin and L. Bazinet, "Fouling on ion-exchange membranes: Classification, characterization and strategies of prevention and control," *Advances in colloid and interface science,* vol. 229, pp. 34-56, 2016.

[73] L. Wang and S. Lin, "Membrane capacitive deionization with constant current vs constant voltage charging: which is better?," *Environmental science & technology,* vol. 52, no. 7, pp. 4051-4060, 2018.

[74] T. Kim, J. Dykstra, S. Porada, A. Van Der Wal, J. Yoon, and P. Biesheuvel, "Enhanced charge efficiency and reduced energy use in capacitive deionization by increasing the discharge voltage," *Journal of colloid and interface science,* vol. 446, pp. 317-326, 2015.

[75] Y. Zhao, Y. Wang, R. Wang, Y. Wu, S. Xu, and J. Wang, "Performance comparison and energy consumption analysis of capacitive deionization and membrane capacitive deionization processes," *Desalination,* vol. 324, pp. 127-133, 2013.

[76] R. Zhao, P. Biesheuvel, and A. Van der Wal, "Energy consumption and constant current operation in membrane capacitive deionization," *Energy & Environmental Science,* vol. 5, no. 11, pp. 9520-9527, 2012.

[77] A. Hemmatifar, J. W. Palko, M. Stadermann, and J. G. Santiago, "Energy breakdown in capacitive deionization," *Water Res.,* vol. 104, pp. 303-311, 2016.

[78] A. Hemmatifar, "Energy Consumption and Salt Adsorption in Capacitive Deionization," Stanford University, 2018.

[79] O. Sufiani, J. Elisadiki, R. L. Machunda, and Y. A. Jande, "Modification strategies to enhance electrosorption performance of activated carbon electrodes for capacitive deionization applications," *Journal of Electroanalytical Chemistry,* p. 113328, 2019.

[80] Y. Cheng, Z. Hao, C. Hao, Y. Deng, X. Li, K. Li, and Y. Zhao, "A review of modification of carbon electrode material in capacitive deionization," *RSC Advances,* vol. 9, no. 42, pp. 24401-24419, 2019.

[81] Y. M. Volfkovich, A. Y. Rychagov, A. Mikhalin, M. Kardash, N. Kononenko, D. Ainetdinov, S. Shkirskaya, and V. Sosenkin, "Capacitive deionization of water using mosaic membrane," *Desalination,* vol. 426, pp. 1-10, 2018.

[82] Y. Bian, X. Yang, P. Liang, Y. Jiang, C. Zhang, and X. Huang, "Enhanced desalination performance of membrane capacitive deionization cells by

packing the flow chamber with granular activated carbon," *Water Res.,* vol. 85, pp. 371-376, 2015.

[83] P. Liang, L. Yuan, X. Yang, S. Zhou, and X. Huang, "Coupling ion-exchangers with inexpensive activated carbon fiber electrodes to enhance the performance of capacitive deionization cells for domestic wastewater desalination," *Water Res.,* vol. 47, no. 7, pp. 2523-2530, 2013.

[84] S. K. Patel, M. Qin, W. S. Walker, and M. Elimelech, "Energy Efficiency of Electro-Driven Brackish Water Desalination: Electrodialysis Significantly Outperforms Membrane Capacitive Deionization," *Environmental Science & Technology,* 2020.

[85] M. Qin, A. Deshmukh, R. Epsztein, S. K. Patel, O. M. Owoseni, W. S. Walker, and M. Elimelech, "Comparison of energy consumption in desalination by capacitive deionization and reverse osmosis," *Desalination,* vol. 455, pp. 100-114, 2019.

[86] M. Qin, A. Deshmukh, R. Epsztein, S. K. Patel, O. M. Owoseni, W. S. Walker, and M. Elimelech, "Response to comments on" comparison of energy consumption in desalination by capacitive deionization and reverse osmosis"," *Desalination,* vol. 462, pp. 48-55, 2019.

[87] S. Porada, L. Zhang, and J. Dykstra, "Energy consumption in membrane capacitive deionization and comparison with reverse osmosis," *Desalination,* vol. 488, p. 114383, 2020.

[88] L. Wang, J. Dykstra, and S. Lin, "Energy efficiency of capacitive deionization," *Environmental science & technology,* vol. 53, no. 7, pp. 3366-3378, 2019.

[89] C. Zhang, L. Wu, J. Ma, A. N. Pham, M. Wang, and T. D. Waite, "Integrated flow-electrode capacitive deionization and microfiltration system for continuous and energy-efficient brackish water desalination," *Environmental science & technology,* vol. 53, no. 22, pp. 13364-13373, 2019.

[90] A. M. Pernía, M. J. Prieto, J. A. Martín-Ramos, P. J. Villegas, and F. J. Álvarez-González, "Energy Recovery in Capacitive Deionization Technology," *Desalination and Water Treatment,* p. 37, 2018.

[91] Y. Jande and W.-S. Kim, "Integrating reverse electrodialysis with constant current operating capacitive deionization," *Journal of environmental management,* vol. 146, pp. 463-469, 2014.

[92] Y. A. C. Jande and W.-S. Kim, "Simultaneous production of freshwater and energy from saline water using hybrid capacitive deionization-reverse electrodialysis," *Int. J. Res. Chem. Metall. Civ. Eng.,* vol. 1, pp. 35-39, 2014.

[93] M. W. Saleem, Y. Jande, and W.-S. Kim, "Performance optimization of integrated electrochemical capacitive deionization and reverse electrodialysis model through a series pass desorption process," *Journal of Electroanalytical Chemistry,* vol. 795, pp. 41-50, 2017.

[94] M. W. Saleem, B.-G. Im, and W.-S. Kim, "Electrochemical CDI integration with PRO process for water desalination and energy production: Concept, simulation, and performance evaluation," *Journal of Electroanalytical Chemistry,* vol. 822, pp. 134-143, 2018.

[95] P. Długołęcki and A. van der Wal, "Energy recovery in membrane capacitive deionization," *Environmental science & technology,* vol. 47, no. 9, pp. 4904-4910, 2013.

[96] L. Chen, X. Yin, L. Zhu, and Y. Qiu, "Energy recovery and electrode regeneration under different charge/discharge conditions in membrane capacitive deionization," *Desalination,* vol. 439, pp. 93-101, 2018.

[97] J. Kang, T. Kim, H. Shin, J. Lee, J.-I. Ha, and J. Yoon, "Direct energy recovery system for membrane capacitive deionization," *Desalination,* vol. 398, pp. 144-150, 2016.

[98] Y.-W. Chen, J.-F. Chen, C.-H. Lin, and C.-H. Hou, "Integrating a supercapacitor with capacitive deionization for direct energy recovery from the desalination of brackish water," *Applied Energy,* vol. 252, p. 113417, 2019.

[99] C. Tan, C. He, J. Fletcher, and T. D. Waite, "Energy recovery in pilot scale membrane CDI treatment of brackish waters," *Water Res.,* p. 115146, 2019.

[100] J. Dykstra, S. Porada, A. Van Der Wal, and P. Biesheuvel, "Energy consumption in capacitive deionization–Constant current versus constant voltage operation," *Water research,* vol. 143, pp. 367-375, 2018.

[101] A. Rommerskirchen, C. J. Linnartz, D. Müller, L. K. Willenberg, and M. Wessling, "Energy Recovery and Process Design in Continuous Flow–Electrode Capacitive Deionization Processes," *ACS Sustainable Chemistry & Engineering,* vol. 6, no. 10, pp. 13007-13015, 2018.

[102] J. Ma, P. Liang, X. Sun, H. Zhang, Y. Bian, F. Yang, J. Bai, Q. Gong, and X. Huang, "Energy recovery from the flow-electrode capacitive deionization," *Journal of Power Sources,* vol. 421, pp. 50-55, 2019.

[103] H. Lim, Y. Ha, H. B. Jung, P. S. Jo, H. Yoon, D. Quyen, N. Cho, C.-Y. Yoo, and Y. Cho, "Energy Storage and Generation through Desalination Using Flow-Electrodes Capacitive Deionization," *Journal of Industrial and Engineering Chemistry,* 2019.

[104] X. Liu, S. Shanbhag, T. V. Bartholomew, J. F. Whitacre, and M. S. Mauter, "Cost Comparison of Capacitive Deionization and Reverse Osmosis for Brackish Water Desalination," *ACS ES&T Engineering,* 2020.

[105] S. Hand, J. S. Guest, and R. D. Cusick, "Technoeconomic analysis of brackish water capacitive deionization: navigating tradeoffs between performance, lifetime, and material costs," *Environmental Science & Technology,* vol. 53, no. 22, pp. 13353-13363, 2019.

[106] H. Strathmann, A. Grabowski, and G. Eigenberger, "Ion-exchange membranes in the chemical process industry," *Industrial & Engineering Chemistry Research,* vol. 52, no. 31, pp. 10364-10379, 2013.

[107] S.-Y. Pan, A. Z. Haddad, A. Kumar, and S.-W. Wang, "Brackish water desalination using reverse osmosis and capacitive deionization at the water-energy nexus," *Water Research,* p. 116064, 2020.

[108] X. Liu, S. Shanbhag, S. Natesakhawat, J. F. Whitacre, and M. S. Mauter, "Performance Loss of Activated Carbon Electrodes in Capacitive Deionization: Mechanisms and Material Property Predictors," *Environmental Science & Technology,* 2020.

[109] M. Metzger, M. M. Besli, S. Kuppan, S. Hellstrom, S. Kim, E. Sebti, C. V. Subban, and J. Christensen, "Techno-economic analysis of capacitive and intercalative water deionization," *Energy & Environmental Science,* 2020.

[110] H. Helmholtz, "Uber einige Gesetze der Vertheilung elektrischer Strome in korperlichen Leitem, mit Anwendung auf die thierisch-elektrischen Versuche," *Ann. Phys. Chem,* vol. 89, p. 21, 1853.

[111] O. Stern, "Zur theorie der elektrolytischen doppelschicht," *Zeitschrift für Elektrochemie und angewandte physikalische Chemie,* vol. 30, no. 21‐22, pp. 508-516, 1924.

[112] J. S. Newman and C. W. Tobias, "Theoretical analysis of current distribution in porous electrodes," *Journal of The Electrochemical Society,* vol. 109, no. 12, p. 1183, 1962.

[113] A. Johnson and J. Newman, "Desalting by means of porous carbon electrodes," *Journal of the Electrochemical Society,* vol. 118, no. 3, pp. 510-517, 1971.

[114] J. Newman and W. Tiedemann, "Porous‐electrode theory with battery applications," *AIChE Journal,* vol. 21, no. 1, pp. 25-41, 1975.

[115] R. A. Rica, R. Ziano, D. Salerno, F. Mantegazza, M. Z. Bazant, and D. Brogioli, "Electro-diffusion of ions in porous electrodes for capacitive extraction of renewable energy from salinity differences," *Electrochimica Acta,* vol. 92, pp. 304-314, 2013.

[116] R. l. A. Rica, D. Brogioli, R. Ziano, D. Salerno, and F. Mantegazza, "Ions transport and adsorption mechanisms in porous electrodes during capacitive-mixing double layer expansion (CDLE)," *The Journal of Physical Chemistry C,* vol. 116, no. 32, pp. 16934-16938, 2012.

CHAPTER 2

MODELING CAPACITIVE DEIONIZATION, A REVIEW

2.1. Abstract

Capacitive deionization (CDI) is an easy to assemble and energy efficient desalination technique for treating a small quantity of low-salinity brackish water. Modeling ion transport and adsorption dynamics in CDI contributes to the optimization of cell design and operation, energy consumption and energy efficiency investigation and techno-economic analyses. The four types of CDI models were identified and compared with respect to their ability to capture electrosorption mechanisms and Faradaic reactions, computational complexity and scope of application. Overall, modified Donnan theory based CDI models were identified as the most mature and can be applied to a wide range of applications. Equivalent circuit models could serve as alternatives for estimating energy behaviors of CDI in single salt solution. Dynamic Langmuir models should be modified to describe Faradaic reactions. CDI simulation needs and potential future directions were identified.

[1] This chapter is based on a manuscript under preparation as: Zhang, X, Reible, D. Modeling capacitive deionization, a review, 2021.

2.2. Graphical abstract

CDI models	Electrosorption mechanisms	Faradaic reactions	Calculation simplicity	Application scope
Modified Donnan based CDI models	★★★	★★½	★½☆	★★★
Isotherm and kinetic models	★☆☆	☆☆☆	★★★	★☆☆
Dynamic Langmuir models	★★☆	☆☆☆	★★☆	★½☆
Equivalent circuit models	★★☆	★★☆	★★½	★★☆

2.3. Introduction

Capacitive deionization (CDI) was first proposed in 1960s [1], and has regained academic interest in the past two decades due to the easy assembling and relatively low energy consumption for desalinating low salinity brackish waters and near-fresh waters [2]. Conventional CDI is assembled by inserting a spacer between a pair of porous electrodes. A porous spacer is commonly used in CDI to prevent short-circuiting, enhance ion mixing and eliminate concentration polarization [3]. A current collector is attached onto the electrode to convey current from the external power supply. The charging modes of CDI includes constant current (CC) and constant voltage (CV). Ions are driven by the electric force toward the oppositely charged electrode and are adsorbed in the electric double layer (EDL) forming close to the electrode surface during desalination, and are repelled back to the channel during regeneration by either short-circuiting or reverse charging the electrodes. A number of alternative architectures of CDI have been developed to enhance adsorption capacity, improve desalination performance and expand application scopes. Tang et al. [4] reviewed the recent developments of materials, cell assembly, operating modes, and specific applications of the CDI variants including membrane CDI (MCDI), flow-through CDI, inverted CDI (I-CDI), flow-electrode CDI (FCDI) and intercalation electrodes aided CDI.

CDI can be operated in a closed system termed batch mode by desalinating a volume of brackish water until electrode saturation is achieved, or can be operated in an open system as single-pass mode by continuously pumping untreated water through the channel in alternating desalination and regeneration steps. In single-pass mode, partially

recycling the brine can improve water recovery [5]. Salamat and Hidrovo [6] conducted a hybrid-cycle operation by recycling the permeate stream during desalination to enhance salt removal efficiency, and recycling the brine stream during regeneration to enhance water recovery. Novel flow modes such as pulse flow [7] and sinusoidal flow [8] have also been employed to enhance the operation efficiency.

The ion adsorption capacity of CDI is related to the electrode material, electrode pore geometry, effective surface area of porous electrode, feed water composition and salinity, and applied voltage or current during both desalination and regeneration [2]. The most effective pore size distribution is still under debate. Salt adsorption capacity was observed to be positively related to the pore volumes with mean pore sizes smaller than 1 nm, especially in microporous electrode [9, 10]. However, Hou et al. [11] revealed a considerable loss of capacitance in micropores. Yang et al. [12] proposed a cut-off pore width of 0.6 nm at an applied voltage of 1.2V and feed water salinity of 100 ppm, below which no effective adsorption was observed. This cut-off pore width was expected to decrease with increasing salinity and applied voltage [12].

Capacitance increases with increasing ionic and electronic charge density of micropores due to the reduced Stern layer thickness from the stronger electrostatic compression [13]. Relatively high applied voltage and temperature facilitate the distortion of ion hydration shell, enhancing the accessibility of the pores with similar size as hydrated ions, and thus improve the capacitance [14]. Jiménez et al. [15] predicted a maximum capacitance at a specific applied voltage by incorporating ion exclusion effects in the simulation. Sub-nanometer pores were revealed to possess a relatively high capacitance

[14]. Capacitance in FCDI increases with increasing flow-electrode content due to the enhanced collision possibility [16].

Charge efficiency is defined by the ratio of the adsorbed ions over the transferred charges at equilibrium [17]. A charged electrode surface attracts counter-ions and repels co-ions. If the applied voltage is below thermal voltage, counter-ion attraction and co-ion repulsion balance each other, resulting in zero adsorption [2]. Due to co-ion repulsion and current leakage from Faradaic reactions, the charge efficiency is always less than 1. Shang et al. [7] revealed that salt retention in the cell during desalination further reduced charge efficiency. However, by assembling ion-exchange membrane (IEM) in front of the electrode, co-ion repulsion and Faradaic reactions can be reduced, improving charge efficiency [2]. Differential charge efficiency [18] and chemical charge efficiency [19] have been proposed to explore the ratio of salt flux over charge flux and the ratio of adsorbed salt over chemical charges on uncharged electrode surface, respectively.

Modeling ion transport and adsorption behavior in CDI can aid in understanding the electrosorption mechanisms and can be used to optimize cell design and operating conditions. Liu et al. [20] categorized CDI simulation efforts into three scales, namely, atom-scale, electrode-scale, and plant-scale. Atom-scale models are mainly based on molecular dynamics simulation and density functional theory, incorporating the interactions among ions, electrons and solvents. These atom-scale models are instructive for synthesis and selection of electrode material for CDI. Electrode-scale models depict the macroscopic transport and adsorption of ions and account for the main

part of CDI models. Plant-scale models include parametric models which either ignore simulating CDI process [21], or simulate CDI units as capacitors with simple equations [22, 23], for the purpose of conducting techno-economic analyses of full size CDI modules.

This review focuses on electrode-scale models aiming at 1) Introducing EDL theory and proposing a comprehensive CDI model, which incorporates macroscopic transport equations coupled with modified Donnan (mD) theory to simulate ion transport and adsorption dynamics in CDI; 2) Describing the development of the key equations of other models that have been applied to simulating CDI process including isotherm and kinetics models, DL models, and equivalent circuit models; 3) Comparing the four types of CDI models and their ability to simulate electrosorption mechanisms and Faradaic reactions, their computational complexity and the range of their applications.

2.4. EDL based models

2.4.1 EDL theory

Adsorption process in capacitive electrodes is associated with the development of the EDL. EDL theory is based on a local equilibrium between micropores and the adjacent macropores. This local equilibrium holds since ion transport dynamics in EDL are commonly not rate-limiting considering the scale of the EDL is nanometers compared to the micron scale CDI thickness [24]. The first proposed EDL model was the Helmholtz model, which assumes that ions linearly condense onto the pore wall [25]. However, the Helmholtz model does not consider the finite size of hydrated ions which

limits their proximity to the pore wall. Stern [26] assumed an ion-free layer between pore surface and solution to account for ion hydrated radius to form Gouy-Chapman-Stern (GCS) theory. In GSC theory, the ion distribution in the diffuse layer follows Boltzmann equation. GCS theory is valid for planar electrodes and macroporous electrodes with pore sizes much larger than Debye length [2] to avoid EDL overlapping, but is less accurate for microporous electrodes with pore sizes similar or smaller than Debye length, where EDL overlapping is inevitable.

Classical Donnan theory was proposed assuming no concentration or potential gradient inside the narrow pores where EDL overlapped, and considering a step change of potential termed Donnan potential at the pore opening [27]. Donnan theory is derived from a local electrochemical potential equilibrium for the same ions. Subsequently, modified Donnan (mD) theory was proposed by adding Stern layer and a chemical potential term for non-electrostatic attraction of the pore wall toward the approaching ions [28]. This mD theory and its extensions have been widely used for simulating ion adsorption behaviors in CDI considering the porous electrodes are mainly composed of micropores with overlapped EDL.

A series of advanced models including modified Poisson-Boltzman (PB) equations [29, 30] or modified Poisson-Nernst-Planck (PNP) equations have been proposed for simulating EDL development under relatively high concentration and applied voltage where non-ideality becomes significant [31-33]. These modified equations can be simplified to be incorporated into mD theory to capture the non-ideality of the solution and improve the simulation accuracy.

2.4.2 Mathematical development of mD theory based process models

Macroscopic porous electrode (MPE) theory separates the void space in an electrode into macropores, which serves as transport path, and micropores, which serve as the adsorption site [34-36]. MPE theory avoids dealing with the complex morphology of electrode material and employs volume-averaged parameters that can be easily obtained, such as porosity and volume-average resistivity. Macroscopic transport equations have been used for simulating transport in porous media and are applicable for describing ion transport in porous electrode, spacer-filled channel and IEM (if applied). A comprehensive CDI process model incorporating the published extensions of mD theory based CDI models is proposed in the following sections.

2.4.2.1 Ion transport and adsorption in electrode

Ion transport in an electrode is commonly described by mass balance equation coupling an extended Nernst-Planck (NP) flux, with ion adsorption rate inserted as a sink term. Ion adsorption in electrode is simulated by mD theory and its extensions. A porous electrode is usually assumed to only contain macropores and micropores. However, Kim et al. [37] and Dykstra et al. [38] incorporated mesopores into the electrode as well and assumed mesopores to be electroneutral with the same concentration as the adjacent macropores but did not serve as ion transport path. Part of the feed water was assumed to flow through the electrodes in some studies [28, 39]. However, considering the low permeability from the relatively small pore size of most electrodes compared to spacer-filled channel, flow resistance in the electrode is much higher than that of the channel,

making water flowing through the electrode negligible except for flow-through CDI [10].

A comprehensive macroscopic ion transport and adsorption equation for porous electrode is given by:

$$\varepsilon_{ma}\frac{\partial c_{ma,i}}{\partial t}+\varepsilon_{me}\frac{\partial c_{ma,i}}{\partial t}+\varepsilon_{mi}\frac{\partial c_{mi,i}}{\partial t}=\nabla\cdot\left(D_{ma,i}\nabla c_{ma,i}+\frac{z_i D_{ma,i}F c_{ma,i}}{RT}\nabla\varphi_{ma}-U_{ma}c_{ma,i}\right)\pm r_{F,i} \quad (2.1)$$

where ε_{ma}, ε_{me}, ε_{mi}, are the void fractions of macropores, mesopores and micropores, respectively, $c_{ma,i}$ and $c_{mi,i}$ are the concentrations of ion species i in macropores and micropores, respectively, t is the operating time, z_i is the ion valence of ion species i, F is Faraday's constant (96485 C/mol), R is universal gas constant (8.314 J/mol/K), T is ambient temperature, φ_{ma} is the electrolyte potential in macropores, U_{ma} is the Darcy velocity in macropores if water flowing through the electrode is considered, $r_{F,i}$ is the Faradaic reaction rate of ion species i assuming one-electron transfer per reaction, minus sign is for i to be oxidant while plus sign is for i to be reductant, and $D_{ma,i}$ is the effective diffusion coefficient of ion species i in macropores corrected for tortuosity by Bruggeman relation [40]:

$$D_{ma,i}=D_i^0(\varepsilon_{ma}/{\varepsilon_{ma}}^{-1/2}) \quad (2.2)$$

where D_i^0 is the diffusion coefficient of ionic species i in solution.

Electroneutrality holds in macropores:

$$\sum_i z_i c_{ma,i} = 0 \tag{2.3}$$

A comprehensive mD theory incorporating the published extensions is given by:

$$c_{mi,i} = c_{ma,i} exp(-\frac{z_i F \Delta\varphi_d}{RT} + \mu_{att} - \Delta\mu_i^{ex}) \tag{2.4}$$

$$\Delta\mu_i^{ex} = \mu_{mi,i}^{ex} - \mu_{ma,i}^{ex} \tag{2.5}$$

where $\Delta\varphi_d$ is the Donnan potential, μ_{att} is the dimensionless non-electrostatic attraction term, and $\Delta\mu_i^{ex}$ is the dimensionless excess chemical potential difference between micropores, $\mu_{mi,i}^{ex}$, and the adjacent macropores, $\mu_{ma,i}^{ex}$, accounting for ion exclusion effects. Among the expressions of this excess chemical potential, Carnahan–Starling (CS) expression provides sufficient accuracy for single salt solutions, while Boublik–Mansoori–Carnahan–Starling–Leland (BMCSL) expression better suits ion mixtures with unequal sizes [41]. BMCSL expression has been employed to evaluate the effects of hydrated ion sizes on ion selectivity in multicomponent system CDI [42, 43].

Most studies set μ_{att} to a constant value, which is fitted from experimental observations. The μ_{att} can be omitted if non-electrostatic adsorption is negligible. Biesheuvel et al. [44] proposed an improved mD (i-mD) theory to incorporate the image forces in micropores by correlating μ_{att} with micropore concentrations:

$$\mu_{att} = \frac{E}{c_{ion,mi}} \tag{2.6}$$

$$c_{ion,mi} = \sum_i c_{mi,i} \tag{2.7}$$

where E is the scaled attractive Coulomb energy [44], and $c_{ion,mi}$ is the total concentration of cations and anions in micropores.

In CDI with functionalized electrodes, chemical charges are attached onto electrode surface to either enhance adsorption capacity, or form I-CDI. Hence, μ_{att} can be dropped by adding a chemical charge density term in the charge balance equation of micropores to simulate the interactions between the fixed charges and the ions [45]:

$$\sigma_{elec} \pm \sigma_F + \sigma_{chem} + \sigma_{mi} = 0 \tag{2.8}$$

$$\sigma_{mi} = \sum_i z_i c_{mi,i} \tag{2.9}$$

where σ_{elec} is the electronic charge density on electrode matrix, σ_{chem} is the chemical charge density on electrode surface, σ_{mi} is the ion charge density in micropores, and σ_F is the transferred electron charge density during Faradaic reactions in micropores with positive sign for anode and negative sign for cathode. These parameters are scaled as micropore volume-averaged concentration terms.

Carboxylic and phenolic functional groups with negative charges are introduced to electrode surface via thermal and chemical activation during electrode synthesis. In addition, the adsorption of protons into the carbon basal planes may introduce positive surface charges. Biesheuvel [46] proposed an amphoteric Donnan model by dividing electrode into two regions including an acidic region containing negative chemical charges, and a basic region containing positive charges. The charge balance of micropores should be calculated separately in acidic and basic regions. The total electronic charge density of micropores in each electrode is given by:

$$\sigma_{elec} = \sum_{j=A,B} \alpha_j \sigma_{elec,j} \tag{2.10}$$

where α_j is the volumetric fraction of acidic regions ($j=A$) and basic regions ($j=B$) in micropores.

The occurrence of Faradaic reactions under relatively high applied voltage and the rapid electromigration rate of protons can significantly change the pH values in solution [47]. By including the transport of proton and hydroxyl in simulation, the effects of pH changes can be simulated [48]. pH changes the chemical charge density due to the changing dissociation degree of the functional groups on electrode surface [19, 48]. Hemmatifar et al. [19] simulated the changes of chemical charge density by coupling mD theory with weak electrolyte acid-base equilibria theory. Chemical charge density is time-dependent and varies with the applied voltage if the surface functional groups are redox-active [49].

Faradaic reactions include irreversible redox active reactions such as carbon corrosion, oxygen reduction and water splitting, and reversible reactions occurring on intercalation electrodes, which can be employed to capture and release specific ions of interest. Adsorption capacity of intercalation electrode is much higher than capacitive electrodes. The adsorption mechanisms of intercalation electrodes can be simulated by Frumkin isotherm and its extensions [50-52]. Irreversible Faradaic reactions become dominant under relatively high applied voltage. Detailed reaction formulas, mechanisms and methods to inhibit irreversible Faradaic reactions have been comprehensively reviewed by Zhang et al. [53].

Generalized Frumkin-Butler-Volmer (gFBV) equation has been employed to simulate electron transfer rate of Faradaic reaction assuming one-electron transfer per reaction [47, 48, 54]:

$$r_F = k_R c_{mi,O} \exp\left(-\alpha_R \frac{F\Delta\varphi_{st}}{RT}\right) - k_O c_{mi,R} \exp\left(\alpha_O \frac{F\Delta\varphi_{st}}{RT}\right) \tag{2.11}$$

$$\frac{\partial \sigma_F}{\partial t} = r_F \tag{2.12}$$

where k_R and k_O are the rate constants of reduction reaction and the respective oxidization reaction, respectively, which depend on Faradaic reaction types, $c_{mi,O}$ and $c_{mi,R}$ are the concentrations of the respective oxidant and reductant of the same element in micropores, respectively, α_R and α_O are the transfer coefficients in reduction reaction and the respective oxidation reaction, respectively, which are both 0.5 for one-electron transfer redox reaction, and $\Delta\varphi_{st}$ is the Stern layer potential drop.

Under relatively high applied voltage or relatively low concentration, the slow electromigration rate of ions cannot balance the fast adsorption rate at the beginning of charging, leading to ion depletion in electrode macropores. The large concentration gradient from micropores to macropores contributes to the ion transport resistance from macropores into micropores and reduces the overall desalination rate. To account for this ion transport resistance, Salamat and Hidrovo [55] replaced the adsorption rate term with a modified Butler-Volmer expression assuming ion transfer to be analogical to electron transfer in redox reaction:

$$\varepsilon_{mi}\frac{\partial c_{mi,i}}{\partial t} = k[c_{ma,i}exp\left(\alpha_{ma-mi}\left(-\frac{z_i F\Delta\varphi_d}{RT}+\mu_{att}-\Delta\mu_i^{ex}\right)\right)-c_{mi,i}\exp((1-$$

$$\alpha_{ma-mi})\left(\frac{z_i F\Delta\varphi_d}{RT}-\mu_{att}+\Delta\mu_i^{ex}\right))] \quad (2.13)$$

where k is the transfer rate constant and $\alpha_{ma\text{-}mi}$ is the transfer coefficient between micropores and macropores.

Cell applied voltage, V_{cell}, is partially dropped on the external resistance:

$$V_{cell} = V_e + I_{ext}R_{ext} \quad (2.14)$$

where V_e is the remaining potential drop on the electrode pair and can be assumed to be evenly split on cathode ($-V_e/2$) and anode ($V_e/2$), R_{ext} is the external resistance mainly including wire resistance, current collector resistance and contact resistance at the interface of current collector and electrode [38], I_{ext} is the external current given by [56]:

$$I_{ext} = \iiint F\varepsilon_{mi}\frac{\partial\sigma_{mi}}{\partial t}dxdydz \quad (2.15)$$

where x, y, and z are the thickness, length and width directions, respectively. Ignoring electrode electronic resistance, the electric potential on the electrode is related to the electrolyte potential in electrode macropores by:

$$\pm\frac{V_e}{2} = \Delta\varphi_{st} + \Delta\varphi_d + \varphi_{ma} \quad (2.16)$$

where positive sign is for anode and negative sign is for cathode. Within each electrode, Stern layer potential drop is related to the electronic charge density of micropores by:

$$\Delta\varphi_{st} = \frac{F\sigma_{elec}}{C_{st}} \quad (2.17)$$

where C_{st} is the Stern layer capacitance. In the published CDI simulation efforts C_{st} is either considered to be constant for simplicity, or related to the ionic charge density in micropores via an empirical expression [9, 13]:

$$C_{st} = C_{st,0} + \alpha_{st}\sigma_{mi}^2 \tag{2.18}$$

where $C_{st,0}$ is the Stern layer capacitance without charging, and α_{st} is the correlation coefficient fitted from experimental observations.

For asymmetric cathode and anode, the electronic charge density of micropores in cathode and anode can be correlated by:

$$\varepsilon_{mi,c} d_c \sigma_{elec}|_c = \varepsilon_{mi,a} d_a \sigma_{elec}|_a \tag{2.19}$$

where subscript *c* and *a* represent cathode and anode, respectively, and *d* is the electrode thickness.

2.4.2.2 Ion transport in the channel

Ion transport in spacer-filled channel can be described by mass balance with extended NP flux including advection term:

$$\varepsilon_s \frac{\partial c_i}{\partial t} = \nabla \cdot [D_{disp} \nabla c_i + \frac{z_i D_i F c_i}{RT} \nabla \varphi - U c_i] \tag{2.20}$$

$$D_i = D_i^0 (\varepsilon_s / \varepsilon_s{}^{-1/3}) \tag{2.21}$$

where ε_s is the spacer's porosity, c_i is the concentration of species *i* in the channel, φ is the electrolyte potential in the channel, *U* is the Darcy velocity of the flowing solution, D_i is the effective diffusion coefficient of species *i* in the channel, which is corrected

tortuosity by Millington and Quirk's model (Eq. 21) [57], D_{disp} is the dispersion coefficient, which has been incorporated into an MCDI process model to account for the hydrodynamic dispersion effects in spacer-filled channel by Zhang and Reible [58], and is given by [59]:

$$D_{disp} = D_i + \lambda \frac{U}{\varepsilon_s} \tag{2.22}$$

where λ is the dispersivity.

In some simulations, an open channel is considered for simplicity and ion transport in channel is simulated by inserting a stagnant diffusion layer (SDL) between either channel and electrode or channel and IEM (if employed). SDL has also been employed to simulate ion transport between the electrode channel and IEM in FCDI [60]. Zhao et al. [13] employed NP equation to account for ion transport flux in the SDL with fixed thickness. The extent of turbulence and ion mixing degree in the channel together impact SDL thickness [54]. Perez et al. [61] revealed that SDL thickness increased with decreasing flow rate until a well-developed region was achieved, where SDLs overlapped. In the developing region, SDL thickness increased along with cell length in the flow direction [61]. Considering the commonly negligible concentration polarization in a porous-media spacer filled channel due to dispersion effects [62], the assumption of SDL may not be applicable.

Alternatively, ion transport in the spacer-filled channel has been simplified by treating the channel as a plug flow reactor (PFR), which can be divided into a series of continuous stirred-tank reactors (CSTRs). The dead volume between the cell exit and

the conductivity sensor, including the volume of the effluent solution in the tube and the "probe cell", has also been simulated as a CSTR considering the reduced concentration gradients from dispersion and advection effects [63, 64].

2.4.2.3 Ion transport in IEM

IEM is employed in MCDI, FCDI and some of the intercalation electrode assembled CDI. Since flow direction is tangential to IEM, feed water flowing through IEM is usually ignored. However, electroosmotic and osmotic flow through IEM become significant under relatively high feed water concentration and should be incorporated into the flow balance [65].Co-ions' permeation can be ignored for simplicity when fixed charge density on IEM is much higher compared to the concentration outside IEM [60]. The permeation of co-ions through IEM becomes significant when concentration difference inside and outside the IEM gets smaller [28]. Ion transport in IEM can be described by mass balance with NP flux:

$$\varepsilon_w \frac{\partial c_{m,i}}{\partial t} = \nabla \cdot (D_{m,i} \nabla c_{m,i} + \frac{z_i D_{m,i} F c_{m,i}}{RT} \nabla \varphi_m) \tag{2.23}$$

$$D_{m,i} = D_i^0 [\varepsilon_w / (2 - \varepsilon_w)]^2 \tag{2.24}$$

where ε_w is the IEM's water uptake volume fraction, which is the ratio of solution volume over swollen IEM's volume, $c_{m,i}$ is the concentration of species i in IEM, φ_m is the electrolyte potential in IEM, and $D_{m,i}$ is the effective diffusion coefficient of species i in IEM corrected by Mackie and Meares's model (Eq. 24) [66]. Rommerskirchen et

al. [65] introduced a constriction factor to estimate $D_{m,i}$ in the existence of large concentration gradient in IEM.

Charge balance inside IEM is given by:

$$\sum z_i c_{m,i} + z_F c_F = 0 \tag{2.25}$$

where z_F is the valence of the fixed charges on IEM, and c_F is the fixed charge density in IEM.

Under the relatively high concentration of counter-ions and the relatively strong electrostatic force between the fixed charges and ions in IEM, Hassanvand et al. [5] considered the non-ideality of the solution in IEM by replacing ions' concentration with activity using Manning's counter-ion condensation theory to calculate ions' activity coefficient.

2.4.2.4 Boundary and initial conditions

Concentration and electrolyte potential are continuous within each cell element such as the channel, electrode and IEM. Concentration flux and current density are continuous throughout the cell. Zero fluxes of both concentration and potential are set on the outside surface of the electrode pair. On the boundaries of IEM, concentration and potential possess step changes following Donnan theory:

$$\varphi_{m,c} - \varphi = \frac{RT}{z_i F} ln \frac{c_i}{c_{m,i}} \tag{2.26}$$

$$\varphi_{m,e} - \varphi_{ma} = \frac{RT}{z_i F} ln \frac{c_{ma,i}}{c_{m,i}} \tag{2.27}$$

where $\varphi_{m,c}$ and $\varphi_{m,e}$ are the electrolyte potentials in IEM at IEM-channel interface and IEM-electrode interface, respectively.

Initial conditions are based on experimental setup. Usually a uniform concentration distribution in the channel and electrode macropores is used as the initial condition assuming the same concentration as the feed solution. Initial potential and current density are zero. Initially EDL is unestablished so Stern layer potential drop and Donnan potential are zero. Initial concentration in IEM and electrode micropores can be calculated based on Donnan theory and mD theory and its extensions, respectively.

2.4.2.5 Model dimensions

Three-dimension models are not yet available due to the complexity of solving the fully-coupled nonlinear partial differential equations (PDEs). Hence, dimension reduction is necessary to facilitate numerical convergence. Fully coupled two-dimension models have been developed and solved for CV single-pass mode CDI [6, 55, 56] and MCDI [58] by omitting the variations of parameters in the width direction, but are not available for CC mode (M)CDI yet. Fully-coupled two-dimension models possess relatively high accuracy but suffer from numerical issues under a wider operating conditions especially for multicomponent system. Hence, simplifications such as considering the cell to be symmetric, applying the same diffusion coefficient for all ions, and ignoring concentration variations in the thickness direction within the channel or electrode have been employed. These simplified two-dimension models are applicable for both CC and CV modes (M)CDI [5, 10, 28, 37, 39, 47, 63, 67]. One-dimension models further omit

the variations of parameters in the length direction [64, 68, 69], which holds for flow-through CDI and conventional CDI with relatively short length.

The input parameters for the model include operating parameters, physical and chemical property parameters of cell elements, and geometry parameters. Due to the sufficient pressure exerted on cell elements during cell assembling to reduce contact resistance between electrode and current collector, the thickness and porosity of cell elements may change after assembly, reducing the accuracy of measurement. Dykstra et al. [38] proposed a novel method by measuring the system resistance to estimate the spacer thickness and porosity after assembly.

Numerical solutions of one-dimension and two-dimension models can be obtained by software such as MATLAB [7, 16, 70], COMSOL [6, 55, 56, 58] and gPROMS ModelBuilder [60, 65]. Porada et al. [2] proposed a zero-dimension dynamic process model for batch mode CDI by employing mD theory to simulate ion adsorption and treating the channel as a CSTR. Due to the simplicity, this zero-dimension model can be solved in Excel.

2.4.2.6 Model application

The mD theory based models are feasible for simulating the spatiotemporal ion transport and adsorption behaviors in conventional CDI, MCDI and the enhanced CDI architectures such as flow-through CDI [64, 69], FCDI [16, 60, 65, 68], and I-CDI [45]. These models can also simulate the dynamics of capacitive mixing, which is also known as “blue energy” and can be considered as an inverse process of CDI for harvesting

energy from the salinity gradients of river waters and seawaters at estuary entry [71, 72]. The changes in pH [47] and chemical surface charges [49] caused by Faradaic reactions can be simulated in the model. The effects of operating conditions, feed water salinity and composition, ion valence, ion size, and ion diffusion coefficient on ion selective removal can be evaluated [42, 67, 73, 74]. Zhao et al. [13] explained the time-dependent ion selectivity in a single-pass CV mode CDI by analyzing the transient interplay between electrostatic force and ion electromigration rate via mD theory.

The simulated transient concentration distribution in cell elements, effluent concentration, Stern layer potential drop, Donnan potential and current density can be employed to estimate the ion transport resistance [38] and energy consumption as indicated by specific energy consumption (SEC), thermodynamic energy efficiency (TEE) [70, 75], or energy losses in each cell element [16]. Wang et al. [76] proposed a reversible thermodynamic cycle via mD theory, which was applicable for intuitively evaluating TEE and giving insights to improving TEE by adjusting operating conditions.

Overall, CDI process models have been employed to optimize cell performance metrics including average salt adsorption rate, salt adsorption capacity, salt removal efficiency, charge efficiency, SEC, TEE, water recovery and water productivity by theoretically adjusting electrode physiochemical properties, cell geometry, cycle mode, flow mode, and operating conditions [7, 10, 28, 37, 39, 58, 63, 68]. Trade-offs between kinetic efficiency and energy efficiency [6, 55, 77], water recovery and TEE [68], water recovery and water productivity [5], and SEC and water productivity [78] have been

observed, indicating simultaneous optimization of all the performance metrics are impossible. Hence, trade-off curves can be simulated under varying operating conditions to obtain the operating range with relatively optimal of both metrics of interest [77, 78]. Salamat and Hidrovo [6] proposed a combined performance metric including salt removal efficiency, water productivity, salt removal rate, and water recovery to explore the relatively optimal operating conditions.

2.5. Alternative CDI models

Besides mD theory based CDI models, other models mainly including isotherm and kinetic models, dynamic Langmuir models, and equivalent circuit models, have been employed for CDI simulation. The development and key equations of these models are displayed in the following sections.

2.5.1 Isotherm and kinetic models

Isotherm models including Langmuir, Freundlich, Brunauer-Emmett-Teller (BET), and Frumkin isotherms have been employed to fit the experimental observed isotherms (adsorption amount versus concentration at equilibrium) in CDI [79-85]. The equations and the physical meanings of the parameters of the isotherm models used for CDI are given in Table 2.1.

Table 2.1. Isotherm models used for CDI

Isotherm model	Equation	Parameter	Physical meaning
Langmuir	$q = \frac{q_m b C}{1 + bC}$	q	Equilibrium adsorption
		q_m	Theoretical saturation adsorption amount
		b	Langmuir isotherm constant
		C	Equilibrium concentration
Freundlich	$q = K_F C^{\frac{1}{n}}$	q	Equilibrium adsorption
		K_F	Freundlich constant
		n	Freundlich constant
		C	Equilibrium concentration
BET	$q = \frac{q_{m,BET} C_{BET} C}{(C - C_s)[1 + (C_{BET} - 1)\frac{C}{C_s}]}$	q	Equilibrium adsorption
		$q_{m,BET}$	Theoretical saturation adsorption amount
		C_{BET}	BET constant indicating the interaction energy between ion and surface
		C_S	BET constant indicating the monolayer saturation ion concentration
		C	Equilibrium concentration
Frumkin	$\frac{\theta}{1 - \theta} e^{-2A\theta} = \beta C$	θ	Surface coverage of ions
		A	Frumkin constant indicating lateral interaction among adsorbed ions

Table 2.1. Continued

		β	Frumkin constant indicating adsorption strength
		C	Equilibrium concentration

The Langmuir model typically gives a better fit and a higher correlation coefficient compared to other isotherm models. However, Li et al. [86] revealed that Freundlich isotherm showed a better fit for a graphene assembled CDI. Chen et al. [87] fitted the experimental observed isotherm better with Freundlich isotherm for phosphate adsorption in CDI. Gaikwad and Balomajumder [88] achieved a better fit for the electrosorption of both cations and anions in CDI with an extended Freundlich isotherm.

For batch mode CDI, cell dynamics have been simulated by Lagergren first-order and second-order models, and intraparticle diffusion model [82, 86-90]. The equations and the physical meanings of the parameters of the kinetic models used for batch mode CDI are given in Table 2.2.

Table 2.2. Kinetic models used for batch mode CDI

Kinetic model	Equation	Parameter	Physical meaning
Lagergren first-order model	$\ln(q_e - q_t) = lnq_e - k_1 t$	q_e	Equilibrium adsorption amount
		q_t	Transient adsorption amount
		k_1	First-order rate constant
		t	Operating duration
Lagergren second-order model	$\frac{1}{q_t} = \frac{1}{k_2 q_e^2} + \frac{t}{q_e}$	q_t	Transient adsorption amount
		k_2	Second-order rate constant
		q_e	Equilibrium adsorption amount
		t	Operating duration
Intraparticle diffusion model	$q_t = k_{id} t^{1/2} + C_{id}$	q_t	Transient adsorption amount
		k_{id}	Intraparticle diffusion rate constant
		C_{id}	Intraparticle diffusion constant indicating non-electrostatic adsorption.
		t	Operating duration

Lagergren first-order model generally displays the highest regression coefficient compared to other kinetic models for fitting the experimentally obtained transient effluent concentration curves. Li et al. [80] argued that whether first-order model or second-order model had a better fit largely depended on the electrode material. Ma et al. [90] achieved a higher fit with an intraparticle diffusion model under relatively low feed water salinity, where ion adsorption resistance became significant.

For single-pass mode CDI, the adsorption and desorption processes have been simulated with simple differential reaction equations [91, 92] and modified transient capacitor equations [93, 94]. Jande and Kim [95] modified their single-pass mode models by adding a CSTR at the cell exit and correlating the effluent concentration to the inlet concentration to simulate the dynamics of batch mode CDI. Expressions and the influencing factors of the minimal effluent concentration were explored in both single-pass and batch modes [93-95].

2.5.2 Dynamic Langmuir models

Nordstrand and Dutta [96] recently improved Langmuir isotherm to form a dynamic Langmuir (DL) model by considering the reduced effective adsorption sites due to co-ion repulsion and competitive adsorption in multicomponent solution in CDI, and relating the adsorption sites to the applied voltage. The dynamic adsorption equation of DL model is given by:

$$\frac{dc_{ads}^{i}}{dt} = k_{ads}^{i} c^{i}\left(\mathrm{S} - \beta_0^i - \beta_1^i c_0^i - \textstyle\sum_i z^i c_{ads}^i\right) - k_{des}^{i} c_{ads}^{i} \tag{2.28}$$

where c^i_{ads} is the adsorbed concentration of species i, t is the operating duration, k^i_{ads} and k^i_{des} are the rate constants of species i for adsorption and desorption, respectively, S is the total adsorption sites, β^i_0 and β^i_1 are the constants accounting for co-ion repulsion effects, z^i is the ion valence of species i, and c^i and c^i_0 are the transient and initial concentrations of species i. Ions evaluated in the same equation should possess the same charge sign.

When electrode saturation is reached, the term on the left-hand side of Eq. (2.28) vanishes and transient concentration terms become the same as the initial concentration in single-pass mode CDI. Hence, the ion adsorption amount, charge storage and charge efficiency at equilibrium in single-pass mode CDI can be simulated.

In order to describe the dynamic behavior of CDI, Nordstrand et al. [97] simplified Eq. (2.28) by assuming that the transient concentration changes in the cell did not affect the adsorption rate so c^i can be replaced by c^i_0. For single salt solution, DL adsorption equation is rewritten as:

$$\frac{dc_{ads}}{dt} = (k_{ads}(\mathrm{S} - \beta_0)c_0 - k_{ads}\beta_1 c_0^2) - (k_{ads}c_0 z + k_{des})c_{ads} = K_a - K_b c_{ads} \quad (2.29)$$

where K_a and K_b are the comprehensive constants. The adsorption rate was correlated with the transient effluent concentration by treating the channel as a CSTR:

$$\frac{dc}{dt} = -\frac{dc_{ads}}{dt} + \frac{Q}{V}(c_0 - c) \quad (2.30)$$

where Q is the flow rate of the feed solution, and V is the volume of the channel. By coupling Eq. (2.29) and Eq. (2.30), K_a and K_b can be fitted from the experimentally observed transient effluent concentration curves using a published MATLAB based program [97], enabling a convenient implementation of this model for users.

DL model can be simplified by assuming the same charge efficiency for different ions to estimate the relative adsorption of different ions at equilibrium in a multicomponent solution. This relative adsorption was related to the equilibrium concentration and a

proposed competitiveness metric, which was related to the rate constants of adsorption and desorption [98]:

$$\frac{c_{ads}^{i}}{c_{ads}^{j}} = \frac{k_{ads}^{i}/k_{des}^{i}c_{e}^{i}}{k_{ads}^{j}/k_{des}^{j}c_{e}^{j}} = \alpha_{i,j}\frac{c_{e}^{i}}{c_{e}^{j}} \tag{2.31}$$

where c^{i}_{e} and c^{j}_{e} are the concentrations of species *i* and *j* at equilibrium, respectively, and $\alpha_{i,j}$ is the competitiveness metric of *i* over *j* and equals to the ratio of the competitiveness metric of species *i* over a baseline ion *b*, $\alpha_{i,b}$, over the competitiveness metric of species *j* over *b*, $\alpha_{j,b}$:

$$\alpha_{i,j} = \frac{\alpha_{i,b}}{\alpha_{j,b}} \tag{2.32}$$

Nordstrand and Dutta [99] assumed both adsorption amount and concentration change in the channel were negligible at the beginning of adsorption process, so the adsorption equation of DL model was simplified to be:

$$\frac{dc_{ads}^{i}}{dt} = k_{ads}^{i}c_{0}^{i}\left(\mathrm{S} - \beta_{0}^{i} - \beta_{1}^{i}c_{0}^{i}\right) \tag{2.33}$$

By assuming the same charge efficiency for different ions, the relative adsorption of different ions at the beginning of adsorption is only related to the adsorption rate constants and initial concentrations of different ions:

$$\frac{c_{ads}^{i}}{c_{ads}^{j}} = \frac{k_{ads}^{i}c_{0}^{i}}{k_{ads}^{j}c_{0}^{j}} \tag{2.34}$$

However, the assumption of negligible concentration changes in the channel is impractical considering the rapid reduction of the effluent concentration observed at the beginning of adsorption in CDI experiments [2].

2.5.3 Equivalent circuit models

The simplest equivalent circuit of CDI is a resistor-capacitor (RC) circuit by treating the electrode pair as a capacitor and the system resistance as a resistor [100]. The expressions and physical meanings of the parameters of resistive energy losses of CV and CC modes CDI are summarized in Table 2.3.

Table 2.3. Resistive energy losses of CV and CC modes CDI with RC circuit

CDI mode	Resistive energy losses	Parameter	Physical meaning
CV mode	$E_{CV}(t) = \frac{1}{2} C V_{CV}^2 (1 - e^{-\frac{2t}{RC}})$	$E_{CV}(t)$	Transient resistive energy losses in CV mode CDI
		T	Operating duration
		R	System resistance
		C	Cell capacitance
		V_{CV}	Applied voltage in CV mode CDI
CC mode	$E_{CC}(t) = I_{CC}^2 R t$	$E_{CC}(t)$	Transient resistive energy losses in CC mode CDI
		T	Operating duration
		I_{CC}	Applied current in CC mode CDI
		R	System resistance

Randles circuit is more complicated than RC circuit and has been used to simulate dynamics in a supercapacitor [101, 102]. Qin et al. [103] employed a simplified Randles circuit by simulating the electrode pair as a capacitor, which was in parallel connection

with a resistor that accounted for the polarization and current leakage resistances, and adding a resistor in serial to account for the ion transport resistance and contact resistance, to simulate energy behaviors of CC single-pass mode MCDI. The deviations between the estimated SEC and TEE values achieved by simple Randles circuit model and by mD theory based 1-d dynamic model were proven to be small [75]. However, Randles circuit models are too simple for a comprehensive resistance analysis.

The classical transmission line (TL) model simulates each porous electrode with a dozen or more of Randles circuit units [100, 104]. A schematic diagram of TL model used for CDI is shown in Figure 2.1 [104]. Within each unit, the capacitor, C_{0N}, is in parallel connection with the leakage resistor, R_{0N}. The coupled capacitor and leakage resistor are in serial connection with the electrode electronic resistance, R_{eN}, and the ion transport resistance in electrode macropores, R_{iN}. Between the two series of Randles circuit units, contact resistance at electrode-current collector interface, R_{ct}, and a combination of the ion transport resistance in channel and external resistance, R_s, are in serial connection. TL models can be built and solved in LTspice software. The leakage current can be simulate by Butler-Volmer equation.

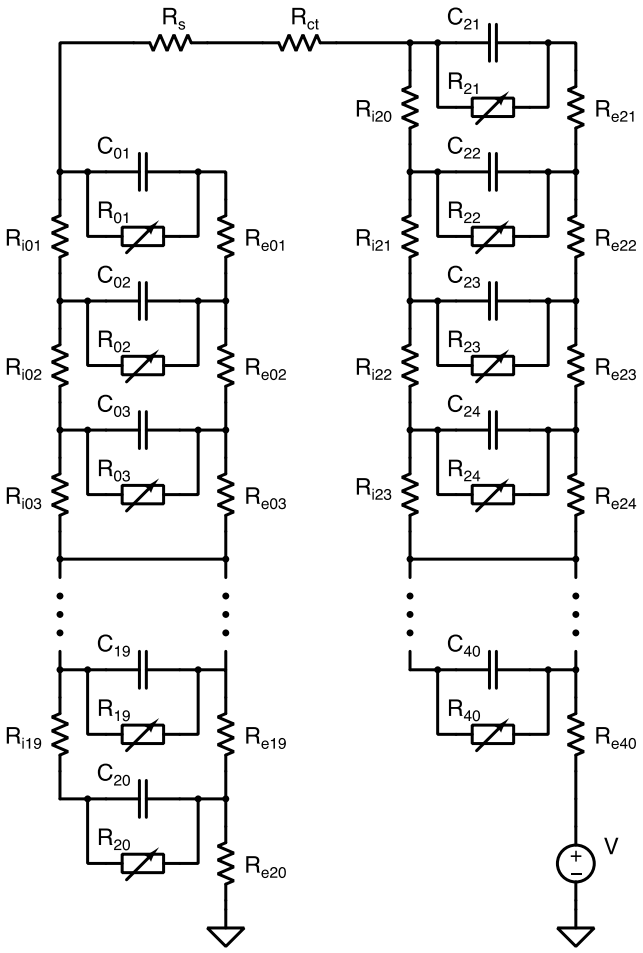

Figure 2.1. Schematic diagram of TL model for CDI [104].

Equivalent circuit models have been employed to directly estimate energy consumption and resistive and parasitic energy losses in CDI [100, 103-106], or couple transport equations to simulate transient effluent concentration curves [23, 107]. Nordstrand and Dutta [108] first simulated the adsorption rate with Randles circuit models, and then assumed this adsorption rate to be identical throughout the electrode. This adsorption rate was then inserted into two-dimension transport equations. This "relaxed coupling" of transport and adsorption processes reduced the computational complexity and

simplified the simulation of full size CDI modules, though at the expense of reducing accuracy. Charge efficiency in equivalent circuit models can be expressed as the multiplication of EDL, Coulombic and flow efficiencies [106].

2.6. Comparison of various CDI models

Based on the analyses of the four types CDI models in Section 2.4 and Section 2.5, comparisons of these models regarding the capture of electrosorption mechanisms and Faradaic reactions, the computation simplicity and the application scope are summarized in Table 2.4.

Table 2.4. Comparisons of the four types CDI models

CDI models	**Electrosorption mechanisms**	**Faradaic reactions**	**Calculation simplicity**	**Application scope**
Modified Donnan based CDI models	★★★	★★½	★½☆	★★★
Isotherm and kinetic models	★☆☆	☆☆☆	★★★	★☆☆
Dynamic Langmuir models	★★☆	☆☆☆	★★☆	★½☆
Equivalent circuit models	★★☆	★★☆	★★½	★★☆

Overall, among the four types of CDI models, mD theory based models are the most mature and widely used for optimizing cell design and operating conditions of various CDI architectures, but possess computation sophistication for multi-dimensional and multicomponent system models. Although isotherm and kinetic models can be easily implemented and have been applied to fitting the experimentally observed isotherm and effluent concentration curves, the effects of operating parameters and cell geometry cannot be evaluated due to the lack of intrinsic mechanisms of electrosorption.

Compared to Langmuir model, DL models are advanced by introducing the effects of applied voltage and co-ion repulsion and can be used for estimating charge efficiency and selective ion removal at equilibrium, but Faradaic reactions have not been simulated. Some assumptions made in the modified DL models require modification to broaden the applicable range of DL models and to better simulate CDI dynamics under both CC and CV modes. Equivalent circuit models are well-balanced in the four indicators investigated, and hence can be alternatives to mD theory based CDI models for directly predicting dynamic voltage and current curves and evaluating energy consumption and energy efficiency. However, equivalent circuit models are not currently capable of simulating the dynamics of multicomponent solution in CDI.

Nordstrand and Dutta [107, 109] proposed a so-called “system identification” method for equivalent circuit models to extract parameters from consecutive cycles simultaneously, which lowered the error accumulation and largely improved the simulation accuracy.

2.7. Concluding remarks

This review focuses on electrode-scale CDI models and proposes a comprehensive CDI process model by incorporating the published mD theory and its extensions into macroscopic transport equations. This comprehensive CDI process model is capable of capturing the modifications of electrodes, pH changes, and Faradaic reactions for a variety of CDI architectures, such as conventional CDI, MCDI, flow-through CDI, FCDI, and I-CDI. Other models used for simulating CDI including isotherm and kinetic

models, DL models, and equivalent circuit models have also been introduced. Comparisons between the four type CDI models have been made regarding the capture of electrosorption mechanisms and Faradaic reactions, computation simplicity and application scope. Overall, mD theory based CDI models are the most mature and can be applied to a broad range of conditions. Equivalent circuit models can serve as alternatives to estimate energy behaviors of CDI, but are currently not able to simulate ion selective removal in multicomponent solution. DL models do not currently incorporate Faradaic effects and are limited in their range of applications.

2.8 References

[1] J. W. Blair and G. W. Murphy, "Electrochemical demineralization of water with porous electrodes of large surface area," ACS Publications, 1960.

[2] S. Porada, R. Zhao, A. Van Der Wal, V. Presser, and P. Biesheuvel, "Review on the science and technology of water desalination by capacitive deionization," *Progress in materials science,* vol. 58, no. 8, pp. 1388-1442, 2013.

[3] M. Suss, S. Porada, X. Sun, P. Biesheuvel, J. Yoon, and V. Presser, "Water desalination via capacitive deionization: what is it and what can we expect from it?," *Energy & Environmental Science,* vol. 8, no. 8, pp. 2296-2319, 2015.

[4] W. Tang, J. Liang, D. He, J. Gong, L. Tang, Z. Liu, D. Wang, and G. Zeng, "Various cell architectures of capacitive deionization: recent advances and future trends," *Water Res.,* vol. 150, pp. 225-251, 2019.

[5] A. Hassanvand, G. Q. Chen, P. A. Webley, and S. E. Kentish, "Improvement of MCDI operation and design through experiment and modelling: Regeneration with brine and optimum residence time," *Desalination,* vol. 417, pp. 36-51, 2017.

[6] Y. Salamat and C. H. Hidrovo, "A parametric study of multiscale transport phenomena and performance characteristics of capacitive deionization systems," *Desalination,* vol. 438, pp. 24-36, 2018.

[7] X. Shang, R. D. Cusick, and K. C. Smith, "A combined modeling and experimental study assessing the impact of fluid pulsation on charge and energy efficiency in capacitive deionization," *Journal of The Electrochemical Society,* vol. 164, no. 14, p. E536, 2017.

[8] A. Ramachandran, S. A. Hawks, M. Stadermann, and J. G. Santiago, "Frequency analysis and resonant operation for efficient capacitive deionization," *Water Res.,* vol. 144, pp. 581-591, 2018.

[9] S. Porada, L. Weinstein, R. Dash, A. Van Der Wal, M. Bryjak, Y. Gogotsi, and P. Biesheuvel, "Water desalination using capacitive deionization with microporous carbon electrodes," *ACS applied materials & interfaces,* vol. 4, no. 3, pp. 1194-1199, 2012.

[10] S. Porada, L. Borchardt, M. Oschatz, M. Bryjak, J. Atchison, K. Keesman, S. Kaskel, P. Biesheuvel, and V. Presser, "Direct prediction of the desalination performance of porous carbon electrodes for capacitive deionization," *Energy & Environmental Science,* vol. 6, no. 12, pp. 3700-3712, 2013.

[11] C.-H. Hou, C. Liang, S. Yiacoumi, S. Dai, and C. Tsouris, "Electrosorption capacitance of nanostructured carbon-based materials," *Journal of colloid and interface science,* vol. 302, no. 1, pp. 54-61, 2006.

[12] K.-L. Yang, T.-Y. Ying, S. Yiacoumi, C. Tsouris, and E. S. Vittoratos, "Electrosorption of ions from aqueous solutions by carbon aerogel: an electrical double-layer model," *Langmuir,* vol. 17, no. 6, pp. 1961-1969, 2001.

[13] R. Zhao, M. Van Soestbergen, H. Rijnaarts, A. Van der Wal, M. Bazant, and P. Biesheuvel, "Time-dependent ion selectivity in capacitive charging of porous electrodes," *Journal of colloid and interface science,* vol. 384, no. 1, pp. 38-44, 2012.

[14] R. Kalluri, M. Biener, M. Suss, M. Merrill, M. Stadermann, J. Santiago, T. Baumann, J. Biener, and A. Striolo, "Unraveling the potential and pore-size dependent capacitance of slit-shaped graphitic carbon pores in aqueous electrolytes," *Physical Chemistry Chemical Physics,* vol. 15, no. 7, pp. 2309-2320, 2013.

[15] M. Jiménez, M. Fernandez, S. Ahualli, G. Iglesias, and A. Delgado, "Predictions of the maximum energy extracted from salinity exchange inside porous electrodes," *Journal of colloid and interface science,* vol. 402, pp. 340-349, 2013.

[16] L. Wang, C. Zhang, C. He, T. D. Waite, and S. Lin, "Equivalent film-electrode model for flow-electrode capacitive deionization: Experimental validation and performance analysis," *Water Research,* vol. 181, p. 115917, 2020.

[17] R. Zhao, P. Biesheuvel, H. Miedema, H. Bruning, and A. Van der Wal, "Charge efficiency: a functional tool to probe the double-layer structure inside of porous electrodes and application in the modeling of capacitive deionization," *The Journal of Physical Chemistry Letters,* vol. 1, no. 1, pp. 205-210, 2010.

[18] P. Biesheuvel, B. Van Limpt, and A. Van der Wal, "Dynamic adsorption/desorption process model for capacitive deionization," *The journal of physical chemistry C,* vol. 113, no. 14, pp. 5636-5640, 2009.

[19] A. Hemmatifar, D. I. Oyarzun, J. W. Palko, S. A. Hawks, M. Stadermann, and J. G. Santiago, "Equilibria model for pH variations and ion adsorption in capacitive deionization electrodes," *Water research,* vol. 122, pp. 387-397, 2017.

[20] S. Liu, V. Q. Do, and K. C. Smith, "Modeling of Electrochemical Deionization Across Length Scales: Recent Accomplishments and New Opportunities," *Current Opinion in Electrochemistry,* 2020.

[21] X. Liu, S. Shanbhag, T. V. Bartholomew, J. F. Whitacre, and M. S. Mauter, "Cost Comparison of Capacitive Deionization and Reverse Osmosis for Brackish Water Desalination," *ACS ES&T Engineering,* 2020.

[22] S. Hand, J. S. Guest, and R. D. Cusick, "Technoeconomic analysis of brackish water capacitive deionization: navigating tradeoffs between performance, lifetime, and material costs," *Environmental Science & Technology,* vol. 53, no. 22, pp. 13353-13363, 2019.

[23] T. D. Hasseler, A. Ramachandran, W. A. Tarpeh, M. Stadermann, and J. G. Santiago, "Process design tools and techno-economic analysis for capacitive deionization," *Water Res.,* vol. 183, p. 116034, 2020.

[24] M. Z. Bazant, K. Thornton, and A. Ajdari, "Diffuse-charge dynamics in electrochemical systems," *Physical review E,* vol. 70, no. 2, p. 021506, 2004.

[25] H. Helmholtz, "Uber einige Gesetze der Vertheilung elektrischer Strome in korperlichen Leitem, mit Anwendung auf die thierisch-elektrischen Versuche," *Ann. Phys. Chem,* vol. 89, p. 21, 1853.

[26] O. Stern, "Zur theorie der elektrolytischen doppelschicht," *Zeitschrift für Elektrochemie und angewandte physikalische Chemie,* vol. 30, no. 21‐22, pp. 508-516, 1924.

[27] M. Müllier and B. Kastening, "The double layer of activated carbon electrodes: Part 1. The contribution of ions in the pores," *Journal of Electroanalytical Chemistry,* vol. 374, no. 1-2, pp. 149-158, 1994.

[28] P. Biesheuvel, R. Zhao, S. Porada, and A. Van der Wal, "Theory of membrane capacitive deionization including the effect of the electrode pore space," *Journal of colloid and interface science,* vol. 360, no. 1, pp. 239-248, 2011.

[29] I. Borukhov, D. Andelman, and H. Orland, "Adsorption of large ions from an electrolyte solution: a modified Poisson–Boltzmann equation," *Electrochimica Acta,* vol. 46, no. 2-3, pp. 221-229, 2000.

[30] I. Borukhov, D. Andelman, and H. Orland, "Steric effects in electrolytes: A modified Poisson-Boltzmann equation," *Physical review letters,* vol. 79, no. 3, p. 435, 1997.

[31] T.-L. Horng, T.-C. Lin, C. Liu, and B. Eisenberg, "PNP equations with steric effects: a model of ion flow through channels," *The Journal of Physical Chemistry B,* vol. 116, no. 37, pp. 11422-11441, 2012.

[32] M. S. Kilic, M. Z. Bazant, and A. Ajdari, "Steric effects in the dynamics of electrolytes at large applied voltages. II. Modified Poisson-Nernst-Planck equations," *Physical review E,* vol. 75, no. 2, p. 021503, 2007.

[33] H. Wang, A. Thiele, and L. Pilon, "Simulations of cyclic voltammetry for electric double layers in asymmetric electrolytes: A generalized modified poisson–nernst–planck model," *The Journal of Physical Chemistry C,* vol. 117, no. 36, pp. 18286-18297, 2013.

[34] J. S. Newman and C. W. Tobias, "Theoretical analysis of current distribution in porous electrodes," *Journal of The Electrochemical Society,* vol. 109, no. 12, p. 1183, 1962.

[35] A. Johnson and J. Newman, "Desalting by means of porous carbon electrodes," *Journal of the Electrochemical Society,* vol. 118, no. 3, pp. 510-517, 1971.

[36] J. Newman and W. Tiedemann, "Porous‐electrode theory with battery applications," *AIChE Journal,* vol. 21, no. 1, pp. 25-41, 1975.

[37] T. Kim, J. Dykstra, S. Porada, A. Van Der Wal, J. Yoon, and P. Biesheuvel, "Enhanced charge efficiency and reduced energy use in capacitive deionization by increasing the discharge voltage," *Journal of colloid and interface science,* vol. 446, pp. 317-326, 2015.

[38] J. Dykstra, R. Zhao, P. Biesheuvel, and A. Van der Wal, "Resistance identification and rational process design in capacitive deionization," *Water Res.,* vol. 88, pp. 358-370, 2016.

[39] R. Zhao, O. Satpradit, H. Rijnaarts, P. Biesheuvel, and A. Van der Wal, "Optimization of salt adsorption rate in membrane capacitive deionization," *Water Res.,* vol. 47, no. 5, pp. 1941-1952, 2013.

[40] D.-W. Chung, M. Ebner, D. R. Ely, V. Wood, and R. E. García, "Validity of the Bruggeman relation for porous electrodes," *Modelling and Simulation in Materials Science and Engineering,* vol. 21, no. 7, p. 074009, 2013.

[41] P. Biesheuvel and M. Van Soestbergen, "Counterion volume effects in mixed electrical double layers," *Journal of Colloid and Interface Science,* vol. 316, no. 2, pp. 490-499, 2007.

[42] E. N. Guyes, T. Malka, and M. E. Suss, "Enhancing the ion-size-based selectivity of capacitive deionization electrodes," *Environmental science & technology,* vol. 53, no. 14, pp. 8447-8454, 2019.

[43] M. E. Suss, "Size-based ion selectivity of micropore electric double layers in capacitive deionization electrodes," *Journal of The Electrochemical Society,* vol. 164, no. 9, p. E270, 2017.

[44] P. Biesheuvel, S. Porada, M. Levi, and M. Z. Bazant, "Attractive forces in microporous carbon electrodes for capacitive deionization," *Journal of solid state electrochemistry,* vol. 18, no. 5, pp. 1365-1376, 2014.

[45] P. Biesheuvel, H. Hamelers, and M. Suss, "Theory of water desalination by porous electrodes with immobile chemical charge," *Colloids and Interface Science Communications,* vol. 9, pp. 1-5, 2015.

[46] P. Biesheuvel, "Activated carbon is an electron-conducting amphoteric ion adsorbent," *arXiv preprint arXiv:1509.06354,* 2015.

[47] J. Dykstra, K. Keesman, P. Biesheuvel, and A. Van der Wal, "Theory of pH changes in water desalination by capacitive deionization," *Water research,* vol. 119, pp. 178-186, 2017.

[48] P. Biesheuvel, Y. Fu, and M. Bazant, "Electrochemistry and capacitive charging of porous electrodes in asymmetric multicomponent electrolytes," *Russian Journal of Electrochemistry,* vol. 48, no. 6, pp. 580-592, 2012.

[49] F. He, P. Biesheuvel, M. Z. Bazant, and T. A. Hatton, "Theory of water treatment by capacitive deionization with redox active porous electrodes," *Water Res.,* vol. 132, pp. 282-291, 2018.

[50] K. Singh, H. Bouwmeester, L. de Smet, M. Bazant, and P. Biesheuvel, "Theory of water desalination with intercalation materials," *Physical Review Applied,* vol. 9, no. 6, p. 064036, 2018.

[51] K. Singh, L. Zhang, H. Zuilhof, and L. de Smet, "Water desalination with nickel hexacyanoferrate electrodes in capacitive deionization: Experiment, model and comparison with carbon," *Desalination,* vol. 496, p. 114647, 2020.

[52] J. Gamaethiralalage, K. Singh, S. Sahin, J. Yoon, M. Elimelech, M. Suss, P. Liang, P. Biesheuvel, R. Zornitta, and L. de Smet, "Recent advances in ion selectivity with capacitive deionization," *Energy & Environmental Science,* 2021.

[53] C. Zhang, D. He, J. Ma, W. Tang, and T. D. Waite, "Faradaic reactions in capacitive deionization (CDI)-problems and possibilities: A review," *Water research,* vol. 128, pp. 314-330, 2018.

[54] P. Biesheuvel, Y. Fu, and M. Z. Bazant, "Diffuse charge and Faradaic reactions in porous electrodes," *Physical Review E,* vol. 83, no. 6, p. 061507, 2011.

[55] Y. Salamat and C. H. Hidrovo, "Significance of the micropores electro-sorption resistance in capacitive deionization systems," *Water Res.,* vol. 169, p. 115286, 2020.

[56] A. Hemmatifar, M. Stadermann, and J. G. Santiago, "Two-dimensional porous electrode model for capacitive deionization," *The Journal of Physical Chemistry C,* vol. 119, no. 44, pp. 24681-24694, 2015.

[57] R. Millington and J. Quirk, "Permeability of porous solids," *Transactions of the Faraday Society,* vol. 57, pp. 1200-1207, 1961.

[58] X. Zhang and D. Reible, "Exploring the Function of Ion-Exchange Membrane in Membrane Capacitive Deionization via a Fully Coupled Two-Dimensional Process Model," *Processes,* vol. 8, no. 10, p. 1312, 2020.

[59] J. Vanderborght, H. Vereecken, and I. Agrosphere IV, "Review of dispersivity lengths for transport modeling in soils," ed: Retrieved, 2018.

[60] A. Rommerskirchen, B. Ohs, K. A. Hepp, R. Femmer, and M. Wessling, "Modeling continuous flow-electrode capacitive deionization processes with ion-exchange membranes," *Journal of membrane science,* vol. 546, pp. 188-196, 2018.

[61] C. A. R. Perez, O. N. Demirer, R. L. Clifton, R. M. Naylor, and C. H. Hidrovo, "Macro analysis of the electro-adsorption process in low concentration nacl solutions for water desalination applications," *Journal of The Electrochemical Society,* vol. 160, no. 3, p. E13, 2013.

[62] S. Honarparvar, X. Zhang, T. Chen, C. Na, and D. Reible, "Modeling technologies for desalination of brackish water—toward a sustainable water supply," *Current Opinion in Chemical Engineering,* vol. 26, pp. 104-111, 2019.

[63] S. Porada, M. Bryjak, A. Van Der Wal, and P. Biesheuvel, "Effect of electrode thickness variation on operation of capacitive deionization," *Electrochimica Acta,* vol. 75, pp. 148-156, 2012.

[64] E. N. Guyes, A. N. Shocron, A. Simanovski, P. Biesheuvel, and M. E. Suss, "A one-dimensional model for water desalination by flow-through electrode capacitive deionization," *Desalination,* vol. 415, pp. 8-13, 2017.

[65] A. Rommerskirchen, M. Alders, F. Wiesner, C. J. Linnartz, A. Kalde, and M. Wessling, "Process model for high salinity flow-electrode capacitive deionization processes with ion-exchange membranes," *Journal of Membrane Science,* vol. 616, p. 118614, 2020.

[66] J. Mackie and P. Meares, "The diffusion of electrolytes in a cation-exchange resin membrane I. Theoretical," *Proceedings of the Royal Society of London. Series A. Mathematical and Physical Sciences,* vol. 232, no. 1191, pp. 498-509, 1955.

[67] J. Dykstra, J. Dijkstra, A. Van der Wal, H. Hamelers, and S. Porada, "On-line method to study dynamics of ion adsorption from mixtures of salts in capacitive deionization," *Desalination,* vol. 390, pp. 47-52, 2016.

[68] S. Hand, X. Shang, J. S. Guest, K. C. Smith, and R. D. Cusick, "Global sensitivity analysis to characterize operational limits and prioritize performance goals of capacitive deionization technologies," *Environmental science & technology,* vol. 53, no. 7, pp. 3748-3756, 2019.

[69] Y. Qu, P. G. Campbell, A. Hemmatifar, J. M. Knipe, C. K. Loeb, J. J. Reidy, M. A. Hubert, M. Stadermann, and J. G. Santiago, "Charging and transport dynamics of a flow-through electrode capacitive deionization system," *The Journal of Physical Chemistry B,* vol. 122, no. 1, pp. 240-249, 2018.

[70] L. Wang and S. Lin, "Membrane capacitive deionization with constant current vs constant voltage charging: which is better?," *Environmental science & technology,* vol. 52, no. 7, pp. 4051-4060, 2018.

[71] R. A. Rica, R. Ziano, D. Salerno, F. Mantegazza, M. Z. Bazant, and D. Brogioli, "Electro-diffusion of ions in porous electrodes for capacitive extraction of renewable energy from salinity differences," *Electrochimica Acta,* vol. 92, pp. 304-314, 2013.

[72] R. l. A. Rica, D. Brogioli, R. Ziano, D. Salerno, and F. Mantegazza, "Ions transport and adsorption mechanisms in porous electrodes during capacitive-mixing double layer expansion (CDLE)," *The Journal of Physical Chemistry C,* vol. 116, no. 32, pp. 16934-16938, 2012.

[73] W. Tang, P. Kovalsky, D. He, and T. D. Waite, "Fluoride and nitrate removal from brackish groundwaters by batch-mode capacitive deionization," *Water Res.,* vol. 84, pp. 342-349, 2015.

[74] W. Xing, J. Liang, W. Tang, G. Zeng, X. Wang, X. Li, L. Jiang, Y. Luo, X. Li, and N. Tang, "Perchlorate removal from brackish water by capacitive deionization: Experimental and theoretical investigations," *Chemical Engineering Journal,* vol. 361, pp. 209-218, 2019.

[75] M. Qin, A. Deshmukh, R. Epsztein, S. K. Patel, O. M. Owoseni, W. S. Walker, and M. Elimelech, "Response to comments on “comparison of energy consumption in desalination by capacitive deionization and reverse osmosis”," *Desalination,* vol. 462, pp. 48-55, 2019.

[76] L. Wang, P. Biesheuvel, and S. Lin, "Reversible thermodynamic cycle analysis for capacitive deionization with modified Donnan model," *Journal of colloid and interface science,* vol. 512, pp. 522-528, 2018.

[77] L. Wang and S. Lin, "Intrinsic tradeoff between kinetic and energetic efficiencies in membrane capacitive deionization," *Water research,* vol. 129, pp. 394-401, 2018.

[78] L. Wang and S. Lin, "Theoretical framework for designing a desalination plant based on membrane capacitive deionization," *Water research,* vol. 158, pp. 359-369, 2019.

[79] C. J. Gabelich, T. D. Tran, and I. M. Suffet, "Electrosorption of inorganic salts from aqueous solution using carbon aerogels," *Environmental science & technology,* vol. 36, no. 13, pp. 3010-3019, 2002.

[80] H. Li, L. Pan, T. Lu, Y. Zhan, C. Nie, and Z. Sun, "A comparative study on electrosorptive behavior of carbon nanotubes and graphene for capacitive deionization," *Journal of Electroanalytical Chemistry,* vol. 653, no. 1-2, pp. 40-44, 2011.

[81] M.-W. Ryoo, J.-H. Kim, and G. Seo, "Role of titania incorporated on activated carbon cloth for capacitive deionization of NaCl solution," *Journal of colloid and interface science,* vol. 264, no. 2, pp. 414-419, 2003.

[82] G. Wang, B. Qian, Q. Dong, J. Yang, Z. Zhao, and J. Qiu, "Highly mesoporous activated carbon electrode for capacitive deionization," *Separation and Purification Technology,* vol. 103, pp. 216-221, 2013.

[83] L. Wang, M. Wang, Z.-H. Huang, T. Cui, X. Gui, F. Kang, K. Wang, and D. Wu, "Capacitive deionization of NaCl solutions using carbon nanotube sponge electrodes," *Journal of Materials Chemistry,* vol. 21, no. 45, pp. 18295-18299, 2011.

[84] H. Li, L. Pan, Y. Zhang, L. Zou, C. Sun, Y. Zhan, and Z. Sun, "Kinetics and thermodynamics study for electrosorption of NaCl onto carbon nanotubes and carbon nanofibers electrodes," *Chemical Physics Letters,* vol. 485, no. 1-3, pp. 161-166, 2010.

[85] D. Liu, K. Huang, L. Xie, and H. L. Tang, "Relation between operating parameters and desalination performance of capacitive deionization with

activated carbon electrodes," *Environmental Science: Water Research & Technology,* vol. 1, no. 4, pp. 516-522, 2015.

[86] H. Li, T. Lu, L. Pan, Y. Zhang, and Z. Sun, "Electrosorption behavior of graphene in NaCl solutions," *Journal of Materials Chemistry,* vol. 19, no. 37, pp. 6773-6779, 2009.

[87] F.-F. Chen, H.-F. Li, X.-R. Jia, Z.-Y. Wang, X. Liang, Y.-Y. Qin, W.-Q. Chen, and T.-Q. Ao, "Characteristic and model of phosphate adsorption by activated carbon electrodes in capacitive deionization," *Separation and Purification Technology,* vol. 236, p. 116285, 2020.

[88] M. S. Gaikwad and C. Balomajumder, "Simultaneous electrosorptive removal of chromium (VI) and fluoride ions by capacitive deionization (CDI): Multicomponent isotherm modeling and kinetic study," *Separation and Purification Technology,* vol. 186, pp. 272-281, 2017.

[89] H. Li and L. Zou, "Ion-exchange membrane capacitive deionization: A new strategy for brackish water desalination," *Desalination,* vol. 275, no. 1-3, pp. 62-66, 2011.

[90] L. Ma, L. Huang, Y. Xu, C. Liu, F. Wang, H. Xing, and S. Ma, "Dynamics and Model Research on the Electrosorption by Activated Carbon Fiber Electrodes," *Water,* vol. 13, no. 1, p. 62, 2021.

[91] J.-H. Ryu, T.-J. Kim, T.-Y. Lee, and I.-B. Lee, "A study on modeling and simulation of capacitive deionization process for wastewater treatment," *Journal of the Taiwan Institute of Chemical Engineers,* vol. 41, no. 4, pp. 506-511, 2010.

[92] H. K. Mutha, H. J. Cho, M. Hashempour, B. L. Wardle, C. V. Thompson, and E. N. Wang, "Salt rejection in flow-between capacitive deionization devices," *Desalination,* vol. 437, pp. 154-163, 2018.

[93] Y. Jande and W.-S. Kim, "Predicting the lowest effluent concentration in capacitive deionization," *Separation and Purification Technology,* vol. 115, pp. 224-230, 2013.

[94] Y. Jande and W.-S. Kim, "Desalination using capacitive deionization at constant current," *Desalination,* vol. 329, pp. 29-34, 2013.

[95] Y. Jande and W.-S. Kim, "Modeling the capacitive deionization batch mode operation for desalination," *Journal of Industrial and Engineering Chemistry,* vol. 20, no. 5, pp. 3356-3360, 2014.

[96] J. Nordstrand and J. Dutta, "Dynamic Langmuir Model: A Simpler Approach to Modeling Capacitive Deionization," *The Journal of Physical Chemistry C,* vol. 123, no. 26, pp. 16479-16485, 2019.

[97] J. Nordstrand, K. Laxman, M. T. Z. Myint, and J. Dutta, "An Easy-to-Use Tool for Modeling the Dynamics of Capacitive Deionization," *The Journal of Physical Chemistry A,* vol. 123, no. 30, pp. 6628-6634, 2019.

[98] J. Nordstrand and J. Dutta, "Simplified Prediction of Ion Removal in Capacitive Deionization of Multi-Ion Solutions," *Langmuir,* vol. 36, no. 5, pp. 1338-1344, 2020.

[99] J. Nordstrand and J. Dutta, "Predicting and Enhancing the Ion Selectivity in Multi-Ion Capacitive Deionization," *Langmuir,* vol. 36, no. 29, pp. 8476-8484, 2020.

[100] Y. Qu, T. F. Baumann, J. G. Santiago, and M. Stadermann, "Characterization of resistances of a capacitive deionization system," *Environmental science & technology,* vol. 49, no. 16, pp. 9699-9706, 2015.

[101] C. Arbizzani, M. Mastragostino, and L. Meneghello, "Polymer-based redox supercapacitors: A comparative study," *Electrochimica Acta,* vol. 41, no. 1, pp. 21-26, 1996.

[102] C. Masarapu, H. F. Zeng, K. H. Hung, and B. Wei, "Effect of temperature on the capacitance of carbon nanotube supercapacitors," *ACS nano,* vol. 3, no. 8, pp. 2199-2206, 2009.

[103] M. Qin, A. Deshmukh, R. Epsztein, S. K. Patel, O. M. Owoseni, W. S. Walker, and M. Elimelech, "Comparison of energy consumption in desalination by capacitive deionization and reverse osmosis," *Desalination,* vol. 455, pp. 100-114, 2019.

[104] Y. Qu, P. G. Campbell, L. Gu, J. M. Knipe, E. Dzenitis, J. G. Santiago, and M. Stadermann, "Energy consumption analysis of constant voltage and constant current operations in capacitive deionization," *Desalination,* vol. 400, pp. 18-24, 2016.

[105] A. Ramachandran, D. I. Oyarzun, S. A. Hawks, M. Stadermann, and J. G. Santiago, "High water recovery and improved thermodynamic efficiency for capacitive deionization using variable flowrate operation," *Water Res.,* vol. 155, pp. 76-85, 2019.

[106] A. Ramachandran, D. I. Oyarzun, S. A. Hawks, P. G. Campbell, M. Stadermann, and J. G. Santiago, "Comments on “Comparison of energy consumption in desalination by capacitive deionization and reverse osmosis”," *Desalination,* vol. 461, no. LLNL-JRNL-770722, 2019.

[107] J. Nordstrand and J. Dutta, "An Extended Randles Circuit and a Systematic Model-Development Approach for Capacitive Deionization," *Journal of the Electrochemical Society*.

[108] J. Nordstrand and J. Dutta, "Relaxed Adsorption-flow Coupling Enables Stable COMSOL Modeling of Upscaled Capacitive Deionization."

[109] J. Nordstrand and J. Dutta, "Basis and Prospects of Combining Electroadsorption Modeling Approaches for Capacitive Deionization," *Physics,* vol. 2, no. 2, pp. 309-324, 2020.

CHAPTER 3

EXPLORING THE FUNCTION OF ION-EXCHANGE MEMBRANE IN MEMBRANE CAPACITIVE DEIONIZATION VIA A FULLY COUPLED TWO-DIMENSIONAL PROCESS MODEL[2]

3.1. Abstract

In the arid west, the freshwater supply of many communities is limited, leading to increased interest in tapping brackish water resources. Although reverse osmosis is the most common technology to upgrade saline waters, there is also interest in developing and improving alternative technologies. Here we focus on membrane capacitive deionization (MCDI), which has attracted broad attention as a portable and energy-efficient desalination technology. In this study, a fully coupled two-dimensional MCDI process model capable of capturing transient ion transport and adsorption behaviors was developed to explore the function of the ion-exchange membrane (IEM) and detect MCDI influencing factors via sensitivity analysis. The IEM enhanced desalination by improving the counter-ions' flux and increased adsorption in electrodes by encouraging retention of ions in electrode macropores. An optimized cycle time was proposed with maximal salt removal efficiency. The usage of the IEM, high applied voltage, and low flow rate were discovered to enhance this maximal salt removal efficiency. IEM properties including water uptake volume fraction, membrane thickness, and fixed charge density had a marginal impact on cycle time and salt removal efficiency within certain limits, while increasing cell length and electrode thickness and decreasing channel thickness and dispersivity significantly improved overall performance.

[2] This chapter is reproduced from the paper published as: Zhang X, Reible D. Exploring the Function of Ion-Exchange Membrane in Membrane Capacitive Deionization via a Fully Coupled Two-Dimensional Process Model [J]. Processes, 2020, 8(10): 1312.

3.2. Introduction

Freshwater is essential in our daily life with diverse demands for drinking water, agricultural irrigation, and industrial water. Demand for freshwater combined with the potential for supply disruptions from climate change have exacerbated freshwater scarcity [1]. Alternative technologies for providing freshwater are increasingly sought including desalinating saline water due to abundant seawater and brackish groundwater resources [2-4]. Although thermal distillation and reverse osmosis are the most popular desalination techniques [4], capacitive deionization (CDI) exhibits potential advantages including tunable effluent concentration, selective ion removal capability, high and flexible water recovery, simple pretreatment procedures and reduced fouling and scaling problems, particularly when treating low salinity brackish water [5, 6]. CDI may be particularly appropriate for low volume water desalination [7]. However, due to developments in flow-electrode CDI, increased productivity and continuous electrosorption have expanded its applicability [8, 9].

Membrane capacitive deionization (MCDI) is a modification of conventional CDI that has ion-exchange membrane (IEM) on electrodes [6, 10]. Schematic graphs of MCDI depicting both desalination and regeneration processes are shown in Figure 3.1. Cation-exchange membrane (CEM) and anion-exchange membrane (AEM) are inserted between a spacer-filled channel and a pair of porous electrodes. During desalination,

ions are collected on the oppositely charged electrode. During regeneration, the captured ions are repelled back into the channel, generating a concentrate stream. IEM helps to slow co-ions' migration, which refer to the ions with the same charge as the fixed charge on the IEM. This maintains the majority of co-ions inside the electrode during desalination, and slows co-ions' penetration from channel solution into the electrode during regeneration [11].

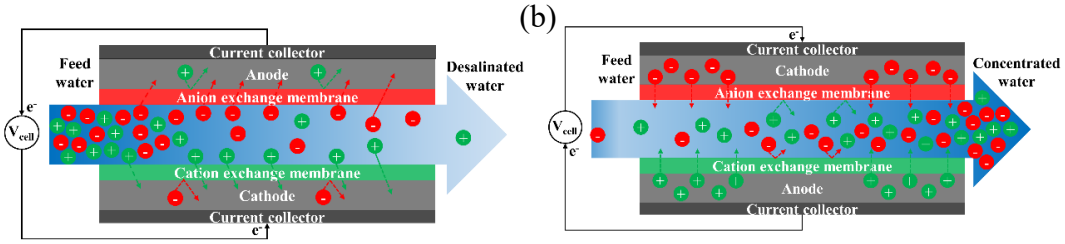

Figure 3.1. Schematic diagrams of MCDI, (a) desalination process, (b) regeneration process.

Lee et al. [12] first proposed MCDI and achieved a higher salt removal rate compared to CDI when desalinating power plant wastewater. The advantages of MCDI compared to conventional CDI in higher salt removal efficiency [13-16], higher current efficiency [14, 15, 17, 18], faster desalination rate [16] and lower energy consumption [18, 19] have also been reported. The feasibility of energy recovery in MCDI further decreases the net energy consumption [20, 21]. Properties of the electrode [22] and the IEM [23], feed water quality [10], and operating conditions [19, 24, 25], including operating mode, applied voltage/current, flow rate, water recovery and adsorption duration directly control cell performance, such as the amount of ions removed, the water quality of the desalinated stream, and energy efficiency of MCDI.

Building a comprehensive and accurate MCDI process model is essential to better understand the mechanisms and analyze the key influences on cell performance. An MCDI process model should capture ion transport and adsorption dynamics in the electrode, IEM and the channel. A model of porous electrode has been proposed treating electrode macropores as an ion transport pathway, and electrode micropores as adsorption sites [11, 26]. The small size of micropores suggests that the electric double layer (EDL) in these pores overlaps, creating a nearly uniform potential distribution throughout much of the micropores [26, 27]. Ion electrosorption behavior in micropores has been simulated via Gouy–Chapman–Stern (GCS) model [28, 29], classical Donnan theory [30], and modified Donnan theory [11, 26, 31-34]. Modified Donnan theory expands classical Donnan theory by introducing a Stern layer between micropore surface and diffuse layer and considering non-electrostatic attractions [35] from micropore surface towards the approaching ions [32]. The macroscopic porous electrode (MPE) model [36, 37] approximates microscopic pores as volume averaged adsorption sites. MPE theory avoids dealing with complicated morphology of the porous electrode and treats the sub-grid scale behavior of the micropores as an adsorptive sink term in macroscopic transport equations [31, 36, 38, 39]. Nernst-Planck (NP) equation has been applied to describe ion transport in both macropores [31, 34, 39] and IEM [10, 11, 34, 40]. In reality, co-ion transport through the IEM always occurs. When the concentration of the solution is getting closer to the fixed charge density of the IEM, Donnan exclusion becomes weakened, resulting in non-negligible co-ion transport through the IEM [41]. Non-ideal IEM theory has been proposed to include both counter-ion and co-ion

transport through the IEM [11, 25]. Donnan equilibrium has been widely used as the boundary condition on IEM [10, 11, 33, 34]. In a few studies, ion transport in the channel is modeled as a well-mixed bulk solution with a mass transfer boundary layer [10, 28, 39]. A porous media spacer is commonly used in the channel of (M)CDI to prevent short-circuiting, break concentration polarization and improve ions mixing [13, 42]. However, dispersion [43, 44] as a result of non-uniform flow in the porous spacer is rarely considered in existing models.

Although one-dimensional models possess the advantages of simplicity and easy implementation, they neglect ion transport in the direction of the flow in the channel. Several semi-two-dimensional models have been developed by dividing the channel into several well stirred units in the flow direction to simulate bi-dimensional ion transport in (M)CDI [10, 11, 25, 26, 34]. Hemmatifar et al. [31] proposed a two-dimensional CDI model by fully coupling axial and lateral ion transport and adsorption equations to capture the multi-dimensional effects on ion concentration and potential distributions inside the cell. The MPE model and modified Donnan theory were used to characterize the adsorption behavior, and NP equation was used to model ion transport in the cell [31].

In this study, a two-dimensional MCDI model is developed by modifying Hemmatifar's CDI model [31], which has facilitated the implementation of fully coupled two-dimensional models to explore cell performance characteristics in recent studies [45, 46]. The goals of this study include exploring the function of IEM on desalination rate and adsorption capability, and evaluating the impacts of hydraulic dispersion, IEM

properties and cell configuration on cell performance via a series of sensitivity analysis. The novelties of this model lie in: 1) This model is the first fully coupled two-dimensional process model for MCDI considering non-ideal IEM; 2) Hydraulic dispersion effects caused by fluid flowing through porous spacer are included; 3) Cycle time with maximal salt removal efficiency is proposed as an optimized operating mode. The implementation of this model contributes to a more convenient optimization of cell design and operating conditions of MCDI.

3.3. Model framework

3.3.1. MCDI parameters and operating conditions

This model simulates ion dynamics in a single-pass [6] CV mode MCDI. Figure 3.2 shows the two-dimensional MCDI assembly containing cathode, CEM, spacer-filled channel, AEM and anode successively. The first dimension (length dimension) is in the flow direction parallel to the electrodes and the second dimension (thickness dimension) is perpendicular to the electrodes (the desalination or regeneration flux dimension). The dimensions and other key device parameters employed in this model are shown in Table 3.1.

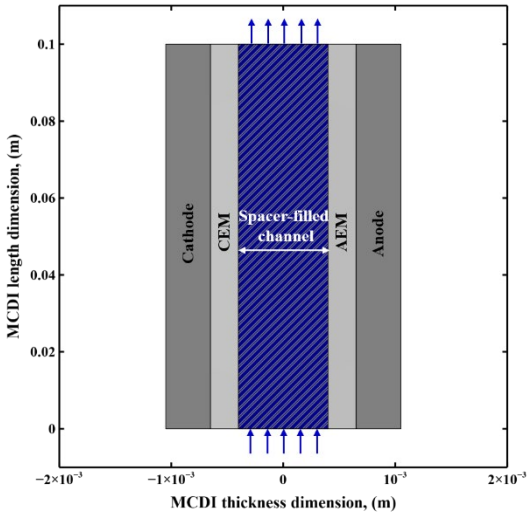

Figure 3.2. Two-dimensional MCDI assembly in this model.

Table 3.1. MCDI device parameters and operating conditions.

Parameter	Value	Unit
Cell length	8-12, 6 *	[cm]
Cathode/Anode thickness	0.2-0.6, 0.362 *	[mm]
Macropore porosity	0.4, 0.3 *	-
Micropore porosity	0.3, 0.3 *	-
Micropore capacitance	1.5, 1.2 *	[GF/m3]
Mass of a pair of electrodes	4.18, 1.35 *	[g]
CEM/AEM thickness	0.2-0.3, 0.17/0.14 *	[mm]
CEM/AEM water uptake volume fraction	0.2-0.6	[L(water) / L(swollen polymer)]
CEM/AEM fixed charge density	500-1000	[mol/m3]
Spacer-filled channel thickness	0.8-1.2, 0.25 *	[mm]
Spacer porosity	0.71	-
Hydraulic dispersivity	0.001-0.1	[m]
Ratio of transverse dispersivity over axial dispersivity	0.1	-
Diffusion coefficient of Na^+ in water	1.33 E-9	[m2/s]
Diffusion coefficient of Cl^- in water	2.03 E-9	[m2/s]
Feed water concentration	0-100, 20 *	[mol/m3]
Flow rate	10-20, 7.5 *	[mL/min]
Applied voltage	0.5-0.8, 1.2 *	[V]
Temperature	298.15	[K]

* Parameters from ref. [25] and are only used as inputs for model validation. Parameters before comma are used for subsequent simulation efforts.

A sodium chloride aqueous solution over the concentration range of 0-100 mol/m^3 is chosen to mimic brackish water. Electrode properties including macropore andmicropore void fractions, and capacitance are from Hemmatifar's paper [31]. Due to the incomplete data for a specific IEM, IEM properties including thickness, water uptake volume fraction and fixed charge density are set among a reasonable range of the reported commercial IEM values [47-49]. Water in IEM causes IEM swelling, and aids salt permeability through IEM [50, 51]. Here, water volume fraction represents the volume fraction of water content in the swollen IEM. Fixed charge density refers to the molar concentration of fixed charge groups per liter of absorbed water in a swollen IEM [52]. Fixed charge on IEM contributes to counter-ions' transport but suppresses co-ions' penetration through IEM [41]. Higher fixed charge density increases this permselectivity. The key membrane properties may vary between CEM and AEM in reality [53]. In this study, CEM and AEM are set to share the same geometry, water uptake volume fraction and fixed charge density for the sake of simplification and controlling variables. Non-woven cloth with a porosity of 0.71 and a mean pore size of 20 μm is chosen to simulate the spacer [54].

Hydraulic dispersion is mainly related to hydrodynamic characteristics and is unaffected by the electric field at these salinities [55]. Hydraulic dispersivity in porous media was indicated to be scale-dependent and approximated among micrometer to decimeter magnitude for centimeter-magnitude scales [56, 57]. Transverse dispersivity, the dispersivity perpendicular to the main flow, was varied over a range of 1-10% of the axial dispersivity as inputs in our model, which was consistent with the observation of

Bear and Verruijt [58] that transverse dispersivity was 1-20% of the axial dispersivity. Transverse dispersivity did not exert a significant influence on cell performance in the simulated results. The ratio of 1:10 (10%) was finally selected for subsequent simulation efforts.

To effectively avoid Faradaic reactions in (M)CDI, the applied voltage in constant voltage (CV) mode should not exceed 0.8 V [59, 60]. The applied voltage ranges from 0.5 V to 0.8 V in this study. The feed water concentration and flow rate are in a reasonable range of the reported (M)CDI operating conditions [5, 22, 61]. Detailed operating conditions are listed in Table 1. The parameters marked by asterisks are taken from ref. [25] and are only used as inputs for model validation.

3.3.2. Mathematical development

3.3.2.1. Assumptions

Ideal solution is assumed on the basis of the dilute feed water concentration range in this study. Complete dissociation of NaCl is assumed. The flow of water is incompressible and isothermal. Neither Faradaic reaction nor electrode electronic resistance is considered under the range of applied voltage [59, 60] and feed water concentration [34], respectively. The electrostatic effect of the charges of the IEM and the electrodes on diffusivity is assumed negligible [52, 62, 63]. Spacer-filled channel, IEM, and the distribution of electrode macropores and micropores are all assumed homogeneous. Electroneutrality is valid in spacer-filled channel and electrode

macropores, which is in accord with the principle that charge separation only occurs within the distance of Debye-Hückel length [64].

The pore Reynolds (Re) number is calculated by:

$$Re = \frac{d_p \rho u}{\mu}, \tag{3.1}$$

where, u is the interstitial velocity in the channel, d_p is the mean pore size of the porous spacer, ρ and μ are the density and viscosity of the solution, respectively. Darcy flow is valid in the channel [65].

3.3.2.2. Ion transport in spacer-filled channel

A modified NP equation incorporating hydraulic dispersion, electromigration and advection terms is used to describe the motion of charged species in the porous spacer-filled channel:

$$\varepsilon_s \frac{\partial c_i}{\partial t} = \nabla \cdot [D_{disp} \nabla c_i + \frac{z_i D_i F c_i}{RT} \nabla \varphi - U c_i], \tag{3.2}$$

where, ε_s is the porosity of the spacer, c_i is the concentration of species i in the channel, t is the operating time, z_i is the ion valence of species i, F is Faraday's constant (96485 C/mol), R is universal gas constant (8.314 J/mol/K), T is ambient temperature, φ is the electrolyte potential in the channel, U is the Darcy velocity, D_{disp} is the hydrodynamic dispersion coefficient expressed by dispersivity λ [57]:

$$\mathrm{D_{disp}} = \mathrm{D_i} + \lambda \frac{\mathrm{U}}{\varepsilon_s}. \tag{3.3}$$

where D_i is the effective diffusion coefficient of species i in the spacer-filled channel corrected by porosity and tortuosity [66]:

$$D_i = D_i^0 \frac{\varepsilon_s}{\tau} = D_i^0 \frac{\varepsilon_s}{\varepsilon_s^{\frac{-1}{3}}}, \tag{3.4}$$

where D_i^0 is the diffusion coefficient of species i in solution, and τ is the tortuosity in the spacer-filled channel. Hydraulic dispersion effects on electromigration are neglected. Considering electroneutrality in the channel, we arrive at:

$$\sum z_i c_i = 0. \tag{3.5}$$

3.3.2.3. Ion transport in the IEM

NP equation is also applicable for ion transport in the IEM:

$$\varepsilon_w \frac{\partial c_{m,i}}{\partial t} = \nabla \cdot (D_{m,i} \nabla c_{m,i} + \frac{z_i D_{m,i} F c_{m,i}}{RT} \nabla \varphi_m), \tag{3.6}$$

where, $c_{m,i}$ is the concentration of species i in the IEM, φ_m is the electrolyte potential in the IEM and $D_{m,i}$ is the effective diffusion coefficient of species i in the IEM amended by Mackie and Meares's model [67]:

$$D_{m,i} = D_i^0 [\varepsilon_w / (2 - \varepsilon_w)]^2, \tag{3.7}$$

here, ε_w is the water uptake volume fraction of the IEM. Fixed charges on the IEM are balanced by the ions in the solution:

$$\sum \mathrm{z_i c_{m,i}} + \mathrm{z_F c_F} = 0, \tag{3.8}$$

where z_F is the ion valence of the fixed charge on the IEM, and c_F is the fixed charge density on the IEM.

3.3.2.4. Ion transport and adsorption in the electrode

Ion transport in macropores is described by NP equation incorporating ion adsorption into micropores via a sink term on the left hand side:

$$\varepsilon_{ma}\frac{\partial c_{ma,i}}{\partial t}+\varepsilon_{mi}\frac{\partial c_{mi,i}}{\partial t}=\nabla\cdot\left(D_{ma,i}\nabla c_{ma,i}+\frac{z_i D_{ma,i} F c_{ma,i}}{RT}\nabla\varphi_{ma}\right), \tag{3.9}$$

here, $c_{ma,i}$ and $c_{mi,i}$ are the concentrations of species i in macropores and micropores, respectively, ε_{ma} and ε_{mi} are the porosities of macropores and micropores, respectively, φ_{ma} is the electrolyte potential in macropores, and $D_{ma,i}$ is the effective diffusion coefficient of species i in macropores corrected by porosity and tortuosity [66]:

$$D_{ma,i}=D_i^0\left(\varepsilon_{ma}/\varepsilon_{ma}^{-1/3}\right). \tag{3.10}$$

Electroneutrality is also valid in macropores:

$$\sum z_i c_{ma,i}=0. \tag{3.11}$$

Modified Donnan theory without non-electrostatic term is applied to account for ion adsorption in micropores:

$$\varphi_{st}=-\frac{F}{C_{st}}\left(\sum z_i c_{mi,i}\right), \tag{3.12}$$

$$c_{mi,i}=c_{ma,i}\exp\left(-\frac{z_i F\varphi_d}{RT}\right), \tag{3.13}$$

here, φ_{st} is Stern layer potential drop, C_{st} is micropore volumetric capacitance, and φ_d is Donnan potential representing potential difference between micropore's diffuse layer and its adjacent macropore.

Equation (3.14) indicates that the applied electric potential on the electrode equals to the sum of Stern layer potential drop, Donnan potential and macropore electrolyte potential:

$$\pm\frac{V_{cell}}{2} = \varphi_{st} + \varphi_d + \varphi_{ma}, \tag{3.14}$$

where V_{cell} is the applied voltage. Assuming MCDI is symmetric with a zero electrolyte potential along the symmetry axis, the potential is set as half negative applied voltage and half positive applied voltage for cathode and anode, respectively.

3.3.2.5. Boundary conditions

Donnan equilibrium serves as the boundary conditions of both IEM-channel boundary (3.15) and IEM-electrode boundary (3.16):

$$\varphi_{m,c}\text{-}\varphi = \frac{RT}{z_i F}\ln\frac{c_i}{c_{m,i}}, \tag{3.15}$$

$$\varphi_{m,e}\text{-}\varphi_{ma} = \frac{RT}{z_i F}\ln\frac{c_{ma,i}}{c_{m,i}}, \tag{3.16}$$

here, $\varphi_{m,c}$ and $\varphi_{m,e}$ are the electrolyte potentials in IEM on the IEM-channel boundary and IEM-electrode boundary, respectively.

Ion flux and current density are continuous on the IEM's boundaries. No ion flux is out of the cell. The inlet of the influent solution obeys Danckwerts flux boundary condition. The derivatives of all variables are set to zero at the outlet.

3.4. Results

The set of non-linear partial differential equations (PDE) are solved by COMSOL Multiphysics 5.4 software through building a fine mesh near the boundaries of the IEM to help convergence and simulation accuracy. The final mesh consists of 364212 degrees of freedom with 35000 domain elements and 1300 boundary elements, which balances accuracy and simulation time. Preliminary evaluation showed that this discretization provided mesh independent results.

3.4.1. Model validation

A semi-quantitative model validation is conducted by comparing the trends of simulated effluent concentration curves under varying applied voltage and varying flow rate with published experimental observations [10, 68]. The general behavior observed experimentally is qualitatively reproduced by this model with a rapid decrease to a minimum effluent concentration and then a slow return to influent concentration as the electrode becomes saturated. Increasing applied voltage achieves greater sorption and results in a lower minimum effluent concentration, as observed by Lee and Choi [68]. Decreasing flow rate reduces the minimum effluent concentration with a prolonged time to approach equilibrium, also known as adsorption saturation. With the same equilibrium adsorption amount, time to reach equilibrium is inversely proportional to

desalination rate, which is an important indicator of (M)CDI performance [26]. Similar trends from varying flow rate are observed by Biesheuvel and Van der Wal [10].

A quantitative model validation is then carried out by setting up MCDI device parameters and operating conditions based on those in ref. [25] (see Table 3.1), and adjusting effective micropore volume and hydraulic dispersivity, two parameters that were not measured, to fit the observed performance. Figure 3.3 shows that by adjusting effective micropore volume to 55% of the total micropore volume, and dispersivity to 0.172 m, the simulated salt adsorption per cycle curve agrees with experimental observations [25].

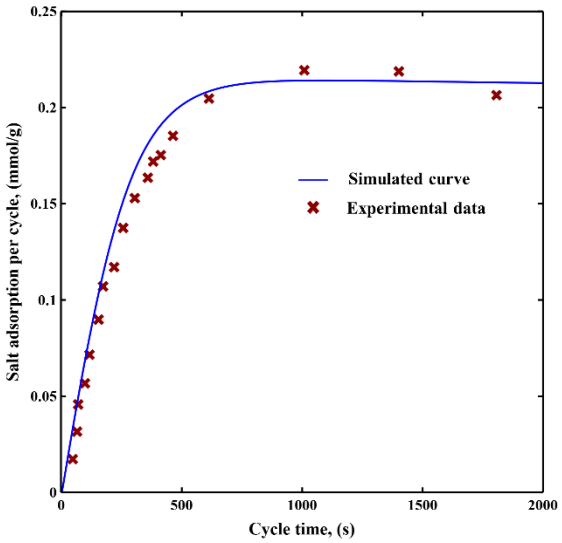

Figure 3.3. Simulated salt adsorption per cycle curve with this model and experimental data from ref. [25].

This validated model is subsequently utilized to explore the function of IEM in MCDI and conduct sensitivity analysis to evaluate influencing factors of MCDI performance.

3.4.2. Function of IEM in MCDI

3.4.2.1. Desalination rate

Figure 3.4 compares transient effluent concentration curves of CDI and MCDI at applied voltage of 0.8 V, flow rate of 10 mL/min and feed water concentration of 20 mol/m^3. The time to reach equilibrium in MCDI is roughly half as much as that in CDI, indicating counter-ion transport is enhanced with the aid of IEM. The improved desalination rate in MCDI is consistent with experimental observations [11, 16, 18, 69, 70].

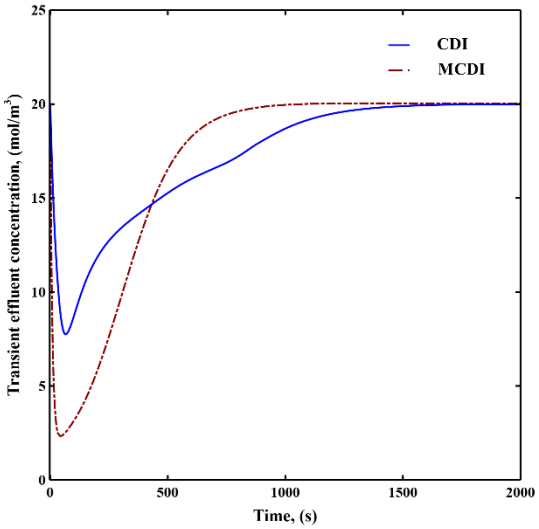

Figure 3.4. Transient effluent concentration curves of CDI and MCDI. The applied voltage is 0.8 V, the flow rate is 10 mL/min, and the feed water concentration is 20 mol/m^3.

The ion flux distributions of sodium ions and chloride ions along a cross-sectional line of CDI and MCDI at t = 50 s under the same operating conditions of flow rate of 10 mL/min, applied voltage of 0.8 V and feed water concentration of 20 mol/m^3 are

displayed in Figure 3.5 (a) and (b), respectively. The time of 50 s is chosen because it is near the minimum effluent concentration and the maximum in changes in concentration profile across both cells, making sure the absolute values of ion fluxes are large enough to show a clear deviation between CDI and MCDI.

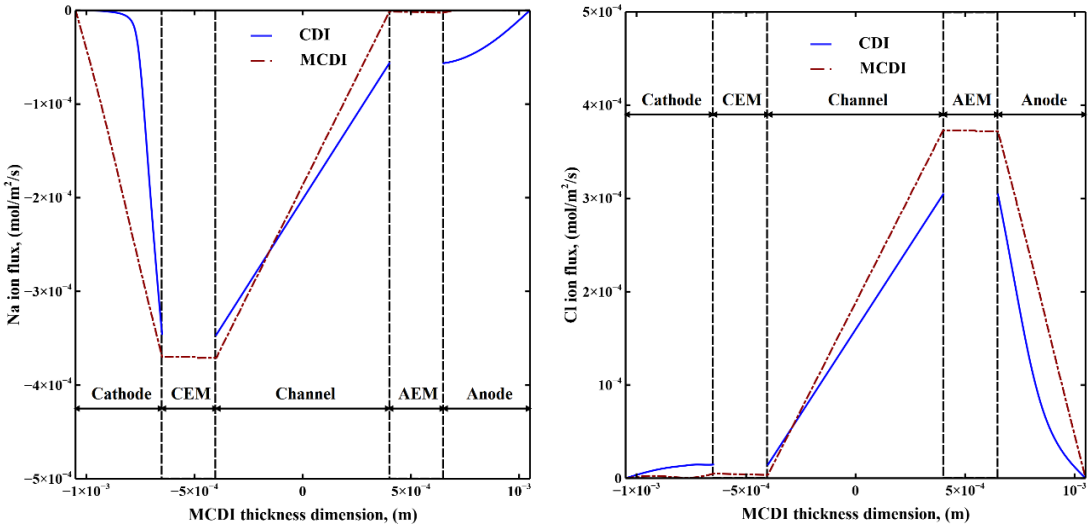

(a) (b)

Figure 3.5. (a) Sodium ion flux distribution and (b) chloride ion flux distribution along the cross-sectional line of CDI and MCDI at t = 50 s. The applied voltage is 0.8 V, the flow rate is 10 mL/min, and the feed water concentration is 20 mol/m^3.

Negative values imply ion transport towards the cathode (and positive values towards the anode). A fixed charge on the IEM enhances counter-ions' flux in the vicinity of the IEM and inhibits co-ions' flux out of the electrode. The enhanced counter-ion flux into macropores helps facilitate counter-ions' adsorption into the adjacent micropores, resulting in a shortened equilibrium time and thus an improved rate of desalination in MCDI compared to CDI.

3.4.2.2. Adsorption Capacity

Adsorption isotherms in CDI and MCDI are plotted as a function of equilibrium bulk concentration under the same operating conditions of flow rate of 10 mL/min, and applied voltage of 0.8 V in Figure 6. This adsorption amount refers to the total adsorbed salt (NaCl) per unit mass of both cathode and anode. Equilibrium bulk concentration is identical to the feed water concentration in single-pass mode. Both cells achieve a peak adsorption before an equilibrium bulk concentration of 1500 ppm with MCDI exhibiting a higher capacity than CDI. Since the co-ion repulsion effects [71] become significant at higher concentrations in CDI, the adsorption capability of CDI is affected, showing a decrease in unit adsorption amount at high equilibrium concentration range. With the aid of IEM, MCDI does not exhibit in significant reductions in adsorption capacity at higher concentrations. This enhanced adsorption in MCDI compared to CDI was also captured by the experimentally observed shapes [11, 72].

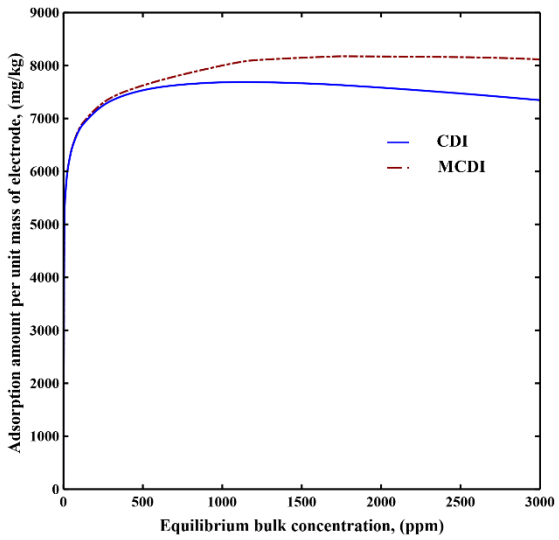

Figure 3.6. Adsorption isotherms of CDI and MCDI. The flow rate is 10 mL/min, and the applied voltage is 0.8 V.

In order to better understand the equilibrium adsorption, the equilibrium molar adsorption of sodium chloride in electrode micropores, electrode macropores and IEM were estimated separately using this model, and the corresponding equilibrium adsorption percentage is shown in Table 3.2.

Table 3.2. Equilibrium adsorption percentage in micropores, macropores and IEM under varying operating conditions.

Operating conditions		Micropores, (%)	Macropores, (%)	IEM, (%)
Variant applied voltage at flow rate of 10 mL/min and feed water concentration of 20 mol/m^3.	0.5 V	91.34	8.53	0.13
	0.6 V	93.19	6.71	0.10
	0.7 V	94.42	5.50	0.08
	0.8 V	95.35	4.58	0.07
Variant feed water concentration at applied voltage of 0.8 V and flow rate of 10 mL/min.	20 mol/m^3	95.35	4.58	0.07
	30 mol/m^3	93.96	5.91	0.13
	50 mol/m^3	91.90	7.82	0.28
	80 mol/m^3	90.46	9.05	0.49
Variant flow rate at applied voltage of 0.8 V and feed water concentration of 20 mol/m^3.	5 ml/min	95.29	4.64	0.07
	10 ml/min	95.35	4.58	0.07
	15 ml/min	95.41	4.52	0.07
	20 ml/min	95.48	4.45	0.07

The micropores are responsible for the vast majority of the sorption suggesting that the primary function of the IEM is to enhance the rate of adsorption rather than the ultimate capacity. The IEM, however, also aids in retention of ions in the macropores and that represents the bulk of the difference with CDI shown in Figure 3.6. Increasing applied voltage enhances the adsorption ability of micropores, reducing the adsorption proportion of IEM and macropores. Increasing concentration reduces the adsorption capacity of micropores and augments the ion accumulation in macropores and IEM, which increases the adsorption proportion of macropores and IEM. Changing flow rate doesn't affect the adsorption capacity of MCDI, so almost no changes in adsorption percentage.

3.4.2.3. Cycle time

(M)CDI is usually operated till equilibrium during desalination in CV mode [5, 61], which is not the most efficient operation considering the less functional duration close to equilibrium (see Figure 3.4). Here, we propose an operating approach based upon

maximizing salt removal efficiency to control the cycle time, which is the time before equilibrium to switch to regeneration of the electrode.

The transient average effluent concentration and salt removal efficiency are shown in (3.17) and (3.18), respectively:

$$c_{out,ave} = \frac{\int c_{out} dt}{t}, \tag{3.17}$$

$$\eta_s = \left(1 - \frac{c_{out,ave}}{c_0}\right) \times 100\%, \tag{3.18}$$

where, $c_{out,ave}$ is transient average effluent concentration, c_{out} is transient effluent concentration, t is operating time during desalination step, η_s is transient salt removal efficiency, and c_0 is feed water concentration.

Figure 3.7 displays transient effluent concentration, transient average effluent concentration, and transient salt removal efficiency curves of MCDI under the operating conditions of applied voltage of 0.8 V, flow rate of 10 mL/min and feed water concentration of 20 mol/m^3. The cycle time based upon maximizing salt removal efficiency is shown with an "x". The corresponding salt removal efficiency of MCDI achieves several-fold improvement compared to operating till equilibrium.

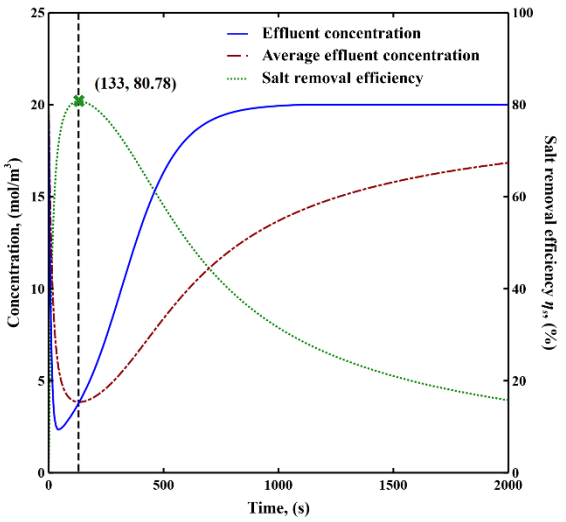

Figure 3.7. Transient effluent concentration, transient average effluent concentration, and transient salt removal efficiency curves of MCDI. The cross mark represents cycle time with the maximum salt removal efficiency. The applied voltage is 0.8 V, the flow rate is 10 mL/min, and the feed water concentration is 20 mol/m^3.

The maximum salt removal efficiency and the corresponding cycle time of CDI and MCDI under varying operating conditions are shown in Figure 3.8. The operating conditions in Figure 3.8 (a) are at flow rate of 10 mL/min, feed water concentration of 20 mol/m^3, and applied voltage of 0.5 V, 0.6 V, 0.7 V and 0.8 V, Figure 3.8 (b) are at applied voltage of 0.8 V, flow rate of 10 mL/min, and feed water concentration of 20 mol/m^3, 50 mol/m^3, and 80 mol/m^3, and Figure 3.8 (c) are at feed water concentration of 20 mol/m^3, applied voltage of 0.8 V, and flow rate of 10 mL/min, 15 mL/min, and 20 mL/min.

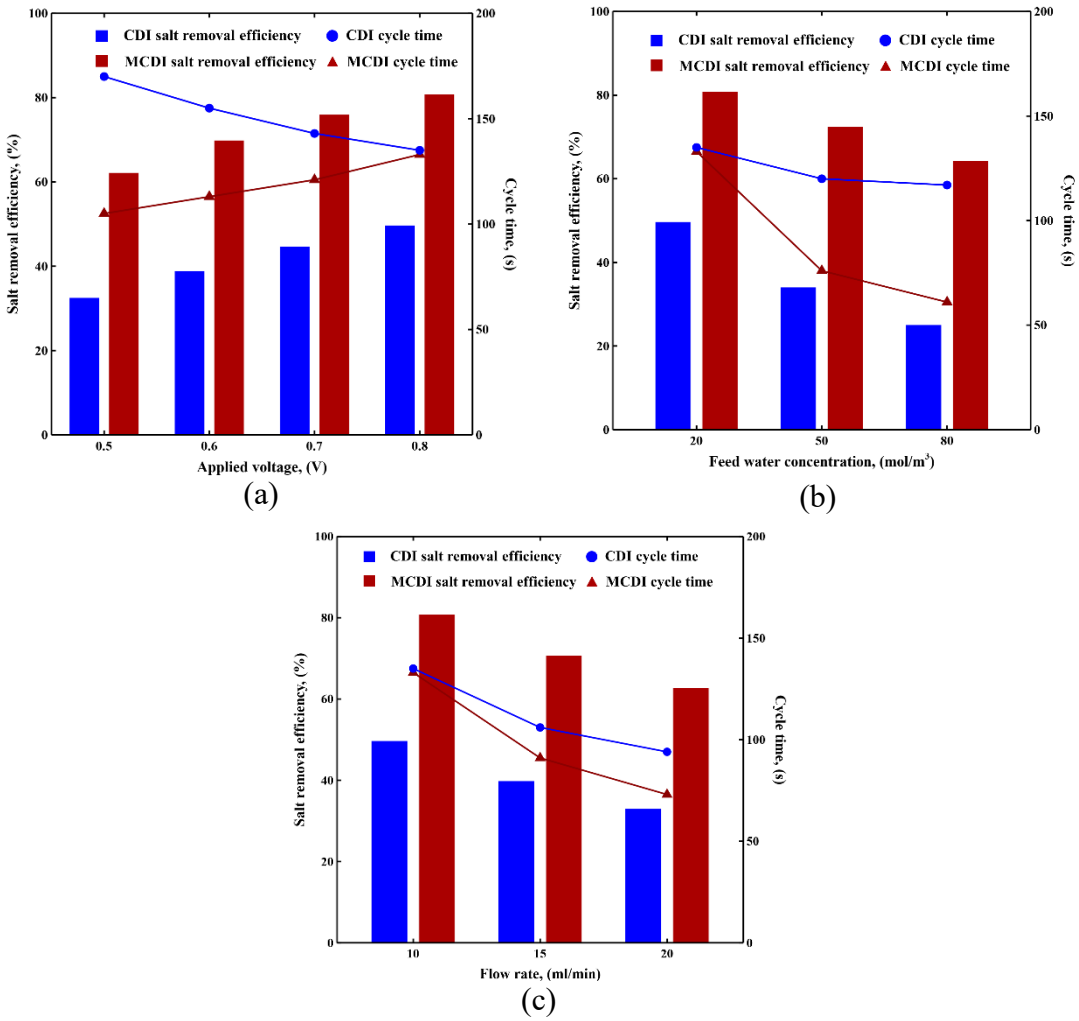

Figure 3.8. The maximum salt removal efficiency and the corresponding cycle time of CDI and MCDI under (a) flow rate of 10 mL/min and feed water concentration of 20 mol/m3, (b) applied voltage of 0.8 V and flow rate of 10 mL/min, and (c) feed water concentration of 20 mol/m^3 and applied voltage of 0.8 V. Lines are used for guiding the eyes.

Overall, MCDI possesses a shorter cycle time with a greater salt removal efficiency compared to CDI, which is the result of the rapid achievement of a lower minimum effluent salt concentration during MCDI desalination (see Figure 3.4). Increasing applied voltage increases salt removal efficiency for both CDI and MCDI by increasing

the salt removal capacity of electrode micropores. Electromigration indicates the motion of the diffusing ionic species relative to the electrolyte induced by electrostatic forces. Increasing feed water concentration increases electromigration and indirectly improves diffusive and dispersive ion fluxes, resulting in a faster desalination rate and rapid achievement of the maximum salt removal efficiency. The decreased salt removal efficiency with increasing equilibrium concentration is related to the adsorption capacity of the electrode. Decreasing flow rate extends the residence time of the solution in the channel, allowing more ions to be transported and adsorbed per volume of treated water, which leads to an improved salt removal efficiency. The reduced velocity, however, reduces convective and dispersive ion fluxes and lengthens the time to maximum salt removal efficiency. Similar trends of salt removal efficiency under varying applied voltage, flow rate and feed water concentration were captured in experimental observations [10, 68].

3.4.3. Sensitivity analysis

Sensitivity analysis was conducted aiming at investigating hydraulic dispersivity, key IEM properties and cell configuration on MCDI performance.

Table 3.3 shows the maximum salt removal efficiency and the corresponding cycle time of MCDI at an applied voltage of 0.8 V, flow rate of 10 mL/min, and feed water concentration of 20 mol/m^3 and how it changes with varying dispersivity. Hydraulic dispersion varies with transport distance, saturation degree of flow conditions, and the interactive effects of lateral scale, flow rate and porous media texture [73]. Larger

dispersivity results in improvement of hydraulic dispersion in flow direction compared to the lateral direction, resulting in a faster longitudinal ion mixing and a shorter residence time of the ions. Hence, the corresponding salt removal efficiency is lowered. Dispersion does not affect the equilibrium adsorption amount of MCDI, but a higher dispersivity requires a longer time to reach equilibrium. This results in an unchanged time to minimum effluent concentration under varying dispersivity and thus an unchanged cycle time.

Table 3.3. Effects of dispersivity on the maximum salt removal efficiency and the corresponding cycle time of MCDI.

Dispersivity, (m)	**Salt removal efficiency, (%)**	**Cycle time, (s)**
0.001	86.15	136
0.01	83.31	133
0.1	73.91	134

Not many studies have analyzed IEM properties' effects on MCDI performance. Tian et al. [74] revealed moderate cross-linking of IEM benefited MCDI adsorption since highly cross-linked IEM possessed low hydrophilicity, inhibiting the penetration of hydrated counter-ions. Chang et al. [75] pointed out that high ion charge capacity, which was defined as molar concentration of fixed charge groups per gram of dry polymer, low resistance, and moderate water content contributed to good cell performance, since too much water in IEM would increase ionic transfer resistance. We can evaluate the effects of IEM properties in this model. Table 3.4 shows the maximum salt removal efficiency and the corresponding cycle time of MCDI at an applied voltage of 0.8 V, flow rate of 10 mL/min, and feed water concentration of 20 mol/m^3 and how it changes with IEM water uptake volume fraction, IEM thickness and IEM fixed charge density.

Varying IEM thicknesses exerts minimal impacts on cycle time and magnitude of maximum salt removal efficiency. This suggests that thin IEM-electrode composites with lower resistance may be favorable alternatives to commercial IEM [76]. Increasing IEM fixed charge density increases ion storage in electrode macropores and thus achieves an improved salt removal efficiency. Overall, IEM properties exhibit marginal effects on MCDI performance within the parameter ranges in this study.

Table 3.4. Effects of IEM water uptake volume fraction, IEM thickness and IEM fixed charge density on the maximum salt removal efficiency and the corresponding cycle time of MCDI.

IEM properties		**Salt removal efficiency, (%)**	**Cycle time, (s)**
IEM water uptake volume fraction	0.2	79.30	136
	0.4	80.78	133
	0.6	80.90	132
IEM thickness, (mm)	0.2	80.89	132
	0.25	80.78	133
	0.3	80.64	133
IEM fixed charge density, (mol/m^3)	500	79.21	127
	750	80.70	128
	1000	80.78	133

Table 3.5 shows the maximum salt removal efficiency and the corresponding cycle time of MCDI at applied voltage of 0.8 V, flow rate of 10 mL/min, and feed water concentration of 20 mol/m^3 with varying cell length, electrode thickness and channel thickness. Increasing cell length and electrode thickness enhances salt adsorption ability by increasing the total mass of the sorptive electrode, and extends the active area, extending the maximum salt removal efficiency. Increasing the channel thickness prolongs the ion transport path toward the electrodes and increases the residence time of the solution in the channel, which result in a longer time to a reduced maximum salt

removal efficiency. Porada et al. [77] achieved similar trends of salt removal efficiency when increasing electrode and channel thicknesses in CDI.

Table 3.5. Effects of cell length, electrode thickness and channel thickness on the maximum salt removal efficiency and the corresponding cycle time of MCDI.

Cell configuration		Salt removal efficiency, (%)	Cycle time, (s)
Cell length, (cm)	8	75.51	106
	10	80.78	133
	12	83.55	165
Electrode thickness, (mm)	0.2	76.70	87
	0.4	80.78	133
	0.6	82.59	154
Channel thickness, (mm)	0.8	80.78	133
	1.0	74.51	151
	1.2	68.90	168

3.4. Discussion

A fully coupled two-dimensional MCDI process model was developed, validated, and applied for exploring the role of IEM and evaluating influencing factors of cell performance. The main results are as follows: 1) A near doubling in desalination rate in MCDI compared to CDI was achieved due to the enhanced counter-ions' flux in the vicinity of IEM; 2) Electrode macropores exhibited 4-9% of total ion storage ability because of reduced co-ions' flux through the IEM; 3) An optimized cycle time was proposed to achieve several-fold improvement of salt removal efficiency compared to operating cell till equilibrium. The use of an IEM, application of high voltage and reduced flow rate increased maximal salt removal efficiency; 4) Sensitivity analysis indicated that increasing cell length and electrode thickness improved salt removal efficiency, while increasing dispersivity and channel thickness lowered salt removal

efficiency, and no significant effects were discovered by tuning IEM properties within the parameter range of this study. This model can be applied to help optimize cell design and operating conditions based on desalination objectives.

Temperature effects, energetic properties and systemic resistances have been analyzed in other studies. Huang and Tang [78] revealed that high temperature fastened desalination rate but affected adsorption capacity of CDI. Energy consumption of MCDI is determined by water recovery and salt removal efficiency, and can be improved with energy recovery [79]. Energy losses in MCDI largely depend on systematic resistances, including external circuit electronic resistance, electrode electronic resistance and ionic transfer resistance [34]. Ionic transfer resistance is positively correlated to transport distance, and is negatively correlated to ionic concentration and porosity of transfer media [34]. Ionic transfer resistance is captured by the NP equations in this model. Palakkal et al. [80] discovered that thin IEM with high ion conductivity possessed low resistance and reduced energy consumption. This model can be extended by modifying the transport and adsorption terms to incorporate the effects of temperature, electronic resistances, Faradaic reactions and special affinity towards specific ions with surface modified electrode and IEM.

3.5. References

[1] M. M. Mekonnen and A. Y. Hoekstra, "Four billion people facing severe water scarcity," *Science advances,* vol. 2, no. 2, p. e1500323, 2016.

[2] S. Honarparvar, X. Zhang, T. Chen, C. Na, and D. Reible, "Modeling technologies for desalination of brackish water—toward a sustainable water supply," *Current Opinion in Chemical Engineering,* vol. 26, pp. 104-111, 2019.

[3] N. Ghaffour, T. M. Missimer, and G. L. Amy, "Technical review and evaluation of the economics of water desalination: current and future challenges for better water supply sustainability," *Desalination,* vol. 309, pp. 197-207, 2013.

[4] M. Elimelech and W. A. Phillip, "The future of seawater desalination: energy, technology, and the environment," *science,* vol. 333, no. 6043, pp. 712-717, 2011.

[5] M. Suss, S. Porada, X. Sun, P. Biesheuvel, J. Yoon, and V. Presser, "Water desalination via capacitive deionization: what is it and what can we expect from it?," *Energy & Environmental Science,* vol. 8, no. 8, pp. 2296-2319, 2015.

[6] S. Porada, R. Zhao, A. Van Der Wal, V. Presser, and P. Biesheuvel, "Review on the science and technology of water desalination by capacitive deionization," *Progress in Materials Science,* vol. 58, no. 8, pp. 1388-1442, 2013.

[7] F. A. AlMarzooqi, A. A. Al Ghaferi, I. Saadat, and N. Hilal, "Application of capacitive deionisation in water desalination: a review," *Desalination,* vol. 342, pp. 3-15, 2014.

[8] J. Ma, J. Ma, C. Zhang, J. Song, W. Dong, and T. D. Waite, "Flow-electrode capacitive deionization (FCDI) scale-up using a membrane stack configuration," *Water Res.,* vol. 168, p. 115186, 2020.

[9] S. Yang, S.-i. Jeon, H. Kim, J. Choi, J.-g. Yeo, H.-r. Park, and D. K. Kim, "Stack design and operation for scaling up the capacity of flow-electrode capacitive deionization technology," *ACS Sustainable Chemistry & Engineering,* vol. 4, no. 8, pp. 4174-4180, 2016.

[10] P. Biesheuvel and A. Van der Wal, "Membrane capacitive deionization," *Journal of Membrane Science,* vol. 346, no. 2, pp. 256-262, 2010.

[11] P. Biesheuvel, R. Zhao, S. Porada, and A. Van der Wal, "Theory of membrane capacitive deionization including the effect of the electrode pore space," *Journal of colloid and interface science,* vol. 360, no. 1, pp. 239-248, 2011.

[12] J.-B. Lee, K.-K. Park, H.-M. Eum, and C.-W. Lee, "Desalination of a thermal power plant wastewater by membrane capacitive deionization," *Desalination,* vol. 196, no. 1-3, pp. 125-134, 2006.

[13] H. Li, Y. Gao, L. Pan, Y. Zhang, Y. Chen, and Z. Sun, "Electrosorptive desalination by carbon nanotubes and nanofibres electrodes and ion-exchange membranes," *Water Res.,* vol. 42, no. 20, pp. 4923-4928, 2008.

[14] Y.-J. Kim and J.-H. Choi, "Enhanced desalination efficiency in capacitive deionization with an ion-selective membrane," *Separation and Purification Technology,* vol. 71, no. 1, pp. 70-75, 2010.

[15] Y.-J. Kim and J.-H. Choi, "Improvement of desalination efficiency in capacitive deionization using a carbon electrode coated with an ion-exchange polymer," *Water Res.,* vol. 44, no. 3, pp. 990-996, 2010.

[16] H. Li and L. Zou, "Ion-exchange membrane capacitive deionization: A new strategy for brackish water desalination," *Desalination,* vol. 275, no. 1-3, pp. 62-66, 2011.

[17] Y.-J. Kim, J. Hur, W. Bae, and J.-H. Choi, "Desalination of brackish water containing oil compound by capacitive deionization process," *Desalination,* vol. 253, no. 1-3, pp. 119-123, 2010.

[18] Y. Zhao, Y. Wang, R. Wang, Y. Wu, S. Xu, and J. Wang, "Performance comparison and energy consumption analysis of capacitive deionization and membrane capacitive deionization processes," *Desalination,* vol. 324, pp. 127-133, 2013.

[19] R. Zhao, P. Biesheuvel, and A. Van der Wal, "Energy consumption and constant current operation in membrane capacitive deionization," *Energy & Environmental Science,* vol. 5, no. 11, pp. 9520-9527, 2012.

[20] J. Kang, T. Kim, H. Shin, J. Lee, J.-I. Ha, and J. Yoon, "Direct energy recovery system for membrane capacitive deionization," *Desalination,* vol. 398, pp. 144-150, 2016.

[21] P. Długołęcki and A. van der Wal, "Energy recovery in membrane capacitive deionization," *Environmental science & technology,* vol. 47, no. 9, pp. 4904-4910, 2013.

[22] J. Landon, X. Gao, A. Omosebi, and K. Liu, "Progress and outlook for capacitive deionization technology," *Current Opinion in Chemical Engineering,* vol. 25, pp. 1-8, 2019.

[23] A. Hassanvand, K. Wei, S. Talebi, G. Chen, and S. Kentish, "The role of ion exchange membranes in membrane capacitive deionisation," *Membranes,* vol. 7, no. 3, p. 54, 2017.

[24] R. Zhao, S. Porada, P. Biesheuvel, and A. Van der Wal, "Energy consumption in membrane capacitive deionization for different water recoveries and flow rates, and comparison with reverse osmosis," *Desalination,* vol. 330, pp. 35-41, 2013.

[25] R. Zhao, O. Satpradit, H. Rijnaarts, P. Biesheuvel, and A. Van der Wal, "Optimization of salt adsorption rate in membrane capacitive deionization," *Water Res.,* vol. 47, no. 5, pp. 1941-1952, 2013.

[26] S. Porada, L. Borchardt, M. Oschatz, M. Bryjak, J. Atchison, K. Keesman, S. Kaskel, P. Biesheuvel, and V. Presser, "Direct prediction of the desalination performance of porous carbon electrodes for capacitive deionization," *Energy & Environmental Science,* vol. 6, no. 12, pp. 3700-3712, 2013.

[27] W. Qu and D. Li, "A model for overlapped EDL fields," *Journal of colloid and interface science,* vol. 224, no. 2, pp. 397-407, 2000.

[28] P. Biesheuvel, B. Van Limpt, and A. Van der Wal, "Dynamic adsorption/desorption process model for capacitive deionization," *The journal of physical chemistry C,* vol. 113, no. 14, pp. 5636-5640, 2009.

[29] F. G. Donnan, "The theory of membrane equilibria," *Chemical reviews,* vol. 1, no. 1, pp. 73-90, 1924.

[30] M. Müllier and B. Kastening, "The double layer of activated carbon electrodes: Part 1. The contribution of ions in the pores," *Journal of Electroanalytical Chemistry,* vol. 374, no. 1-2, pp. 149-158, 1994.

[31] A. Hemmatifar, M. Stadermann, and J. G. Santiago, "Two-dimensional porous electrode model for capacitive deionization," *The Journal of Physical Chemistry C,* vol. 119, no. 44, pp. 24681-24694, 2015.

[32] P. Biesheuvel, Y. Fu, and M. Bazant, "Electrochemistry and capacitive charging of porous electrodes in asymmetric multicomponent electrolytes," *Russian Journal of Electrochemistry,* vol. 48, no. 6, pp. 580-592, 2012.

[33] A. Rommerskirchen, B. Ohs, K. A. Hepp, R. Femmer, and M. Wessling, "Modeling continuous flow-electrode capacitive deionization processes with ion-exchange membranes," *Journal of membrane science,* vol. 546, pp. 188-196, 2018.

[34] J. Dykstra, R. Zhao, P. Biesheuvel, and A. Van der Wal, "Resistance identification and rational process design in capacitive deionization," *Water Res.,* vol. 88, pp. 358-370, 2016.

[35] B. Kastening and M. Heins, "Properties of electrolytes in the micropores of activated carbon," *Electrochimica Acta,* vol. 50, no. 12, pp. 2487-2498, 2005.

[36] J. Newman and E. Thomas-Alyea, "K. Electrochemical Systems," ed: John Wiley & Sons: New York, 2004.

[37] A. Johnson and J. Newman, "Desalting by means of porous carbon electrodes," *Journal of the Electrochemical Society,* vol. 118, no. 3, pp. 510-517, 1971.

[38] A. N. Shocron and M. E. Suss, "The effect of surface transport on water desalination by porous electrodes undergoing capacitive charging," *Journal of Physics: Condensed Matter,* vol. 29, no. 8, p. 084003, 2017.

[39] P. Biesheuvel and M. Bazant, "Nonlinear dynamics of capacitive charging and desalination by porous electrodes," *Physical review E,* vol. 81, no. 3, p. 031502, 2010.

[40] V. Volgin and A. Davydov, "Ionic transport through ion-exchange and bipolar membranes," *Journal of membrane science,* vol. 259, no. 1, pp. 110-121, 2005.

[41] T. Luo, S. Abdu, and M. Wessling, "Selectivity of ion exchange membranes: A review," *Journal of membrane science,* vol. 555, pp. 429-454, 2018.

[42] A. Hassanvand, "Membrane capacitive deionisation as a novel approach to wastewater treatment," PhD PhD thesis, School of Chemical and Biomedical Engineering, The University of Melbourne, Melbourne, Australia, 2018.

[43] A. E. Scheidegger, "General theory of dispersion in porous media," *Journal of Geophysical Research,* vol. 66, no. 10, pp. 3273-3278, 1961.

[44] A. E. Scheidegger, "Statistical hydrodynamics in porous media," *Journal of Applied Physics,* vol. 25, no. 8, pp. 994-1001, 1954.

[45] Y. Salamat and C. H. Hidrovo, "A parametric study of multiscale transport phenomena and performance characteristics of capacitive deionization systems," *Desalination,* vol. 438, pp. 24-36, 2018.

[46] Y. Salamat and C. H. Hidrovo, "Significance of the micropores electro-sorption resistance in capacitive deionization systems," *Water Res.,* vol. 169, p. 115286, 2020.

[47] J. Kamcev, D. R. Paul, G. S. Manning, and B. D. Freeman, "Ion diffusion coefficients in ion exchange membranes: significance of counterion condensation," *Macromolecules,* vol. 51, no. 15, pp. 5519-5529, 2018.

[48] J. Ran, L. Wu, Y. He, Z. Yang, Y. Wang, C. Jiang, L. Ge, E. Bakangura, and T. Xu, "Ion exchange membranes: New developments and applications," *Journal of Membrane Science,* vol. 522, pp. 267-291, 2017.

[49] Q. Duan, S. Ge, and C.-Y. Wang, "Water uptake, ionic conductivity and swelling properties of anion-exchange membrane," *Journal of Power Sources,* vol. 243, pp. 773-778, 2013.

[50] H. Strathmann, *Ion-exchange membrane separation processes*. Elsevier, 2004.

[51] R. S. Kingsbury, K. Bruning, S. Zhu, S. Flotron, C. Miller, and O. Coronell, "Influence of water uptake, charge, Manning parameter, and contact angle on water and salt transport in commercial ion exchange membranes," *Industrial & Engineering Chemistry Research,* vol. 58, no. 40, pp. 18663-18674, 2019.

[52] J. Kamcev, D. R. Paul, G. S. Manning, and B. D. Freeman, "Predicting salt permeability coefficients in highly swollen, highly charged ion exchange membranes," *ACS applied materials & interfaces,* vol. 9, no. 4, pp. 4044-4056, 2017.

[53] T. Xu, "Ion exchange membranes: state of their development and perspective," *Journal of membrane science,* vol. 263, no. 1-2, pp. 1-29, 2005.

[54] A. Rawal, "Structural analysis of pore size distribution of nonwovens," *The Journal of The Textile Institute,* vol. 101, no. 4, pp. 350-359, 2010.

[55] J. Bear and Y. Bachmat, "A generalized theory on hydrodynamic dispersion in porous media," in *IASH symposium on artificial recharge and management of aquifers*, 1967, vol. 72: IASH Publ. Int. Union Geod. Geophys, Haifa, Israel, pp. 7-16.

[56] L. W. Gelhar, C. Welty, and K. R. Rehfeldt, "A critical review of data on field‐scale dispersion in aquifers," *Water resources research,* vol. 28, no. 7, pp. 1955-1974, 1992.

[57] J. Vanderborght, H. Vereecken, and I. Agrosphere IV, "Review of dispersivity lengths for transport modeling in soils," ed: Retrieved, 2018.

[58] J. Bear and A. Verruijt, *Modeling groundwater flow and pollution*. Springer Science & Business Media, 2012.

[59] D. Lu, W. Cai, and Y. Wang, "Optimization of the voltage window for long-term capacitive deionization stability," *Desalination,* vol. 424, pp. 53-61, 2017.

[60] J.-H. Choi, "Comparison of constant voltage (CV) and constant current (CC) operation in the membrane capacitive deionisation process," *Desalination and Water Treatment,* vol. 56, no. 4, pp. 921-928, 2015.

[61] M. A. Ahmed and S. Tewari, "Capacitive deionization: Processes, materials and state of the technology," *Journal of Electroanalytical Chemistry,* vol. 813, pp. 178-192, 2018.

[62] G. S. Manning, "Nonconvective Ionic Flow in Fixed‐Charge Systems," *The Journal of Chemical Physics,* vol. 46, no. 6, pp. 2324-2333, 1967.

[63] G. S. Manning, "Limiting laws and counterion condensation in polyelectrolyte solutions II. Self‐diffusion of the small ions," *The Journal of Chemical Physics,* vol. 51, no. 3, pp. 934-938, 1969.

[64] E. J. Dickinson, J. G. Limon-Petersen, and R. G. Compton, "The electroneutrality approximation in electrochemistry," *Journal of Solid State Electrochemistry,* vol. 15, no. 7-8, pp. 1335-1345, 2011.

[65] J. Bear, *Dynamics of fluids in porous media*. Courier Corporation, 2013.

[66] R. Millington and J. Quirk, "Permeability of porous solids," *Transactions of the Faraday Society,* vol. 57, pp. 1200-1207, 1961.

[67] J. Mackie and P. Meares, "The diffusion of electrolytes in a cation-exchange resin membrane I. Theoretical," *Proceedings of the Royal Society of London. Series A. Mathematical and Physical Sciences,* vol. 232, no. 1191, pp. 498-509, 1955.

[68] J.-H. Lee and J.-H. Choi, "The production of ultrapure water by membrane capacitive deionization (MCDI) technology," *Journal of membrane science,* vol. 409, pp. 251-256, 2012.

[69] H. Li, C. Nie, L. Pan, and Z. Sun, "A Comparative Study between Membrane Capacitive Deionization and Capacitive Deionization from Isotherms and Kinetics," in *Proceedings of Shang-hai International Nanotechnology Cooperation Symposium*, 2011, pp. 110-113.

[70] Y. Liu, C. Nie, L. Pan, X. Xu, Z. Sun, and D. H. Chua, "Carbon aerogels electrode with reduced graphene oxide additive for capacitive deionization with enhanced performance," *Inorganic Chemistry Frontiers,* vol. 1, no. 3, pp. 249-255, 2014.

[71] R. L. Zornitta and L. A. Ruotolo, "Simultaneous analysis of electrosorption capacity and kinetics for CDI desalination using different electrode configurations," *Chemical Engineering Journal,* vol. 332, pp. 33-41, 2018.

[72] P. Biesheuvel, S. Porada, M. Levi, and M. Z. Bazant, "Attractive forces in microporous carbon electrodes for capacitive deionization," *Journal of solid state electrochemistry,* vol. 18, no. 5, pp. 1365-1376, 2014.

[73] J. Vanderborght and H. Vereecken, "Review of dispersivities for transport modeling in soils," *Vadose Zone Journal,* vol. 6, no. 1, pp. 29-52, 2007.

[74] G. Tian, L. Liu, Q. Meng, and B. Cao, "Preparation and characterization of cross-linked quaternised polyvinyl alcohol membrane/activated carbon composite electrode for membrane capacitive deionization," *Desalination,* vol. 354, pp. 107-115, 2014.

[75] J. Chang, K. Tang, H. Cao, Z. Zhao, C. Su, Y. Li, F. Duan, and Y. Sheng, "Application of anion exchange membrane and the effect of its properties on asymmetric membrane capacitive deionization," *Separation and Purification Technology,* vol. 207, pp. 387-395, 2018.

[76] A. Hassanvand, K. Wei, S. Talebi, G. Q. Chen, and S. E. Kentish, "The role of ion exchange membranes in membrane capacitive deionisation," *Membranes,* vol. 7, no. 3, p. 54, 2017.

[77] S. Porada, M. Bryjak, A. Van Der Wal, and P. Biesheuvel, "Effect of electrode thickness variation on operation of capacitive deionization," *Electrochimica Acta,* vol. 75, pp. 148-156, 2012.

[78] K. Z. Huang and H. L. Tang, "Temperature and desorption mode matter in capacitive deionization process for water desalination," *Environmental technology,* pp. 1-8, 2019.

[79] J. Dykstra, S. Porada, A. Van Der Wal, and P. Biesheuvel, "Energy consumption in capacitive deionization–Constant current versus constant voltage operation," *Water research,* vol. 143, pp. 367-375, 2018.

[80] V. M. Palakkal, J. E. Rubio, Y. J. Lin, and C. G. Arges, "Low-resistant ion-exchange membranes for energy efficient membrane capacitive deionization," *ACS Sustainable Chemistry & Engineering,* vol. 6, no. 11, pp. 13778-13786, 2018.

CHAPTER 4

ENERGY PERFORMANCE OF CONSTANT VOLTAGE MEMBRANE CAPACITIVE DEIONIZATION FOR DESALINATION OF BRACKISH WATER[3]

4.1. Abstract

Membrane capacitive deionization (MCDI) is a portable and energy efficient technique for desalinating brackish waters to augment freshwater supply. In this work, the energy performance of constant voltage (CV) mode MCDI was analyzed theoretically using two operational modes, maximizing salt removal efficiency (cut-off mode), and maximizing total salt removal (equilibrium mode). Trade-offs between salt removal efficiency and water recovery were evaluated. Cut-off mode generally possessed higher specific energy consumption (SEC) but greater thermodynamic energy efficiency (TEE) at moderate water recovery compared to equilibrium mode. External resistive losses became dominant with high water recovery in cut-off mode, while pumping losses were dominant in equilibrium mode. In both cycle modes, 20-40% of SEC was stored in the electric double layer (EDL). Increasing cell length significantly increased pump energy requirements, while increasing applied voltage increased ion transfer resistive losses and energy storage in the EDL. When desalinating near-fresh water (15 mM) under moderate water recovery (75%), cut-off CV mode MCDI approached 30% TEE if recovery of 50% of the stored energy can be achieved. CV mode MCDI was competitive to RO under these conditions. CV mode MCDI was more efficient than constant current (CC) mode MCDI with low salinity feed water (3000 mg/L) and moderate water recovery.

[3] This chapter is submitted as: Zhang, X, Reible, D. Energy performance of constant voltage membrane capacitive deionization for desalination of brackish water, Water research, under review, 2021.

4.2. Graphical Abstract

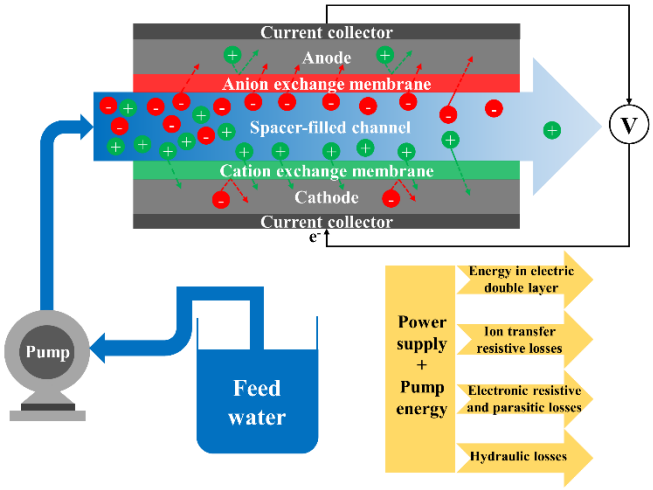

4.3. Introduction

A variety of trends in modern society have increased demands for high quality water without a corresponding increase in supply, ultimately limiting socio-economic development and threatening food security [1, 2]. Monitoring water scarcity and improving the efficiency of water utilization can ease the pressures on water supply [3, 4]. But desalinating brackish waters is an effective alternative for augmenting freshwater supply [5, 6]. Capacitive deionization (CDI) is an emerging desalination technique with portable cell assembly, satisfactory energy consumption, controllable effluent concentration, and selective ion removal [7]. Membrane CDI (MCDI) is a widely studied CDI variant, which employs ion-exchange membrane (IEM) to improve charge efficiency, salt removal rate and adsorption capacity [8].

In MCDI, cation-exchange membrane (CEM) and anion-exchange membrane (AEM) are inserted between a pair of porous electrodes and a porous spacer-filled channel. Schematic diagrams of desalination and regeneration steps of MCDI including ion transfer routes and energy flow paths are shown in Figure 4.1. During desalination (Figure 4.1 (a)), ions are attracted toward the oppositely charged electrode, and are temporarily trapped in the electric double layer (EDL) near the surface of electrode micropores [9, 10]. The input energy includes energy consumed to charge the electrodes and pumping the brackish water through the porous media spacer. Electrical energy losses mainly consist of resistive losses and parasitic losses from Faradaic reactions [11]. The residual energy is temporarily stored in the EDL as ions are getting adsorbed. During regeneration (Figure 4.1 (b)), MCDI is either short-circuited or inversely

charged to repel the temporarily stored ions from the porous electrodes back to the channel. This dissipation of ions in EDL during regeneration leads to a current flow that can be stored and used to help power the system [12].

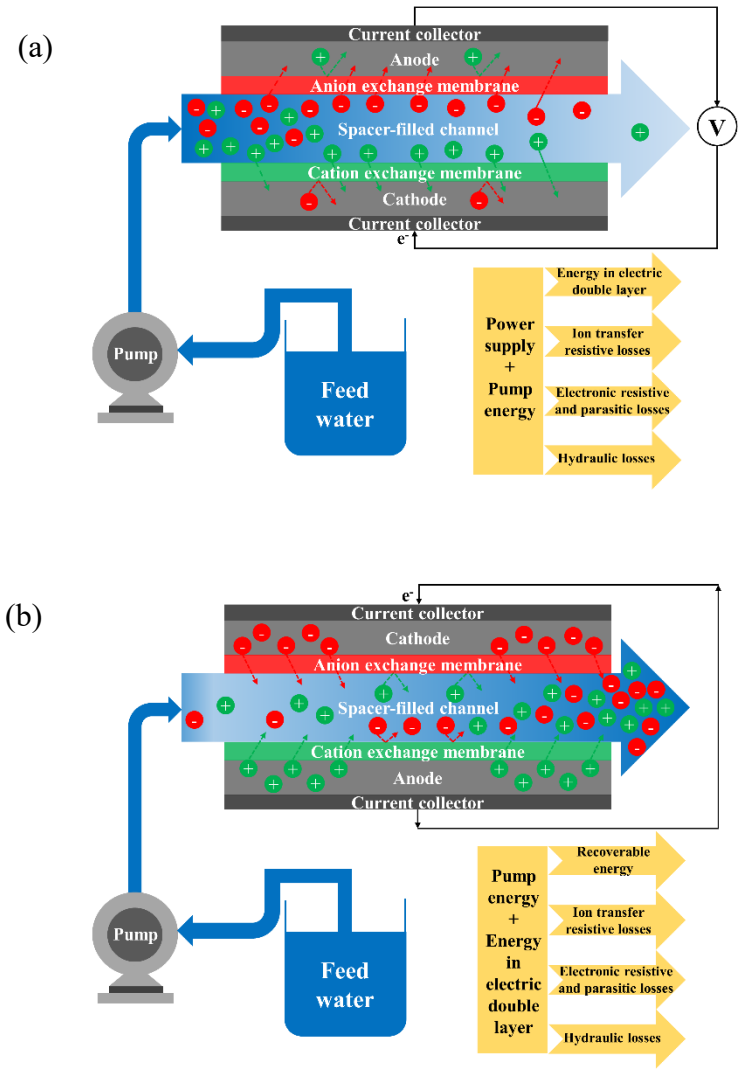

Figure 4.1. Schematic diagrams of MCDI including ion transport routes and energy flow paths of (a) desalination step, and (b) regeneration step.

Energy performance is an important metric of desalination techniques. Energy consumption of MCDI can be small when desalinating saline waters with low total dissolved solids (TDS) [13]. But traditional desalination techniques such as reverse osmosis (RO) and electrodialysis (ED) have been found to have lower energy consumption and higher energy efficiency for a given average water flux, water recovery, salt removal efficiency and feed water salinity [14, 15]. Porada et al. [16], however, implemented an intermittent flow mode to achieve a significantly high water recovery, making MCDI more energy efficient than RO. Photovoltaic energy powered MCDI modules have shown competitive SEC and relatively high water recovery compared to RO [17], indicating MCDI to be promising for less energy-sensitive applications. Most studies concluded that constant current (CC) mode (M)CDI was more energy efficient than constant voltage (CV) mode (M)CDI [18-20]. However, Wang and Lin [21] set the same target adsorption in both CC and CV modes and revealed that which mode was more energy efficient largely depended on the target adsorption and the deviations between CC and CV modes were small [21].

Energy performance of MCDI can be improved by reducing system resistance [11], optimizing operating conditions [13, 22], and recovering the temporarily stored energy in EDL with energy recovery devices (ERD) [23]. Low-resistance electrodes [22], use of thin spacer with large porosity [24] and a thin IEM [25] help reduce system resistance. Removing excess organic matter in feed water in pretreatment steps prevents organic fouling of MCDI, decreases resistance and enhances cell stability [26]. Alternative operating modes such as implementing an intermediate step between desalination and

regeneration steps [27] and applying a high concentration feed solution during regeneration to enhance ion transfer rate [28] also help increase energy efficiency. Thermodynamic energy efficiency (TEE) is the ratio of the thermodynamic minimum energy consumption of ion separation over the actual energy consumption [29, 30]. TEE can be improved by increasing charge efficiency, introducing intercalation electrodes, optimizing operating conditions, and employing ERDs [29]. Use of a thin channel [31], zero flow rate during regeneration [32], low charging current during regeneration [23], and moderate water recovery [13] can enhance energy recovery.

Tuning cycle modes by adjusting operating duration can change cell performance and energy consumption. Demirer et al. [33] enhanced energy efficiency by cycling CDI at the highest amount of adsorbed salt per input energy, and maximized salt removal per input energy per volume of feed water by cycling CDI at maximum average salt removal rate. Zhang and Reible [34] optimized the salt removal efficiency per cycle by cycling MCDI at the minimum average effluent concentration. Salamat and Hidrovo et al. [35] proposed a multi-cycle CDI by treating the product water of the previous cycle as the input in the following desalination step to improve salt removal efficiency.

Due to the low permeability of commonly used porous media spacer, the pressure drop in MCDI channel is much higher compared to that of an open channel or a channel with a mechanical spacer. Despite this, pumping energy is rarely part of assessment of M(CDI) performance. Laxman et al. [36] reduced the pressure drop in the CDI channel by modifying the port architecture of CDI to achieve a better flow distribution and decrease the average velocity in the channel. The permeability of the porous spacer is a

function of the porosity and critical pore size [37]. Guyes et al. [38] produced a perforated electrode with an improved permeability by several orders of magnitude, which significantly reduced fluid pressure drop in a flow-through CDI.

(M)CDI process models [15, 39] and simplified Randles circuit models [14, 40] have been applied for studying energy-related behaviors of (M)CDI. The present work aims at investigating the energy requirements of CV mode MCDI with varying water recovery in two cycle modes, (1) maximizing salt removal efficiency and 2) total salt removal, via our two-dimensional MCDI process model [34], and comparing specific energy consumption (SEC) and TEE between CV mode MCDI and CC mode MCDI. The contributions of this study include: 1) pump losses are included in the calculation of SEC of MCDI; 2) trade-offs between water recovery and salt removal efficiency are evaluated; 3) TEE of CV mode MCDI is evaluated and compared with the reported TEE of RO with near-fresh water at moderate water recovery 4) the energy requirements of both cut-off (maximizing salt removal efficiency) and equilibrium (maximizing total salt removal) cycle modes of CV mode are analyzed and compared with CC mode. This work depicts a clear picture of energy consumption in a full MCDI cycle including pump losses, external resistive losses, ionic transfer resistive losses and energy storage in EDL under varying operating conditions.

4.4. MCDI configuration and operating conditions

In this work, a CV mode MCDI with continuous flow is assembled as described in our recent publication [34]. A full operating cycle consists of a desalination step followed

by a regeneration step. The MCDI is short-circuited during regeneration. Two cycle modes are employed including cut-off mode, which switches to regeneration to maximize salt removal efficiency [34], and equilibrium mode, which switches to regeneration after adsorption at the electrode has reached a maximum and is saturated. The transient effluent concentration curves of these two modes can be found in Figure A.1 in the supporting information. Water recovery, W_r, is the volume ratio of product water over feed water:

$$W_r = \frac{Q_d t_d}{Q_d t_d + Q_r t_r} \tag{4.1}$$

where t_d and t_r are the operating durations in desalination and regeneration steps, respectively, and Q_d and Q_r are the flow rates in desalination and regeneration steps, respectively. In this study, operating durations of desalination and regeneration steps are kept the same ($t_d = t_r$). Water recovery is tuned by adjusting the flow rate during regeneration.

Water productivity, W_p, is defined as the average flux of the product water [15]:

$$W_p = \frac{\frac{Q_d t_d}{t_d + t_r}}{A_m} \tag{4.2}$$

where A_m is the area of IEM:

$$A_m = L \times W \tag{4.3}$$

where L is the cell length, and W is the cell width. In this study, water productivity is set as a constant, so flow rate varies with cell configuration.

Detailed MCDI configuration parameters and operating conditions are based on reported parameters [15, 34] and are shown in Table 4.1.

Table 4.1. MCDI configuration parameters and operating conditions

Parameter		**Value**	**Unit**
Feed water properties	Concentration	15, 20, 51.28*	[mol/m^3]
	Viscosity	8.9×10^{-4}	[Pa·s]
Cell properties	External resistance	0.6	[Ω]
	Cell length	0.1-0.2, 0.1*	[m]
	Electrode thickness	0.15	[mm]
	Macropore porosity	0.4, 0.43*	-
	Micropore porosity	0.3	-
	Micropore capacitance	150, 120*	[MF/m^3]
	IEM thickness	0.13	[mm]
	IEM fixed charge density	1000, 3000*	[mol/m^3]
	Spacer thickness	0.3	[mm]
	Spacer porosity	0.71	-
	Spacer fiber radius	3.5×10^{-3}	[mm]
	Spacer permeability	1.23×10^{-12}	[m^2]
Operating conditions	Water productivity	15	[L/m^2/h]
	Water recovery	50%-90%	-
	Applied voltage	0.8-1.0, 1.2*	[V]

* Parameters only used in Section 4.6.3, where properties of the electrode and IEM are kept the same as ref. [15].

Our MCDI process model describes ion transport in the channel, IEM and electrode with an extended Nernst-Planck equation, which incorporates hydraulic dispersion effects, and simulates ion adsorption in electrode with modified Donnan theory. Mathematical development of this model is described in [34]. This model is used to

calculate transient concentrations and potential drop in each cell element and transient effluent concentration based on the configuration parameters and operating conditions. The simulated data are used to calculate the energy requirements for the (M)CDI.

4.5. MCDI energy performance indicators

Electronic resistive losses of the electrode and parasitic losses are insignificant within the range of feed water concentrations and applied voltages in this study [19, 24]. Energy required for charging the cell by the external power supply during desalination per unit volume of product water, E_{eps}, is calculated by:

$$E_{eps} = \frac{\int_0^{t_d} V_{cell} I_{ext} dt}{Q_d t_d} \tag{4.4}$$

where V_{cell} is the applied voltage, which is a sum of the electric potential drop on the external resistance and the electrode pair:

$$V_{cell} = V_e + I_{ext} R_{ext} \tag{4.5}$$

where V_e is the electric potential drop on the electrode pair, R_{ext} is the external resistance including wire resistance, current collector resistance and contact resistance on the current collector-electrode interface [24], and I_{ext} is the external current, which is related to the temporal variation rate of charge in the EDL [41]:

$$I_{ext} = \iint p_m F \frac{\partial(\sum z_i c_i)}{\partial t} W dx dy \tag{4.6}$$

where p_m is the porosity of the micropores, F is Faraday's constant (96485 C/mol), z_i is the valence of species i, c_i is the concentration of species i in macropores, t is the

operating time, and x and y are the thickness and length directions, respectively. The integral interval is the cathode domain to make sure the calculated I_{ext} during desalination is positive.

Specific energy consumption on the external resistance during desalination, E_{ext}, is represented by:

$$E_{ext} = \frac{\int_0^{t_d} I_{ext}^2 R_{ext} dt}{Q_d t_d} \tag{4.7}$$

The specific energy consumption of the cell pair, E_{cell}, is then given by

$$E_{cell} = E_{eps} - E_{ext} \tag{4.8}$$

E_{cell} includes ionic transfer resistive losses in the electrode, IEM and channel and energy storage in EDL.

The temporarily stored specific energy in EDL during desalination, E_{EDL}, is represented by [42]:

$$E_{EDL} = \frac{\frac{1}{2} C \Delta V^2}{Q_d t_d} \tag{4.9}$$

where ΔV is the accumulated potential in EDL, and C is the capacitance of the electrode pair, which is related to the volumetric capacitance of micropores, C_{st} [41]:

$$C = \frac{C_{st} p_m W L L_e}{2} \tag{4.10}$$

where L_e is the thickness of a single electrode. The capacitance of a symmetric electrode pair is a half of that of a single electrode.

ΔV is a sum of the Stern layer potential drop, φ_{st}, and Donnan potential, φ_D of both electrodes:

$$\Delta V = 2(\varphi_{st} + \varphi_D) \tag{4.11}$$

E_{EDL} is the theoretically maximum recoverable energy and can be partially recovered into a chargeable battery or a supercapacitor via a buck-boost converter during regeneration [12, 31]. We assume here that up to 50% of this is recoverable.

Pump energy compensates for hydraulic losses. Specific pump energy of a full cycle, E_{pump}, is calculated by:

$$E_{pump} = \frac{\Delta P_d Q_d t_d + \Delta P_r Q_r t_r}{Q_d t_d} \tag{4.12}$$

where ΔP_d and ΔP_r are the pressure drops of the feed water through the spacer-filled channel during desalination and regeneration, respectively. The pressure drops are calculated based on Darcy's law [43]:

$$\Delta P_d = \frac{\mu Q_d L}{k A_c} \tag{4.13}$$

$$\Delta P_r = \frac{\mu Q_r L}{k A_c} \tag{4.14}$$

where μ is the viscosity of feed water, k is the permeability of the porous spacer, and A_c is the cross-sectional area of the channel:

$$A_c = L_{ch} \times W \tag{4.15}$$

where L_{ch} is the thickness of the channel.

Permeability increases with porosity and critical pore size of porous media [37, 44], and also increases with fiber radius in fibrous porous media [45, 46]. In this study, permeability is estimated by [45]:

$$\frac{k}{a^2} = f(\varepsilon_s) \tag{4.16}$$

where ε_s is the porosity of the spacer, and a is the fiber radius of fibrous porous spacer. In this study, a is assumed to be the same as that of fiberglass, and $f(\varepsilon_s)$ is estimated based on the reported experimental data in [45].

The total specific energy consumption of MCDI, SEC, is the specific energy input in a full cycle:

$$SEC = E_{eps} + E_{pump} \tag{4.17}$$

The minimum energy needed in desalination is process-independent and equals to Gibbs free energy of ion separation [47]. In a fully dissociated monovalent solution, the minimum ion separation energy required per unit volume of product water, E_{min}, is calculated by [29, 47]:

$$E_{min} = 2RT\left\{\frac{c_0}{W_r}\ln\left[\frac{c_0 - W_r c_d}{c_0(1-W_r)}\right] - c_d \ln\left[\frac{c_0 - W_r c_d}{c_d(1-W_r)}\right]\right\} \tag{4.18}$$

Here, R is the universal gas constant (8.314 J/mol/K), T is the ambient temperature, c_0 is the feed water concentration, and c_d is the product water concentration.

TEE is the ratio of E_{min} over SEC [29]:

$$\text{TEE} = \frac{E_{min}}{SEC} \tag{4.19}$$

4.6. Results and discussion

4.6.1. Trade-offs between water recovery and salt removal efficiency

Five consecutive cycles are run in both cut-off mode and equilibrium mode with water recovery from 50 to 90%. The corresponding salt removal efficiencies per cycle are shown in Figure 4.2.

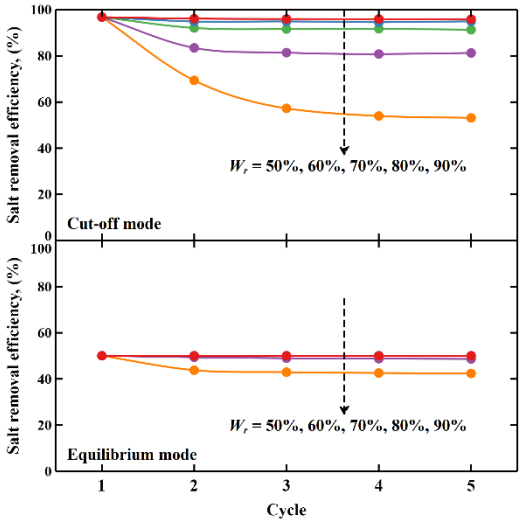

Figure 4.2. Salt removal efficiency per cycle in cut-off mode and equilibrium mode. Water recovery is 50%, 60%, 70%, 80% and 90% from top to bottom successively. Feed water concentration is 20 mM, applied voltage is 0.8 V and cell length is 10 cm.

Due to the incomplete desorption from the electrode during regeneration, the adsorption decreases initially before achieving a quasi-steady condition under high water recovery (see Figure A.1). Hence, salt removal efficiency is lower under quasi-steady conditions compared to that of the first cycle, especially with high water recovery. Quasi-steady conditions are reached within five cycles. Cut-off mode outperforms equilibrium mode with respect to salt removal efficiency, which is above 90% under moderate water

recovery (50%-70%). The reduction in salt removal efficiency at higher water recovery, however, is larger in cut-off mode compared to equilibrium mode due to the short duration of regeneration.

4.6.2. Energy performance of MCDI under quasi-steady conditions

SEC including the specific energy consumption of the pump (E_{pump}), external resistance (E_{ext}), and cell pair (E_{cell}) and energy storage in EDL (E_{EDL}) of both cut-off and equilibrium modes with varying water recovery from 50%-90% are shown in Figure 4.3. Data of the fifth cycle are employed in the calculation to represent quasi-steady state.

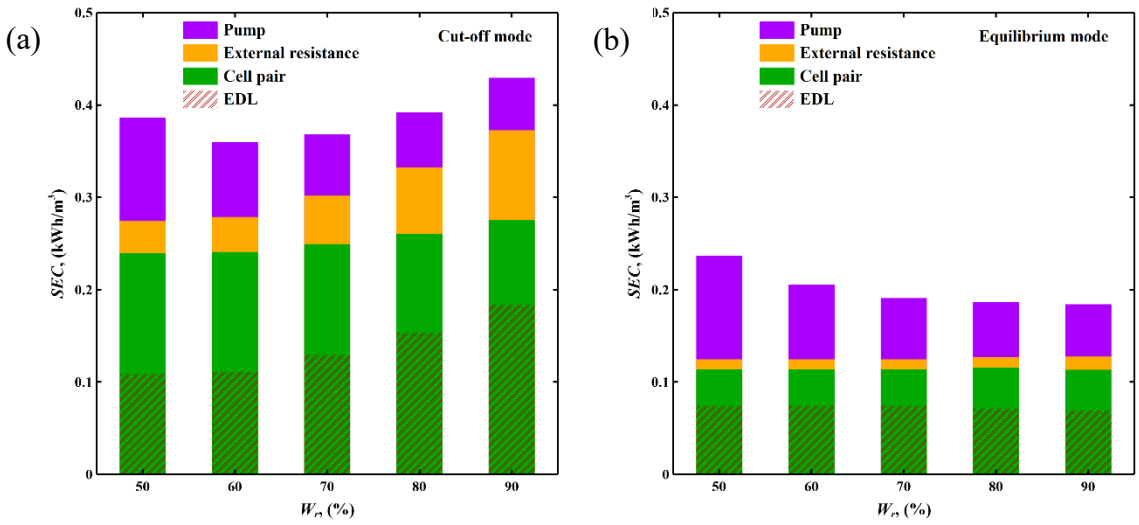

Figure 4.3. SEC of the fifth cycle in (a) cut-off mode and (b) equilibrium mode with the contribution of each component including pump, external resistance, cell pair and energy stored in EDL. Feed water concentration is 20 mM, applied voltage is 0.8 V and cell length is 10 cm.

SEC of cut-off mode is generally higher than that of equilibrium mode, which is attributed to the low current flow as electrode approaches saturation in equilibrium mode (see Figure A.2). The minimum SEC is achieved under water recovery of 60% in cut-off mode and water recovery of 90% in equilibrium mode. Pump energy requirements are independent of cycle modes. The decrease of pump energy at high water recovery is due to the reduced flow rate during regeneration. In cut-off mode, external resistive losses increase with water recovery and dominate at high water recovery. Energy stored in EDL increases with water recovery in cut-off mode due to the increased accumulated potential in EDL during desalination (see Figure A.3). The energy stored in EDL under water recovery of 90% represents more than 40% of SEC in cut-off mode. In equilibrium mode with moderate water recovery, external resistive losses are negligible, while pump losses are dominant. The recoverable energy is that which accumulates in the EDL and is over 50% of the energy consumed in cell pair among all cases in equilibrium mode and is 40%-70% in cut off mode.

The effects of cell length and applied voltage on SEC are explored by showing the specific energy consumption of each part including the pump (E_{pump}), external resistance (E_{ext}), and cell pair (E_{cell}) and energy storage in EDL (E_{EDL}) versus different cell lengths and applied voltages in both cut-off and equilibrium modes under water recovery of 50% in Figure 4.4.

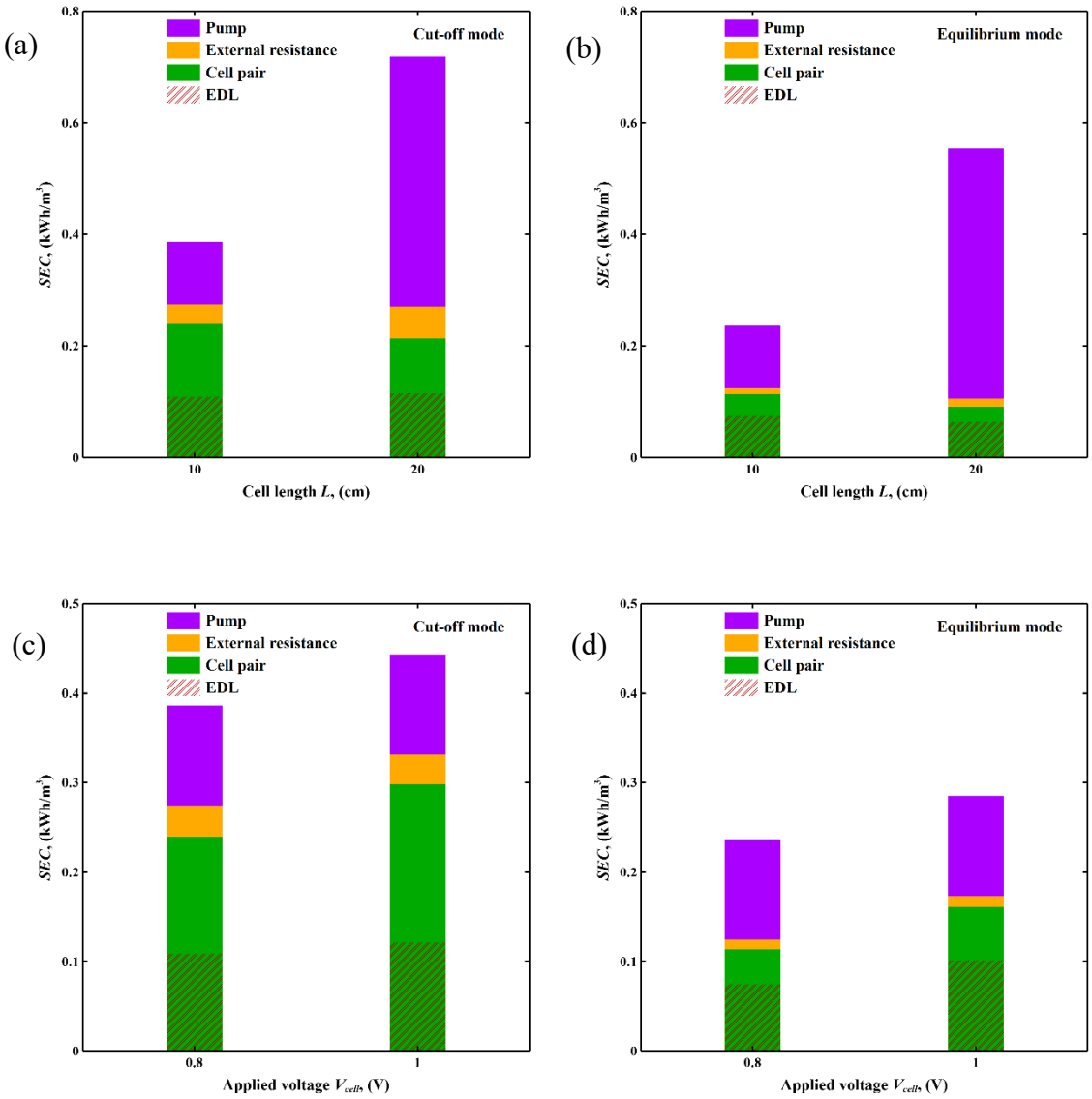

Figure 4.4. SEC with the contribution of each component including pump, external resistance, and cell pair and energy stored in EDL versus cell length in the fifth cycle of (a) cut-off mode and (b) equilibrium mode with applied voltage of 0.8 V and water recovery of 50%; SEC with the contribution of each component including pump, external resistance, and cell pair and energy stored in EDL versus applied voltage in the fifth cycle of (c) cut-off mode and (d) equilibrium mode with feed water concentration of 20 mM, cell length of 10 cm and water recovery of 50%.

In both cycle modes, SEC of the longer cell is 2-2.5 times as much as that of the shorter cell, which is the result of both increased length and increased flow rate to maintain fixed water productivity (flow per unit electrode area). Pump losses can be very high in large-scale MCDI from the high pressure drop through the porous media spacer (see Figure A.4). Reduction in pressure losses in the porous spacer would allow longer MCDI cells to be used without a substantial penalty in energy consumption. Hence, long cell length is not recommended in MCDI unless porous media spacer with high permeability is employed to significantly reduce the pressure drop in the channel.

By increasing the applied voltage, the driving force of the ionic species and the adsorption capacity of the electrode are enhanced thus increasing the overall energy consumption. Higher applied voltage also contributes to the accumulation of potential in EDL, however, leading to an increased energy storage on EDL making more energy available for recovery. Pump losses are not influenced by applied voltage.

TEE of both cut-off and equilibrium modes MCDI without energy recovery or with 50% energy recovery under water productivity of 5, 15, 25 L/m^2/hr are shown in Figure 4.5. For comparison the approximate TEE of reverse osmosis with a similar feed concentration (15 mM) and 75% water recovery is shown [29]. Here the 50% energy recovery refers to harvesting 50% of the energy stored in EDL during regeneration. A part of the energy stored in the EDL is wasted as external resistive losses and ion transfer resistive losses during regeneration but 50% is a conservative estimate of what could be recovered.

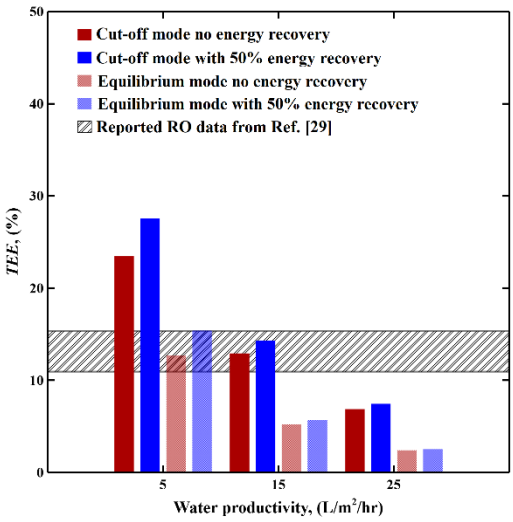

Figure 4.5. TEE of the fifth cycle in cut-off and equilibrium modes MCDI without energy recovery or with 50% water recovery under varying water productivity, and the reported TEE of RO in ref. [29]. For both MCDI and RO, feed water concentration is 15 mM, and water recovery is 75%. In MCDI, cell length is 10 cm, and applied voltage is 0.8 V.

Cut-off mode generally achieves a higher TEE compared to equilibrium mode. Although cut-off mode consumes more energy (see Figure 4.4), the high salt removal efficiency offsets this energy consumption in estimation of the TEE. TEE of cut-off mode MCDI exceeds 20%, and approaches 30% considering 50% energy recovery, which is higher than the reported TEE of RO shown in Figure 4.5, and exceeds the reported TEE of conventional (M)CDI [29]. TEE decreases with increasing water productivity, which is in accordance with the trade-off between desalination kinetics performance and energy efficiency that was identified by Wang and Lin [48]. The superiority of MCDI over RO on energy efficiency can be only achieved at the expense of reducing the water throughput.

4.6.3. Comparison of energy performance between CV and CC modes MCDI

Figure 4.6 compares the salt removal efficiency, SEC and TEE for MCDI in CV versus CC modes. In this comparison, the properties of the electrode and IEM, feed water concentration and water productivity are kept the same as ref. [15] (see Table 4.1). The results suggest that cut-off CV mode can lead to greater salt removal efficiency and greater TEE at low to moderate water recoveries (50-70%).

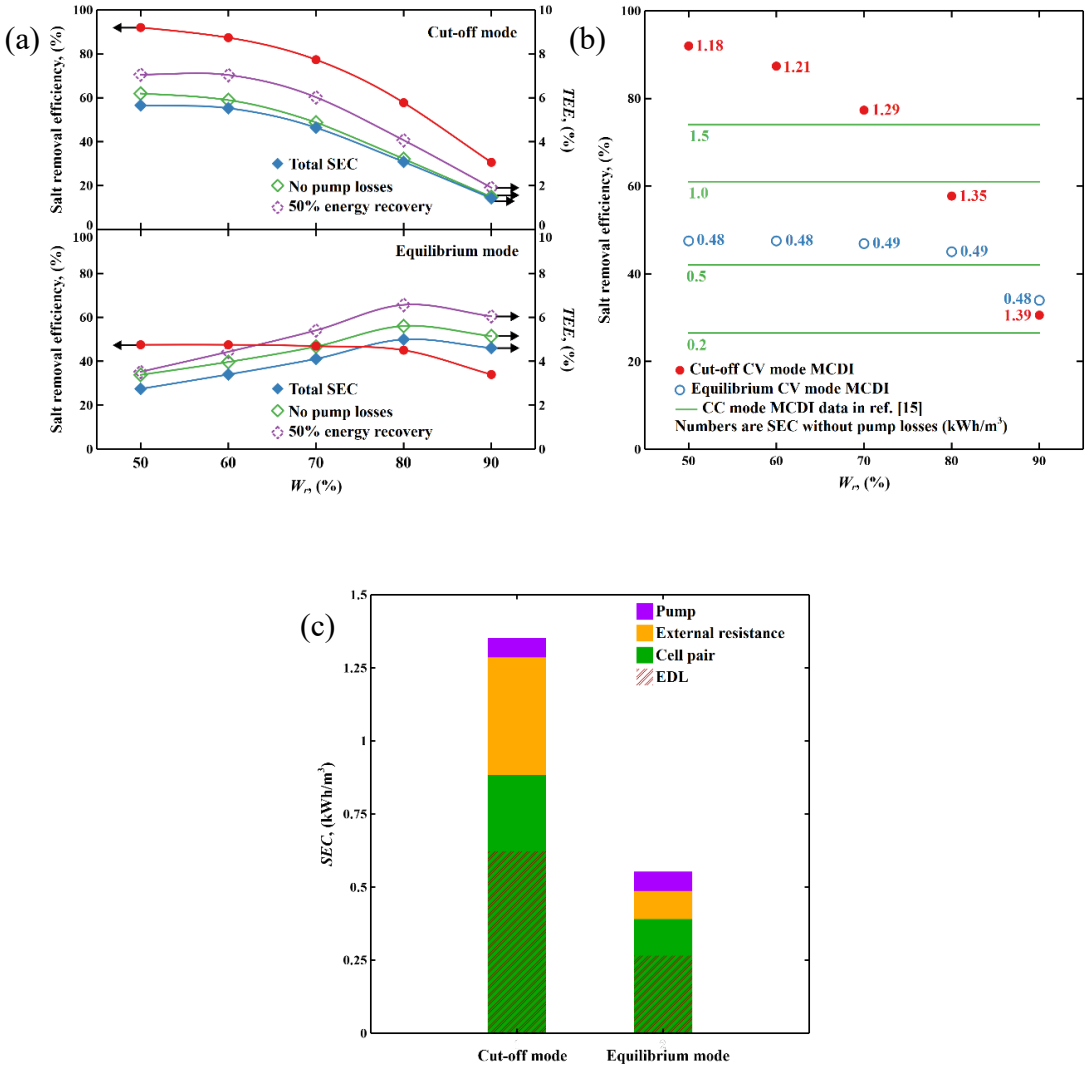

Figure 4.6. (a) Salt removal efficiency and TEE considering SEC, SEC neglecting pump energy requirements, and SEC with 50% energy recovery versus water recovery of 50-90% of quasi-steady state in cut-off and equilibrium CV modes MCDI. (b) Salt removal efficiency and SEC without pump losses versus water recovery of 50-90% of quasi-steady state in cut-off and equilibrium CV modes MCDI and the reported data of CC mode MCDI in ref. [15]. (c) SEC with the contribution of each component including pump, external resistance, and cell pair and energy stored in EDL in both cut-off and equilibrium CV modes MCDI with water recovery of 70%.

As shown in Figure 4.6 (a) the salt removal efficiency and TEE using CV cut-off mode are much higher than that of equilibrium mode at low water recoveries. At high water recoveries, the salt removal efficiencies of the two modes are similar. TEE decreases with increasing water recovery in cut-of mode and increases with water recovery in equilibrium mode under moderate water recovery (50-80%). Without considering pump losses, TEE of both cut-off and equilibrium modes increases. In cut-off mode, pump losses exert less effect on TEE under high water recovery due to the small proportion of pump losses in the relatively high SEC. However, the percentage of pump losses in the overall SEC of equilibrium mode is higher than that of cut-off mode. Energy recovery improves TEE significantly in both cycle modes. By assuming 50% of the energy stored in EDL is recovered, TEE increases by 20% to 30% in both cycle modes.

As shown in Figure 4.6 (b) the CC mode MCDI salt removal efficiency is independent of water recovery but strongly dependent upon SEC. The CV mode salt removal efficiency is a strong function of water recovery. Cut-off CV mode can reach high salt removal efficiency under moderate water recovery (< 70%), which is either inaccessible or requires more energy input in CC mode. Equilibrium CV mode also possesses lower SEC compared to CC mode below water recovery of 80%, although the deviations between equilibrium CV mode and CC mode are small except at high water recoveries.

As shown in Figure 4.6 (c), the relatively high SEC in cut-off mode is because of the ion transfer resistive losses in the cell and the dominant external resistive losses. External resistive losses are more dominant in cut-off mode compared to equilibrium mode. Energy storage in EDL accounts for about 50% of SEC in both cut-off and

equilibrium modes. Hence, SEC can be significantly reduced by applying ERDs during regeneration.

4.7. Conclusion and Outlook

In this work, the energy performance of both cut-off and equilibrium CV modes MCDI are investigated via our MCDI process model [34]. This study showed: 1) Salt removal efficiency is high at lower water recoveries (<70%) in CV cut-off mode but decreases significantly at high water recoveries due to the incomplete desorption from the electrode during regeneration with increasing water recovery; 2) Cut-off mode is generally higher in SEC and possesses larger TEE under moderate water recovery compared to equilibrium mode. Pump losses are dominant in equilibrium mode. External resistive losses become dominant under high water recovery in cut-off mode. Energy stored in EDL accounts for 20-40% of SEC in both cut-off and equilibrium modes. Prolonging cell length significantly increases pump losses, while increasing applied voltage increases ionic transfer resistive losses in the cell pair but contributes to energy storage in EDL. 3) TEE of both cut-off and equilibrium CV modes MCDI decreases with increasing water productivity. When desalinating near-fresh water (15 mM) with 50% energy recovery and 75% water recovery in cut-off mode, TEE approaches 30%, which is higher than that of RO but at reduced water productivity. 4) CV mode MCDI outperforms CC mode MCDI under moderate water recovery by reaching a lower SEC in both cycle modes and achieving a much higher salt removal efficiency in cut-off mode. This study evaluates cut-off and equilibrium CV modes MCDI, and reveals the superiority of CV mode MCDI at moderate water recoveries

compared to CC mode MCDI by being more energy efficient, and yielding much higher salt removal in cut-off mode.

Challenges of achieving a satisfactory energy performance of MCDI include nonnegligible electronic resistive losses, parasitic losses and hydraulic losses. Contact resistance is the dominant external resistance, and can be reduced by coating IEM/ion exchange polymers onto the electrode, introducing silver epoxy contact between the current collector and the electrode, and compressing the cell elements with sufficient pressure [40]. External resistive losses in CV mode MCDI is less than that of CC mode MCDI, especially when high current is applied in the latter cell. Parasitic losses can be suppressed by tuning the operating conditions to avoid long exposure of electrodes under high voltage or modifying the electrode surface with functional groups [49]. Pump losses become dominant in large cells so small MCDI cells are preferred. By assembling MCDI units in series, the overall capacity and water throughput can be increased. Pump losses can be reduced by enlarging the porosity and critical pore size in pore media spacer to improve the permeability of the spacer channel. Employing ERDs during regeneration can further reduce SEC and improve TEE, making MCDI more energy efficient.

4.8. References

[1] N. Mancosu, R. L. Snyder, G. Kyriakakis, and D. Spano, "Water scarcity and future challenges for food production," *Water,* vol. 7, no. 3, pp. 975-992, 2015.

[2] M. M. Mekonnen and A. Y. Hoekstra, "Four billion people facing severe water scarcity," *Science advances,* vol. 2, no. 2, p. e1500323, 2016.

[3] S. N. Gosling and N. W. Arnell, "A global assessment of the impact of climate change on water scarcity," *Climatic Change,* vol. 134, no. 3, pp. 371-385, 2016.

[4] J. Liu, H. Yang, S. N. Gosling, M. Kummu, M. Flörke, S. Pfister, N. Hanasaki, Y. Wada, X. Zhang, and C. Zheng, "Water scarcity assessments in the past, present, and future," *Earth's future,* vol. 5, no. 6, pp. 545-559, 2017.

[5] N. Ghaffour, T. M. Missimer, and G. L. Amy, "Technical review and evaluation of the economics of water desalination: current and future challenges for better water supply sustainability," *Desalination,* vol. 309, pp. 197-207, 2013.

[6] S. Honarparvar, X. Zhang, T. Chen, C. Na, and D. Reible, "Modeling technologies for desalination of brackish water—toward a sustainable water supply," *Current Opinion in Chemical Engineering,* vol. 26, pp. 104-111, 2019.

[7] M. Suss, S. Porada, X. Sun, P. Biesheuvel, J. Yoon, and V. Presser, "Water desalination via capacitive deionization: what is it and what can we expect from it?," *Energy & Environmental Science,* vol. 8, no. 8, pp. 2296-2319, 2015.

[8] W. Tang, J. Liang, D. He, J. Gong, L. Tang, Z. Liu, D. Wang, and G. Zeng, "Various cell architectures of capacitive deionization: recent advances and future trends," *Water Res.,* vol. 150, pp. 225-251, 2019.

[9] P. Biesheuvel, Y. Fu, and M. Bazant, "Electrochemistry and capacitive charging of porous electrodes in asymmetric multicomponent electrolytes," *Russian Journal of Electrochemistry,* vol. 48, no. 6, pp. 580-592, 2012.

[10] P. Biesheuvel, Y. Fu, and M. Z. Bazant, "Diffuse charge and Faradaic reactions in porous electrodes," *Physical Review E,* vol. 83, no. 6, p. 061507, 2011.

[11] A. Hemmatifar, J. W. Palko, M. Stadermann, and J. G. Santiago, "Energy breakdown in capacitive deionization," *Water Res.,* vol. 104, pp. 303-311, 2016.

[12] J. Kang, T. Kim, H. Shin, J. Lee, J.-I. Ha, and J. Yoon, "Direct energy recovery system for membrane capacitive deionization," *Desalination,* vol. 398, pp. 144-150, 2016.

[13] R. Zhao, S. Porada, P. Biesheuvel, and A. Van der Wal, "Energy consumption in membrane capacitive deionization for different water recoveries and flow rates, and comparison with reverse osmosis," *Desalination,* vol. 330, pp. 35-41, 2013.

[14] M. Qin, A. Deshmukh, R. Epsztein, S. K. Patel, O. M. Owoseni, W. S. Walker, and M. Elimelech, "Comparison of energy consumption in desalination by capacitive deionization and reverse osmosis," *Desalination,* vol. 455, pp. 100-114, 2019.

[15] S. K. Patel, M. Qin, W. S. Walker, and M. Elimelech, "Energy Efficiency of Electro-Driven Brackish Water Desalination: Electrodialysis Significantly Outperforms Membrane Capacitive Deionization," *Environmental Science & Technology,* vol. 54, no. 6, pp. 3663-3677, 2020.

[16] S. Porada, L. Zhang, and J. Dykstra, "Energy consumption in membrane capacitive deionization and comparison with reverse osmosis," *Desalination,* vol. 488, p. 114383, 2020.

[17] C. Tan, C. He, W. Tang, P. Kovalsky, J. Fletcher, and T. D. Waite, "Integration of photovoltaic energy supply with membrane capacitive deionization (MCDI) for salt removal from brackish waters," *Water Res.,* vol. 147, pp. 276-286, 2018.

[18] J. Kang, T. Kim, K. Jo, and J. Yoon, "Comparison of salt adsorption capacity and energy consumption between constant current and constant voltage operation in capacitive deionization," *Desalination,* vol. 352, pp. 52-57, 2014.

[19] J.-H. Choi, "Comparison of constant voltage (CV) and constant current (CC) operation in the membrane capacitive deionisation process," *Desalination and Water Treatment,* vol. 56, no. 4, pp. 921-928, 2015.

[20] Y. Qu, P. G. Campbell, L. Gu, J. M. Knipe, E. Dzenitis, J. G. Santiago, and M. Stadermann, "Energy consumption analysis of constant voltage and constant current operations in capacitive deionization," *Desalination,* vol. 400, pp. 18-24, 2016.

[21] L. Wang and S. Lin, "Membrane capacitive deionization with constant current vs constant voltage charging: which is better?," *Environmental science & technology,* vol. 52, no. 7, pp. 4051-4060, 2018.

[22] L. Han, K. Karthikeyan, and K. B. Gregory, "Energy consumption and recovery in capacitive deionization using nanoporous activated carbon electrodes," *Journal of The Electrochemical Society,* vol. 162, no. 12, pp. E282-E288, 2015.

[23] P. Długołęcki and A. van der Wal, "Energy recovery in membrane capacitive deionization," *Environmental science & technology,* vol. 47, no. 9, pp. 4904-4910, 2013.

[24] J. Dykstra, R. Zhao, P. Biesheuvel, and A. Van der Wal, "Resistance identification and rational process design in capacitive deionization," *Water Res.,* vol. 88, pp. 358-370, 2016.

[25] V. M. Palakkal, J. E. Rubio, Y. J. Lin, and C. G. Arges, "Low-resistant ion-exchange membranes for energy efficient membrane capacitive deionization," *ACS Sustainable Chemistry & Engineering,* vol. 6, no. 11, pp. 13778-13786, 2018.

[26] J. Shim, N. Yoon, S. Park, J. Park, M. Son, K. Jeong, and K. H. Cho, "Influence of Natural Organic Matter on Membrane Capacitive Deionization Performance," *Chemosphere,* p. 128519, 2020.

[27] E. García-Quismondo, C. Santos, J. Lado, J. Palma, and M. A. Anderson, "Optimizing the energy efficiency of capacitive deionization reactors working under real-world conditions," *Environmental science & technology,* vol. 47, no. 20, pp. 11866-11872, 2013.

[28] E. García-Quismondo, C. Santos, J. Soria, J. s. Palma, and M. A. Anderson, "New operational modes to increase energy efficiency in capacitive deionization systems," *Environmental science & technology,* vol. 50, no. 11, pp. 6053-6060, 2016.

[29] L. Wang, J. Dykstra, and S. Lin, "Energy efficiency of capacitive deionization," *Environmental science & technology,* vol. 53, no. 7, pp. 3366-3378, 2019.

[30] A. Hemmatifar, A. Ramachandran, K. Liu, D. I. Oyarzun, M. Z. Bazant, and J. G. Santiago, "Thermodynamics of ion separation by electrosorption," *Environmental science & technology,* vol. 52, no. 17, pp. 10196-10204, 2018.

[31] Y.-W. Chen, J.-F. Chen, C.-H. Lin, and C.-H. Hou, "Integrating a supercapacitor with capacitive deionization for direct energy recovery from the desalination of brackish water," *Applied Energy,* vol. 252, p. 113417, 2019.

[32] C. Tan, C. He, J. Fletcher, and T. D. Waite, "Energy recovery in pilot scale membrane CDI treatment of brackish waters," *Water Res.,* vol. 168, p. 115146, 2020.

[33] O. N. Demirer, R. M. Naylor, C. A. R. Perez, E. Wilkes, and C. Hidrovo, "Energetic performance optimization of a capacitive deionization system operating with transient cycles and brackish water," *Desalination,* vol. 314, pp. 130-138, 2013.

[34] X. Zhang and D. Reible, "Exploring the Function of Ion-Exchange Membrane in Membrane Capacitive Deionization via a Fully Coupled Two-Dimensional Process Model," *Processes,* vol. 8, no. 10, p. 1312, 2020.

[35] Y. Salamat and C. H. Hidrovo, "A parametric study of multiscale transport phenomena and performance characteristics of capacitive deionization systems," *Desalination,* vol. 438, pp. 24-36, 2018.

[36] K. Laxman, A. Husain, A. Nasser, M. Al Abri, and J. Dutta, "Tailoring the pressure drop and fluid distribution of a capacitive deionization device," *Desalination,* vol. 449, pp. 111-117, 2019.

[37] N. Nishiyama and T. Yokoyama, "Permeability of porous media: role of the critical pore size," *Journal of Geophysical Research: Solid Earth,* vol. 122, no. 9, pp. 6955-6971, 2017.

[38] E. N. Guyes, A. Simanovski, and M. E. Suss, "Several orders of magnitude increase in the hydraulic permeability of flow-through capacitive deionization electrodes via laser perforations," *RSC advances,* vol. 7, no. 34, pp. 21308-21313, 2017.

[39] Y. Salamat and C. H. Hidrovo, "Significance of the micropores electro-sorption resistance in capacitive deionization systems," *Water Res.,* vol. 169, p. 115286, 2020.

[40] Y. Qu, T. F. Baumann, J. G. Santiago, and M. Stadermann, "Characterization of resistances of a capacitive deionization system," *Environmental science & technology,* vol. 49, no. 16, pp. 9699-9706, 2015.

[41] A. Hemmatifar, M. Stadermann, and J. G. Santiago, "Two-dimensional porous electrode model for capacitive deionization," *The Journal of Physical Chemistry C,* vol. 119, no. 44, pp. 24681-24694, 2015.

[42] P. Sharma and T. Bhatti, "A review on electrochemical double-layer capacitors," *Energy conversion and management,* vol. 51, no. 12, pp. 2901-2912, 2010.

[43] J. Bear, *Dynamics of fluids in porous media*. Courier Corporation, 2013.

[44] R. Millington and J. Quirk, "Permeability of porous solids," *Transactions of the Faraday Society,* vol. 57, pp. 1200-1207, 1961.

[45] G. W. Jackson and D. F. James, "The permeability of fibrous porous media," *The Canadian Journal of Chemical Engineering,* vol. 64, no. 3, pp. 364-374, 1986.

[46] A. Nabovati, E. W. Llewellin, and A. C. Sousa, "A general model for the permeability of fibrous porous media based on fluid flow simulations using the lattice Boltzmann method," *Composites Part A: Applied Science and Manufacturing,* vol. 40, no. 6-7, pp. 860-869, 2009.

[47] P. Biesheuvel, "Thermodynamic cycle analysis for capacitive deionization," *Journal of colloid and interface science,* vol. 332, no. 1, pp. 258-264, 2009.

[48] L. Wang and S. Lin, "Intrinsic tradeoff between kinetic and energetic efficiencies in membrane capacitive deionization," *Water research,* vol. 129, pp. 394-401, 2018.

[49] C. Zhang, D. He, J. Ma, W. Tang, and T. D. Waite, "Faradaic reactions in capacitive deionization (CDI)-problems and possibilities: A review," *Water research,* vol. 128, pp. 314-330, 2018.

CHAPTER 5

THEORETICAL ANALYSIS OF CONSTANT VOLTAGE MODE MEMBRANE CAPACITIVE DEIONIZATION FOR WATER SOFTENING[4]

5.1. Abstract

Water softening is desirable to reduce scaling in water infrastructure and to meet industrial water quality needs and consumer preferences. Membrane capacitive deionization (MCDI) can preferentially adsorb divalent ions including calcium and magnesium and thus may be an attractive water softening technology. In this work, a process model incorporating ion exclusion effects was applied to investigate water softening performance including ion selectivity, ion removal efficiency and energy consumption in a constant voltage (CV) mode MCDI. Trade-offs between the simulated Ca^{2+} selectivity and Ca^{2+} removal efficiency under varying applied voltage and varying initial concentration ratio of Na^{+} to Ca^{2+} were observed. A cut-off CV mode, which was operated to maximize Ca^{2+} removal efficiency per cycle, was found to lead to a specific energy consumption (SEC) of 0.061 kWh/mole removed Ca^{2+} for partially softening industrial water, and 0.077 kWh/m^3 removed Ca^{2+} for slightly softening tap water at a water recovery of 0.5. This is an order of magnitude less than reported values for other softening techniques. MCDI should be explored more fully as an energy efficient means of water softening.

[4] This chapter is reproduced from the paper published as: Zhang, Xin, and Reible, Danny. "Theoretical Analysis of Constant Voltage Mode Membrane Capacitive Deionization for Water Softening." Membranes 11.4 (2021): 231.

5.2. Introduction

The majority of natural waters contain a certain amount of hardness (i.e. divalent ions, primarily calcium and magnesium), causing potential fouling, scaling and taste issues. Excess intake of calcium and magnesium inhibits the adsorption of other essential elements and may cause diarrhea, while inadequate uptake of either calcium or magnesium also poses health threats [1]. Removal of hardness is common in waters for industrial, agricultural and domestic use.

Traditional techniques used for softening hard waters include ion-exchange [2], chemical and electrochemical precipitation [3, 4], nanofiltration [5, 6] and electro-membrane processes [7]. Capacitive deionization (CDI) removes charged particles in solution by attracting them toward the oppositely charged porous electrodes and temporarily holding them in the electric double layer (EDL) formed near the electrodes' surface [8, 9]. CDI is applicable to water softening due to the preferential electrosorption of divalent hardness ions over monovalent ions [10, 11], and the technology has been investigated for softening brackish waters [12-18].

Membrane CDI (MCDI) inserts ion-exchange membrane (IEM) between the electrodes and porous spacer to enhance desalination performance and improve energy efficiency [19]. Specifically, a cation-exchange membrane (CEM) is assembled onto the cathode and an anion-exchange membrane (AEM) is assembled onto the anode. IEM facilitates counter-ions' transport but inhibits co-ions' penetration. IEM improves ion transport rate and increases the flux of hardness ions over that of sodium ions, enabling a faster

and more efficient water softening in MCDI compared to conventional CDI [20]. Fouling and scaling issues are largely alleviated in MCDI compared to conventional CDI and other desalination techniques due to the protection of the IEM and the reversed ion transport direction during regeneration [21, 22].

MCDI water softening performance is determined by feed water chemistry, hydrated ion radius, ion valence, electrode and IEM construction and materials, operating modes and operating conditions [15, 16, 23, 24]. Hou and Huang [15] observed preferential adsorption of ions with smaller hydrated ion radius, larger charge valence and higher initial concentration in a batch mode CDI. IEM selective permeation toward specific ions is governed by the affinity of IEM toward the ions, ion concentration outside the IEM and ion mobility inside the IEM, and can be enhanced by membrane surface modification [25]. Specific IEM modifications such as replacing CEM with Ca-alginate [16] and coating polyelectrolyte multilayers onto the CEM [24] have been employed to tune ion selectivity in MCDI. He et al. [23] observed that selectivity of calcium ions was enhanced under lower applied current and shorter hydraulic retention time in a flow-electrode CDI.

Substitution of monovalent ions (e.g. sodium) by divalent ions has been observed near adsorption saturation of the electrode in constant voltage (CV) mode CDI [13, 14, 26]. Zhao et al. [14] explained this selectivity using the Boltzmann distribution to indicate that close to saturation, the accumulated potential in EDL becomes significant and ion selectivity is dominated by valence. Ion selectivity in a constant current (CC) mode, however, depends more on the ion transport through cell elements since electrode

saturation is not reached in CC mode. Wang and Lin [20] observed a correlation between ion selectivity and ion flux through the IEM in CC mode MCDI resulting from differences in partition coefficient, effective diffusion coefficient and ion concentration.

A number of process models have been developed for depicting dynamic ion transport and adsorption in (M)CDI but all to-date have been limited to treating ions as point charges [20, 27-32]. Yet treating ions as point charges is unable to capture excluded ion volume effects [33], limiting the ability to simulate ion adsorption and selectivity in multicomponent solutions containing ions with different hydration radii. Suss [34] introduced an excess chemical potential term into the modified Donnan theory to correct ion concentration in macropores and micropores for the available volume (pore volume minus the excluded volume of each ion that are inaccessible to other ions). Guyes et al. [35] employed Suss's theory and incorporated the effects of the attached surface charges on the electrode, successfully capturing the experimentally observed preferential adsorption toward the smaller ions in a batch mode CDI using functionalized electrode.

Trade-offs between calcium selectivity and calcium removal efficiency were discovered in CC mode MCDI [20]. However, hardness removal efficiency is a more important performance metric in water softening. CV mode MCDI was observed to reach high salt removal efficiency by reversing electrode polarity at maximum salt removal efficiency (termed here as "cut-off" mode) [32]. In this work, water softening performance of a CV mode MCDI is theoretically explored by investigating the selectivity and removal efficiency of hardness ions and the energy behaviors. The objectives of this work are to 1) extend our previously built MCDI process model [32] to incorporate excluded ion

volume effects and compare the respective simulation results to those achieved with the original model, 2) compare selectivity and removal efficiency of hardness ion under varying operating duration, 3) explore the trade-offs between selectivity and removal efficiency of hardness ions in a cut-off CV mode MCDI, and 4) analyze the cell performance, energy consumption and feasibility of applying MCDI to soften waters of various purposes, including industrial cooling tower blowdown water and domestic tap water.

5.3. Model framework

Our model is based on a single-pass CV mode MCDI with flow direction in parallel with the electrodes [32]. Common components in brackish waters, including the divalent ions typically responsible for hardness, calcium and magnesium, their reported hydrated radii [36] and diffusion coefficients [37] are displayed in Table 5.1.

Table 5.1. Common components in brackish waters and their hydrated radii and diffusion coefficients

Components	**Hydrated radii, (nm)** [36]	**Diffusion coefficients, (m^2/s)** [37]
Na^+	0.358	1.33×10^{-9}
K^+	0.331	1.96×10^{-9}
Ca^{2+}	0.412	0.79×10^{-9}
Mg^{2+}	0.428	0.71×10^{-9}
Cl^-	0.332	2.03×10^{-9}
NO_3^-	0.335	1.90×10^{-9}
SO_4^{2-}	0.379	1.07×10^{-9}

The basic modeling approach is described in [32]. Here we focus on the modifications necessary to include excluded ion volume effects. We employ a modification to Donnan theory considering an excess chemical potential difference term [34]:

$$c_{mi,i} = c_{ma,i} exp(-\frac{z_i F \varphi_d}{RT} - \Delta\mu_i^{ex}) \tag{5.1}$$

where $c_{mi,i}$ is the concentration of species i in micropores, $c_{ma,i}$ is the concentration of species i in macropores, z_i is the ion valence of species i, F is the Faraday's constant (96485 C/mol), φ_d is the Donnan potential of micropores, R is the universal gas constant (8.314 J/mol/K), T is the ambient temperature, and $\Delta\mu_i^{ex}$ is the difference of the excess chemical potentials in micropores and the adjacent macropores:

$$\Delta\mu_i^{ex} = \mu_{mi,i}^{ex} - \mu_{ma,i}^{ex} \tag{5.2}$$

where $\mu_{mi,i}^{ex}$ and $\mu_{ma,i}^{ex}$ are the excess chemical potentials in micropores and the adjacent macropores, respectively, accounting for ion exclusion effects.

For a multi-component system containing the assumed hard-sphere ions with different hydrated ion radii, the excess chemical potential can be analytically expressed by Boublik-Mansoori-Carnahan-Starling-Leland (BMCSL) equation [34]:

$$\mu_{j,i}^{ex} = -\left(1 + \frac{2\xi_2^3 d_i^3}{\phi^3} - \frac{3\xi_2^2 d_i^2}{\phi^2}\right)\ln(1-\phi) + \frac{3\xi_2 d_i + 3\xi_1 d_i^2 + \xi_0 d_i^3}{1-\phi} + \frac{3\xi_2 d_i^2}{(1-\phi)^2}\left(\frac{\xi_2}{\phi} + \xi_1 d_i\right) - \xi_2^3 d_i^3 \frac{\phi^2 - 5\phi + 2}{\phi^2(1-\phi)^3} \tag{5.3}$$

where j represents *mi* and *ma*, and d_i is the hard-sphere diameter of species i, which is correlated to the reported hydrated ion diameter $d_{h,i}$ with an adjustable constant C to fit the experimental data.

$$d_i = C \cdot d_{h,i} \tag{5.4}$$

ϕ is the volume fraction of all the ions:

$$\phi = \sum_i \phi_i = \sum_i \frac{\pi d_i^3}{6} c_{j,i} N_a \tag{5.5}$$

where $c_{j,i}$ is the concentration of species i in location j, macropores or micropores, and N_a is the Avogadro's constant (6.022×10^{23} mol^{-1}).

ξ_k is expressed by:

$$\xi_k = \sum_i \phi_i d_i^{k-3} \tag{5.6}$$

External resistance effects are included in the model with the relation:

$$V_{cell} = V_e + I_{ext} R_{ext} \tag{5.7}$$

where V_{cell} is the applied voltage, V_e is the electric potential drop on the electrode pair, R_{ext} is the external resistance, and I_{ext} is the external current [27].

In this study, MCDI is assumed symmetric with identical cathode and anode, and identical CEM and AEM. Detailed MCDI device parameters and operating conditions based on a single cell unit are listed in Table 5.2. The parameters marked with * and # are only used in the example of industrial cooling tower blowdown water softening (Section 5.4.3.1) and domestic tap water softening (Section 5.4.3.2).

Table 5.2. MCDI device parameters and operating conditions based on a single cell unit

Parameter	Value	Unit
Cell length	10	[cm]
Cell width	10	[cm]
Electrode thickness	0.15	[mm]
Macropore porosity	0.4 [27]	-
Micropore porosity	0.3 [27]	-
Micropore capacitance	1.5 [27]	[GF/m^3]
IEM thickness	0.15	[mm]
IEM water content volume fraction	0.4	[L(water) / L(swollen IEM)]
IEM fixed charge density	1000	[mol/m^3]
Spacer-filled channel thickness	0.3	[mm]
Spacer porosity	0.71	-
Spacer permeability	1.23×10^{-12}	[m^2]
External resistance	0.6	[Ω]
Adjustable variable *C*	1.15-1.35, 1.25*#[34]	-
Flow rate	0.3, 0.35*, 0.2#	[L/h]
Applied voltage	0.1-0.3, 0.4*, 0.08#	[V]

*: Parameters used in industrial cooling tower blowdown water softening example, Section 5.4.3.1.
#: Parameters used in residential tap water softening example, Section 5.4.3.2.

5.4. Results and discussions

5.4.1. Ion excluded volume effects

In a multicomponent saline solution, selectivity of cationic species *i* is usually defined as the ratio of the removal efficiency of the cationic species *i* to that of sodium ions [20]:

$$S\left(\frac{i}{Na^+}\right) = \frac{\Delta c_i / c_{0,i}}{\Delta c_{Na^+} / c_{0,Na^+}} = \frac{\eta_i}{\eta_{Na^+}} \tag{5.8}$$

where $S(i/Na^+)$ is the selectivity of the cationic species i, $c_{0,i}$ is the initial concentration of the cationic species i, c_{0,Na^+} is the initial concentration of sodium ions, Δc_i is the concentration reduction of the cationic species i during desalination, Δc_{Na^+} is the concentration reduction of sodium ions during desalination, η_i is the removal efficiency of the cationic species i, and η_{Na^+} is the removal efficiency of sodium ions. Ion selectivity in (M)CDI is calculated based on the simulated effluent concentration with and without considering ion excluded volume effects by setting an inlet concentration of 20 mol/m^3 for all cations. The respective transient selectivity curves of K^+ and Ca^{2+} are displayed in Figure 5.1.

In order to verify this extended process model, transient K^+ selectivity in K^+-Na^+-Cl^- solution in CDI considering excluded ion volume effects is compared with that of ignoring ion excluded volume effects in Figure 5.1 (a). The use of these monovalent ions in this analysis allows us to explore only the effects of ionic radii separate from valence.

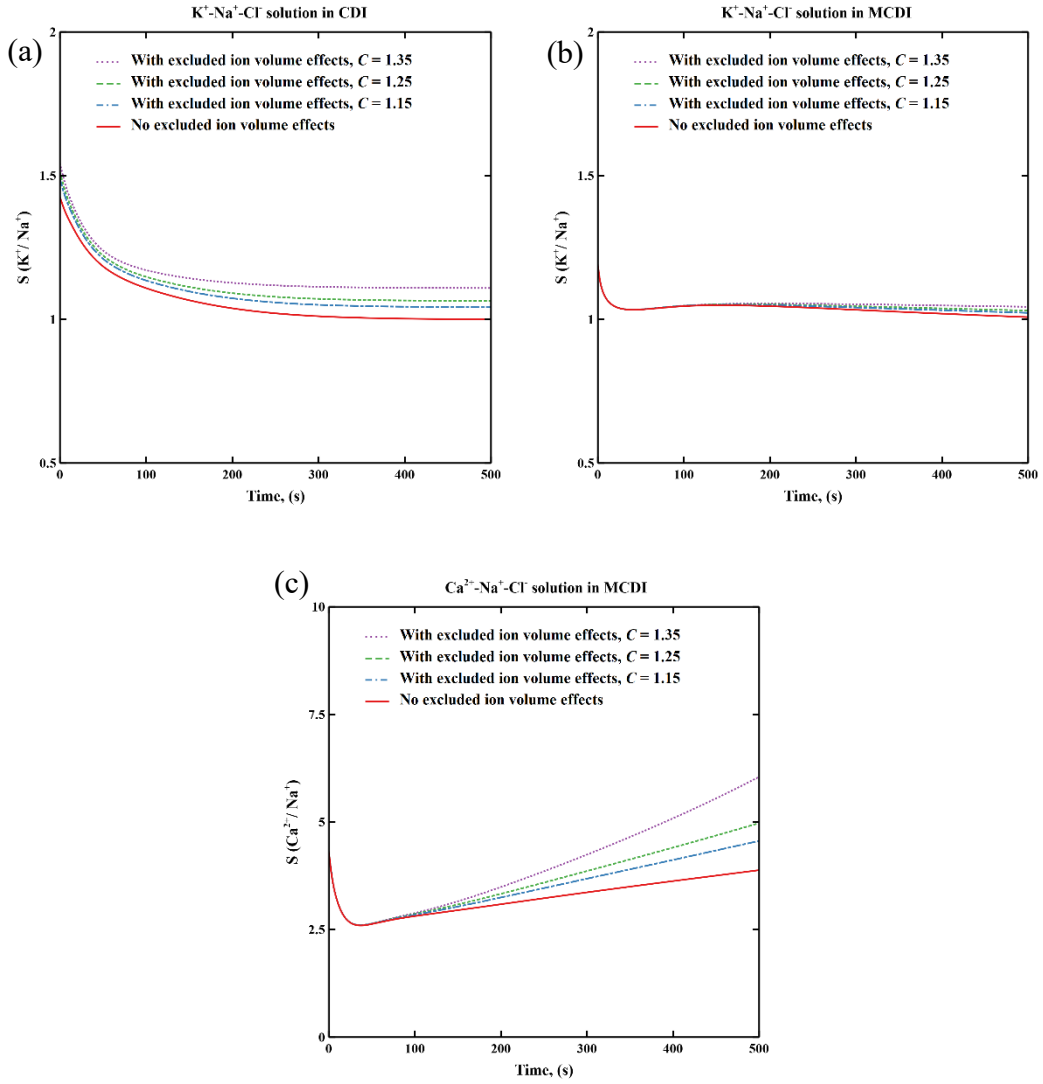

Figure 5.1. Transient K^+ selectivity in K^+-Na^+-Cl^- solution with and without considering excluded ion volume effects during desalination in (a) CDI and (b) MCDI. (c) Transient Ca^{2+} selectivity in Ca^{2+}-Na^+-Cl^- solution with and without considering ion excluded volume effects during desalination in MCDI. Adjustable variable C is varied from 1.15 to 1.35. Applied voltage is 0.3 V. Feed concentration of each cation is 20 mol/m^3.

As shown in Figure 5.1 (a), excluded ion volume effects slightly increases K^+ selectivity. At the beginning of charging, K^+ selectivity is higher than 1, which is attributed to the higher diffusivity of K^+ compared to Na^+. When electrode saturation is

reached (times greater than 300 seconds in this simulation), macropore concentration becomes uniform and identical to feed water concentration and selectivity in the absence of excluded ion volume effects approaches unity. With excluded ion volume effects, the smaller hydrated ion size of K^+ increases adsorption of K^+ and leads to a selectivity greater than 1 at equilibrium. The respective K^+ selectivity curves indicate that this extended process model successfully captures excluded ion volume effects. The varying adjustable constant *C* (see Eq. 5.4) from 1.15 to 1.35 is within the range of *C* values determined from experimental observations [34].

Figure 5.1 (b) shows the transient K^+ selectivity in MCDI. Initially, K^+ selectivity in MCDI is lower compared to that in CDI since K^+ and Na^+ transport through the IEM are similar and the IEM controls transport (see Figure B.1 (c) and (d)). Excluded ion volume effects only appear after some time due to increased adsorption on the electrodes. After electrode saturation is reached (times greater than 250s, see Figure B.1 (c) and (d)), the K^+ selectivity decreases, which is caused by the slow ion penetration through the IEM due to the concentration gradient from electrode macropores to the bulk, causing a repulsion of all ions including K^+ and Na^+. Since K^+ is transported faster than Na^+, K^+ selectivity is reduced after electrode saturation.

Figure 5.1 (c) shows that the selectivity toward the divalent ion Ca^{2+} is significantly greater than for the monovalent species and that excluded ion volume effects can approximately increase selectivity by 50% over that estimated by neglecting those affects. Ca^{2+} selectivity is much higher compared to K^+ selectivity and continues increasing even after the electrode saturation is achieved (times greater than 200s, see

Figure B.1 (e) and (f)). The increase of Ca^{2+} selectivity after electrode saturation is due to the competitive substitution of Na^{+} by Ca^{2+}, which was also observed by Zhao et al. [14].

5.4.2. Trade-offs between selectivity and removal efficiency of calcium ions

Figure 5.2 shows transient Ca^{2+} selectivity and removal efficiency in a Ca^{2+}-Na^{+}-Cl^{-} solution in MCDI. The trend in Ca^{2+} selectivity is almost opposite to that of Ca^{2+} removal efficiency, indicating a trade-off between selectivity and removal efficiency of Ca^{2+} during desalination. This trade-off was also observed in CC mode MCDI [20]. Although Ca^{2+} selectivity is enhanced by extending desalination operation to near-electrode saturation, overall removal efficiency decreases. To maximize removal efficiency, we propose operating MCDI such that only partial electrode saturation is achieved, i.e. "cut-off" mode [32]. In a multicomponent solution containing Ca^{2+} as the major hardness ions, cut-off mode is defined by cycling MCDI at maximal Ca^{2+} removal efficiency per cycle.

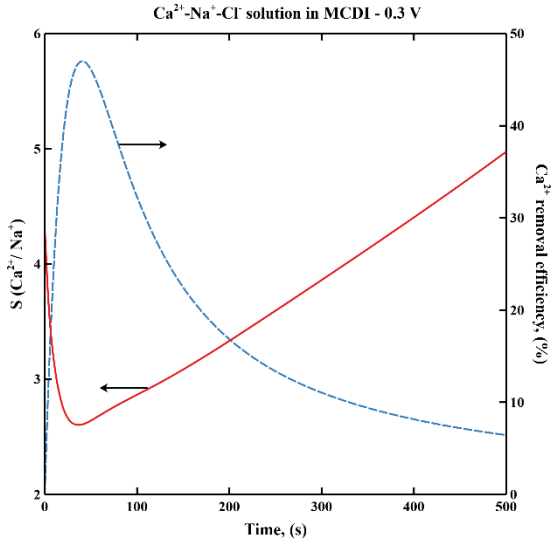

Figure 5.2. Transient Ca^{2+} selectivity and Ca^{2+} removal efficiency in Ca^{2+}-Na^{+}-Cl^{-} solution during desalination in MCDI. Feed concentration of each cation is 20 mol/m^3. Applied voltage is 0.3 V. Ratio of hard sphere diameter to hydraulic diameter, *C* is taken as 1.25.

Figure 5.3 shows the Ca^{2+} selectivity and removal efficiency in Ca^{2+}-Na^{+}-Cl^{-} solution during desalination in a cut-off mode MCDI under varying applied voltage and initial concentration ratios of cations. By increasing the applied voltage from 0.1 V to 0.3 V, Ca^{2+} selectivity decreases by 20%, while Ca^{2+} removal efficiency increases three-fold due to the increased adsorption capacity at the higher voltage (Figure 5.3 (a)). Selectivity for Ca^{2+} decreases with increasing feed ratio of Na^{+} to Ca^{2+} (Figure 5.3 (b)) but Ca^{2+} removal efficiency increases to over 80%.

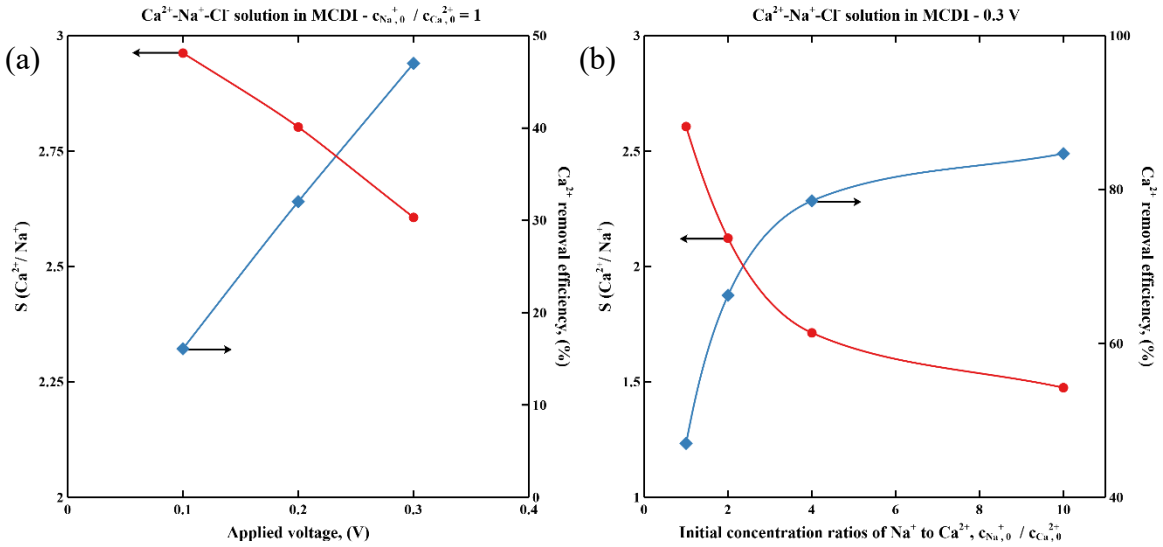

Figure 5.3. Simulated Ca^{2+} selectivity and Ca^{2+} removal efficiency in Ca^{2+}-Na^{+}-Cl^{-} solution during desalination in cut-off mode MCDI. (a) Feed concentration of each cation is 20 mol/m^3. Applied voltages are 0.1 V, 0.2 V, and 0.3 V, respectively; (b) Feed concentration of Na^{+} is 20 mol/m^3, while feed concentrations of Ca^{2+} are 20 mol/m^3, 10 mol/m^3, 5 mol/m^3 and 2 mol/m^3, respectively. Applied voltage is 0.3 V. Ratio of hard sphere diameter to hydraulic diameter, *C* is taken as 1.25.

5.4.3. Case studies

The feasibility of cut-off CV mode MCDI for softening waters is explored by examining water softening performance and energy consumption for two cases 1) industrial cooling tower blowdown water and 2) domestic tap water.

5.4.3.1 Industrial cooling tower blowdown water softening scenario

Electrochemical processes [38, 39] and pressure-driven membranes [40] have been applied to softening and recycling industrial cooling tower blowdown water to eliminate scaling and reduce the overall water usage. In this case study, the major ion compositions in the cooling tower blowdown water is from Ref. [41] as shown in Table

5.3. The MCDI is operated in cut-off CV mode with the salt adsorption step operated to achieve maximum salt removal. Water recovery is tuned by adjusting the operating time of the regeneration or desorption step. The operating conditions are shown in Table 5.2.

The simulated water softening performance including concentration of ionic species in product water, ion removal efficiency, Ca^{2+} selectivity, and specific energy consumption (SEC) of quasi-steady state MCDI are shown in Table 5.3. Here, SEC is based on unit cubic meter of product water and calculated as described in Section A.5 of the supporting information. In order to compare with the energy consumed by other water softening techniques, energy consumption per mole of removed Ca^{2+} is given by:

$$SEC_{mole} = \frac{SEC}{\Delta c_{Ca^{2+}}} \tag{5.9}$$

where $\Delta c_{Ca^{2+}}$ is the concentration reduction of Ca^{2+} in product water during desalination.

Table 5.3. Water softening performance and energy behaviors of quasi-steady state MCDI for partially softening industrial cooling tower blowdown water

Parameter		**Value**		
Concentration of ionic species in the feed water, (mM) [41]	Na^+	24.35		
	Ca^{2+}	7.48		
	Cl^-	14.95		
	NO_3^-	0.98		
	SO_4^{2-}	11.69		
		Water recovery		
		0.3	0.5	0.7
Concentration of ionic species in the product water, (mM)	Na^+	13.21	17.44	22.64
	Ca^{2+}	1.28	2.50	5.19
	Cl^-	9.23	11.53	14.19
	NO_3^-	0.62	0.76	0.93
	SO_4^{2-}	2.96	5.07	8.95
Ion removal efficiency, (%)	Na^+	45.76	28.37	7.03
	Ca^{2+}	82.88	66.64	30.62
	Cl^-	38.25	22.89	5.09
	NO_3^-	37.21	22.37	5.22
	SO_4^{2-}	74.68	56.61	23.43
Ca^{2+} selectivity		1.81	2.35	4.36
SEC, (kWh/m^3)		0.406	0.304	0.217
SEC_{mole}, (kWh/mole)		0.065	0.061	0.095

Quasi-steady state effluent concentration curves (see Figure B.4) are reached within five adsorption/desorption cycles. Under the same water recovery, the removal efficiency of divalent ion is higher than that of monovalent ion with selectivity shown in Table 5.3. As water recovery increases, overall removal efficiency of each ionic species decreases

due to incomplete desorption from the electrodes as a result of shortening of the regeneration/desorption time while Ca^{2+} selectivity increases. The increased product water causes SEC to decrease with increasing water recovery, while SEC_{mole} varies but can increase at high water recovery since short regeneration/desorption times are used at high water recoveries reducing Ca^{2+} removal. The SEC_{mole} values in this case study are an order of magnitude less than the reported values from other water softening techniques [39]. Overall, MCDI is energy efficient for partially softening industrial cooling tower blowdown water under moderate water recovery.

Figure 4 shows the major components of SEC including energy consumption of pump, external resistance, and cell pair, and the energy stored in EDL under fractional water recoveries of 0.3, 0.5 and 0.7.

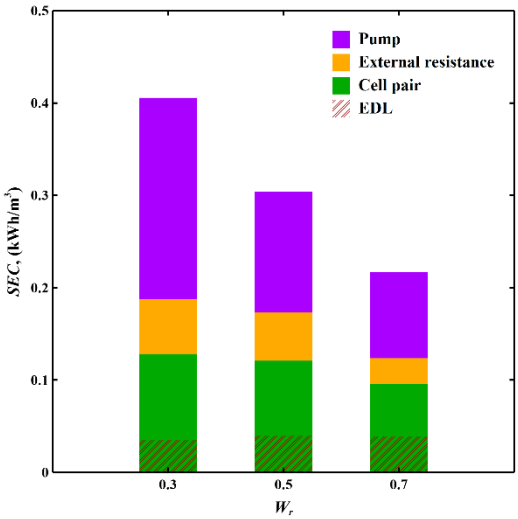

Figure 5.4. SEC with the contribution of each component including pump, external resistance, and cell pair and the energy stored in EDL with varying water recovery under quasi-steady state in cut-off CV mode MCDI for partially softening industrial cooling tower blowdown water. Flow rate is 0.35 L/hr. Applied voltage is 0.4 V.

Pump losses are the major energy losses, especially at low water recovery. Since water recovery is tuned by adjusting operating time of regeneration step, lower water recovery indicates longer regeneration and reduced water production, increasing relative pump energy consumption. External resistive losses account for 10-20% of the total energy consumption. The recoverable energy is not significantly affected by varying water recovery, so the recoverable energy as a proportion of the SEC increases with water recovery. In order to reduce SEC, permeability of the porous media spacer should be increased to reduce the pressure drop through the porous spacer-filled channel. Meanwhile, external resistance, especially contact resistance of MCDI elements, should be lowered to bring down the resistive losses.

5.4.3.2 Domestic tap water softening scenario

Softening domestic tap water helps address scaling issues and enhances the efficacy of soaps. Considering the relatively low hardness in tap water, slight softening is often sufficient and necessary to avoid corrosion [42]. In this case study, a cut-off CV mode MCDI is used for slightly softening domestic tap water with the major mineral compositions from Ref. [43] shown in Table 5.4. Anions in tap water are assumed to be Cl^-. Water recovery is also tuned by adjusting the operating time of regeneration while keeping the same flow rate for both desalination and regeneration steps. The operating conditions are shown in Table 5.2.

The simulated cell performance, such as concentration of ionic species in product water, ion removal efficiency, Ca^{2+} selectivity, Mg^{2+} selectivity, and SEC of quasi-steady state MCDI are shown in Table 5.4. Since a relatively high water recovery is often preferred for tap water treatment, water recovery is set to 0.5 and 0.7. SEC_{mole} is also based upon unit mole of Ca^{2+} removed.

Table 5.4. Water softening performance and energy behaviors of quasi-steady state MCDI for slightly softening domestic tap water

Parameter		**Value**	
Concentration of ionic species in the feed water, (mM) [43]	Na^+	1.65	
	Ca^{2+}	0.75	
	K^+	0.13	
	Mg^{2+}	0.38	
	Cl^-	4.04	
		Water recovery	
		0.5	0.7
Concentration of ionic species in the product water, (mM)	Na^+	1.44	1.58
	Ca^{2+}	0.53	0.66
	K^+	0.11	0.13
	Mg^{2+}	0.27	0.34
	Cl^-	3.16	3.71
Ion removal efficiency, (%)	Na^+	12.94	4.38
	Ca^{2+}	28.90	11.43
	K^+	12.80	1.63
	Mg^{2+}	28.58	10.78
	Cl^-	21.80	8.12
Ca^{2+} selectivity		2.23	2.61
Mg^{2+} selectivity		2.21	2.46
SEC, (kWh/m^3)		0.077	0.055
SEC_{mole}, (kWh/mole)		0.356	0.256

Under the same water recovery, Ca^{2+} removal efficiency and selectivity are slightly higher than those of Mg^{2+}. This is due to the dual effects of the higher feed concentration and smaller hydrated ion radius of Ca^{2+}. Increasing water recovery leads to an increase in the selectivity of both Ca^{2+} and Mg^{2+} and a decrease in SEC and SEC_{mole}, but reduces

the removal efficiencies of all ionic species because of incomplete regeneration of the electrodes. SEC is very low for tap water softening. The SEC values are an order of magnitude less than those reported in a tap water softening study via electrochemical process [42]. Hence, MCDI is energy efficient for slightly softening tap water under moderate water recovery.

Figure 5.5 shows the major components of SEC including energy consumption of pump, external resistance, and cell pair, and the energy stored in EDL under water recovery of 0.5 and 0.7.

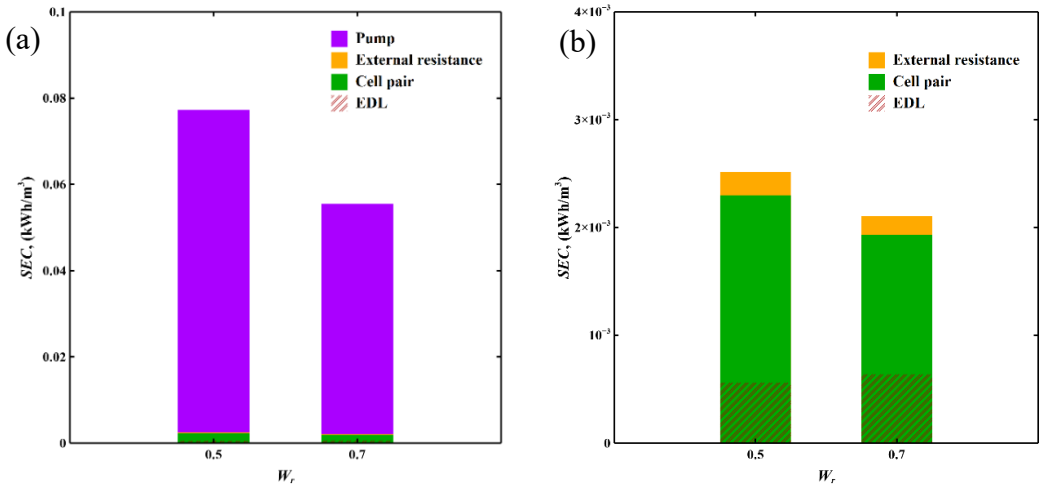

Figure 5.5. (a) SEC with the contribution of each component including pump, external resistance, and cell pair and the energy stored in EDL with varying water recovery under quasi-steady state in cut-off CV mode MCDI for slightly softening domestic tap water; (b) SEC without pump losses. Applied voltage is 0.08 V.

Although increasing water recovery shortens the operating time of regeneration and thus reduces pump losses, pump losses still account for 95% of the energy usage in these simulations although the permeability of the cell spacer can influence that amount.

External resistive losses are negligible due to the low external current during desalination, which is attributed to the low applied voltage together with the high resistance of tap water. The recoverable energy increases slightly with increasing water recovery, but is also negligible compared to the huge pump losses. Hence, when softening super low concentration solution such as tap water, reducing pump losses can significantly enhance energy efficiency.

5.5. Conclusion

In this work, our proposed two-dimensional MCDI process model was extended to incorporate excluded ion volume effects, making it possible to distinguish the adsorption behavior of equally charged ions with different hydrated ion radii as well as the selectivity toward divalent ions. Trade-offs between Ca^{2+} selectivity and Ca^{2+} removal efficiency were observed in a Ca^{2+}-Na^{+}-Cl^{-} solution under either varying applied voltage or varying initial concentration ratios of cations in a cut-off CV mode MCDI. This extended MCDI model was further applied to evaluating water softening performance of a cut-off CV mode MCDI for industrial cooling tower blowdown water and domestic tap water. The SEC of each case was an order of magnitude less than the reported values from other water softening techniques, indicating MCDI to be energy efficient for partially softening industrial waters and slightly softening tap waters under moderate water recovery. Pump losses become dominant for softening super low concentration solutions, such as tap water. Hence, improving the permeability of the porous spacer to reduce the hydraulic pressure drop can reduce the pump energy and save a lot of energy. The proposed model can be applied to predicting water softening

performance for saline waters with low content of foulants. Pretreatment is required for waters with high content of foulants. The proposed model should be modified to incorporate the effects of Faradaic reactions to predict water softening performance under relatively high applied voltage.

5.6. References

[1] J. A. Cotruvo and J. Bartram, *Calcium and magnesium in drinking-water: public health significance*. World Health Organization, 2009.

[2] J. E. Greenleaf, J. c. Lin, and A. K. Sengupta, "Two novel applications of ion exchange fibers: Arsenic removal and chemical‐free softening of hard water," *Environmental Progress,* vol. 25, no. 4, pp. 300-311, 2006.

[3] L. K. Wang, D. A. Vaccari, Y. Li, and N. K. Shammas, "Chemical precipitation," in *Physicochemical treatment processes*: Springer, 2005, pp. 141-197.

[4] C. Gabrielli, G. Maurin, H. Francy-Chausson, P. Thery, T. Tran, and M. Tlili, "Electrochemical water softening: principle and application," *Desalination,* vol. 201, no. 1-3, pp. 150-163, 2006.

[5] S. Lee and C.-H. Lee, "Effect of operating conditions on CaSO4 scale formation mechanism in nanofiltration for water softening," *Water Research,* vol. 34, no. 15, pp. 3854-3866, 2000.

[6] A. Rahimpour, M. Jahanshahi, N. Mortazavian, S. S. Madaeni, and Y. Mansourpanah, "Preparation and characterization of asymmetric polyethersulfone and thin-film composite polyamide nanofiltration membranes for water softening," *Applied Surface Science,* vol. 256, no. 6, pp. 1657-1663, 2010.

[7] J.-S. Park, J.-H. Song, K.-H. Yeon, and S.-H. Moon, "Removal of hardness ions from tap water using electromembrane processes," *Desalination,* vol. 202, no. 1-3, pp. 1-8, 2007.

[8] M. A. Ahmed and S. Tewari, "Capacitive deionization: Processes, materials and state of the technology," *Journal of Electroanalytical Chemistry,* vol. 813, pp. 178-192, 2018.

[9] S. Honarparvar, X. Zhang, T. Chen, C. Na, and D. Reible, "Modeling technologies for desalination of brackish water—toward a sustainable water supply," *Current Opinion in Chemical Engineering,* vol. 26, pp. 104-111, 2019.

[10] J. Choi, P. Dorji, H. K. Shon, and S. Hong, "Applications of capacitive deionization: Desalination, softening, selective removal, and energy efficiency," *Desalination,* vol. 449, pp. 118-130, 2019.

[11] T. Luo, S. Abdu, and M. Wessling, "Selectivity of ion exchange membranes: A review," *Journal of membrane science,* vol. 555, pp. 429-454, 2018.

[12] K. C. Leonard, J. R. Genthe, J. L. Sanfilippo, W. A. Zeltner, and M. A. Anderson, "Synthesis and characterization of asymmetric electrochemical capacitive deionization materials using nanoporous silicon dioxide and magnesium doped aluminum oxide," *Electrochimica Acta,* vol. 54, no. 22, pp. 5286-5291, 2009.

[13] S.-J. Seo, H. Jeon, J. K. Lee, G.-Y. Kim, D. Park, H. Nojima, J. Lee, and S.-H. Moon, "Investigation on removal of hardness ions by capacitive deionization (CDI) for water softening applications," *Water research,* vol. 44, no. 7, pp. 2267-2275, 2010.

[14] R. Zhao, M. Van Soestbergen, H. Rijnaarts, A. Van der Wal, M. Bazant, and P. Biesheuvel, "Time-dependent ion selectivity in capacitive charging of porous electrodes," *Journal of colloid and interface science,* vol. 384, no. 1, pp. 38-44, 2012.

[15] C.-H. Hou and C.-Y. Huang, "A comparative study of electrosorption selectivity of ions by activated carbon electrodes in capacitive deionization," *Desalination,* vol. 314, pp. 124-129, 2013.

[16] H. Yoon, J. Lee, S.-R. Kim, J. Kang, S. Kim, C. Kim, and J. Yoon, "Capacitive deionization with Ca-alginate coated-carbon electrode for hardness control," *Desalination,* vol. 392, pp. 46-53, 2016.

[17] J. J. Lado, R. L. Zornitta, I. s. Vázquez Rodríguez, K. Malverdi Barcelos, and L. A. Ruotolo, "Sugarcane Biowaste-Derived Biochars as Capacitive Deionization Electrodes for Brackish Water Desalination and Water-Softening Applications," *ACS Sustainable Chemistry & Engineering,* vol. 7, no. 23, pp. 18992-19004, 2019.

[18] Z. Y. Leong and H. Y. Yang, "Capacitive Deionization of Divalent Cations for Water Softening Using Functionalized Carbon Electrodes," *ACS omega,* vol. 5, no. 5, pp. 2097-2106, 2020.

[19] P. Biesheuvel and A. Van der Wal, "Membrane capacitive deionization," *Journal of Membrane Science,* vol. 346, no. 2, pp. 256-262, 2010.

[20] L. Wang and S. Lin, "Mechanism of selective ion removal in membrane capacitive deionization for water softening," *Environmental science & technology,* vol. 53, no. 10, pp. 5797-5804, 2019.

[21] A. Hassanvand, G. Chen, P. Webley, and S. Kentish, "An investigation of the impact of fouling agents in capacitive and membrane capacitive deionisation," *Desalination,* vol. 457, pp. 96-102, 2019.

[22] B. Van Limpt and A. Van der Wal, "Water and chemical savings in cooling towers by using membrane capacitive deionization," *Desalination,* vol. 342, pp. 148-155, 2014.

[23] C. He, J. Ma, C. Zhang, J. Song, and T. D. Waite, "Short-circuited closed-cycle operation of flow-electrode CDI for brackish water softening," *Environmental science & technology,* vol. 52, no. 16, pp. 9350-9360, 2018.

[24] S. Sahin, J. E. Dykstra, H. Zuilhof, R. L. Zornitta, and L. C. de Smet, "Modification of Cation-Exchange Membranes with Polyelectrolyte Multilayers to Tune Ion Selectivity in Capacitive Deionization," *ACS applied materials & interfaces,* vol. 12, no. 31, pp. 34746-34754, 2020.

[25] T. Sata, T. Sata, and W. Yang, "Studies on cation-exchange membranes having permselectivity between cations in electrodialysis," *Journal of Membrane Science,* vol. 206, no. 1-2, pp. 31-60, 2002.

[26] J. J. Lado, R. E. Pérez-Roa, J. J. Wouters, M. I. Tejedor-Tejedor, C. Federspill, J. M. Ortiz, and M. A. Anderson, "Removal of nitrate by asymmetric capacitive deionization," *Separation and Purification Technology,* vol. 183, pp. 145-152, 2017.

[27] A. Hemmatifar, M. Stadermann, and J. G. Santiago, "Two-dimensional porous electrode model for capacitive deionization," *The Journal of Physical Chemistry C,* vol. 119, no. 44, pp. 24681-24694, 2015.

[28] A. Rommerskirchen, B. Ohs, K. A. Hepp, R. Femmer, and M. Wessling, "Modeling continuous flow-electrode capacitive deionization processes with ion-exchange membranes," *Journal of membrane science,* vol. 546, pp. 188-196, 2018.

[29] K. Singh, H. Bouwmeester, L. de Smet, M. Bazant, and P. Biesheuvel, "Theory of water desalination with intercalation materials," *Physical Review Applied,* vol. 9, no. 6, p. 064036, 2018.

[30] F. He, P. Biesheuvel, M. Z. Bazant, and T. A. Hatton, "Theory of water treatment by capacitive deionization with redox active porous electrodes," *Water Res.,* vol. 132, pp. 282-291, 2018.

[31] D. I. Oyarzun, A. Hemmatifar, J. W. Palko, M. Stadermann, and J. G. Santiago, "Ion selectivity in capacitive deionization with functionalized electrode: Theory and experimental validation," *Water research X,* vol. 1, p. 100008, 2018.

[32] X. Zhang and D. Reible, "Exploring the Function of Ion-Exchange Membrane in Membrane Capacitive Deionization via a Fully Coupled Two-Dimensional Process Model," *Processes,* vol. 8, no. 10, p. 1312, 2020.

[33] P. Biesheuvel and M. Van Soestbergen, "Counterion volume effects in mixed electrical double layers," *Journal of Colloid and Interface Science,* vol. 316, no. 2, pp. 490-499, 2007.

[34] M. E. Suss, "Size-based ion selectivity of micropore electric double layers in capacitive deionization electrodes," *Journal of The Electrochemical Society,* vol. 164, no. 9, p. E270, 2017.

[35] E. N. Guyes, T. Malka, and M. E. Suss, "Enhancing the ion-size-based selectivity of capacitive deionization electrodes," *Environmental science & technology,* vol. 53, no. 14, pp. 8447-8454, 2019.

[36] E. Nightingale Jr, "Phenomenological theory of ion solvation. Effective radii of hydrated ions," *The Journal of Physical Chemistry,* vol. 63, no. 9, pp. 1381-1387, 1959.

[37] P. Vanysek, "Ionic conductivity and diffusion at infinite dilution," *CRC handbook of chemistry and physics,* vol. 83, pp. 76-78, 2000.

[38] C. Zhang, J. Tang, G. Zhao, Y. Tang, J. Li, F. Li, H. Zhuang, J. Chen, H. Lin, and Y. Zhang, "Investigation on an electrochemical pilot equipment for water softening with an automatic descaling system: Parameter optimization and energy consumption analysis," *Journal of Cleaner Production,* vol. 276, p. 123178, 2020.

[39] J. Luan, L. Wang, W. Sun, X. Li, T. Zhu, Y. Zhou, H. Deng, S. Chen, S. He, and G. Liu, "Multi-meshes coupled cathodes enhanced performance of electrochemical water softening system," *Separation and Purification Technology,* vol. 217, pp. 128-136, 2019.

[40] S. J. Altman, R. P. Jensen, M. A. Cappelle, A. L. Sanchez, R. L. Everett, H. L. Anderson Jr, and L. K. McGrath, "Membrane treatment of side-stream cooling tower water for reduction of water usage," *Desalination,* vol. 285, pp. 177-183, 2012.

[41] T. V. Wagner, V. de Wilde, B. Willemsen, M. Mutaqin, G. Putri, J. Opdam, J. R. Parsons, H. H. Rijnaarts, P. de Voogt, and A. A. Langenhoff, "Pilot-scale hybrid constructed wetlands for the treatment of cooling tower water prior to its desalination and reuse," *Journal of Environmental Management,* vol. 271, p. 110972, 2020.

[42] P. Clauwaert, J. De Paepe, F. Jiang, B. Alonso-Fariñas, E. Vaiopoulou, A. Verliefde, and K. Rabaey, "Electrochemical tap water softening: A zero chemical input approach," *Water research,* vol. 169, p. 115263, 2020.

[43] K. Y. Patterson, P. R. Pehrsson, and C. R. Perry, "The mineral content of tap water in United States households," *Journal of food composition and analysis,* vol. 31, no. 1, pp. 46-50, 2013.

CHAPTER 6

CONCLUSION AND FUTURE WORK

In this work a fully coupled two-dimensional (M)CDI process model based upon mD theory and its extensions explores the desalination performance of CDI including salt removal rate, salt adsorption capacity, salt removal efficiency, and energy behavior including SEC and TEE in monovalent and multivalent systems. The model is used to explore various cell geometries and operating conditions and considers the effects of applied voltage, flow rate, water recovery and cell cycle mode. For multivalent system, this process model is extended to incorporate ion exclusion effects and is then employed to predict water softening performance such as selectivity and removal efficiency of hardness ions and SEC for low-salinity brackish water sources including industrial cooling tower blowdown water and domestic tap water.

6.1 Summary

In Chapter 1, cell assembly, cell architectures, operating modes, adsorption mechanisms, key developments of cell elements, merits and drawbacks of CDI and its variants are depicted. CDI charging mode and application scope are summarized. CDI performance indicators including desalination performance, fouling and scaling degree, and energy and cost performance are introduced. Various factors effective performance are reviewed including 1) desalination performance such as charge efficiency, adsorption capacity, average salt adsorption rate, and salt removal efficiency, 2) anti-

fouling and anti-scaling ability, and 3) energy consumption, energy recovery and cost efficiency.

In Chapter 2, a comprehensive CDI process model incorporating the published extensions of mD theory is introduced that is capable of describing the effects of the functional groups on electrode surface, pH, Faradaic reactions, and various CDI architectures. Other models (that have been used for CDI simulation) including isotherm and kinetic models, DL models, and equivalent circuit model are described and compared to mD theory based CDI models, which are revealed to capture electrosorption mechanisms and Faradaic reactions and possess the widest application scope, although the computation needs to be simplified. Equivalent circuit models can serve as alternatives for estimating energy behaviors in single salt solution.

In Chapter 3, a fully coupled two-dimension MCDI process model is applied to evaluating MCDI performance in the face of hydraulic dispersion in spacer-filled channel and co-ion penetration through the IEM. This quantitatively verified model reveals: 1) the desalination rate is almost doubled in MCDI compared to CDI, 2) adsorption capacity of MCDI is larger than CDI due to the extra adsorption in macropores, and 3) using IEM, increasing applied voltage, decreasing flow rate, prolonging electrode length and thickness, reducing dispersivity and channel thickness, and operating cell under cut-off mode can enhance salt removal efficiency.

In Chapter 4, the energy performance of CV mode MCDI under cut-off and equilibrium modes are evaluated via the process model built in Chapter 3. Salt removal efficiency

decreases with increasing water recovery under high water recovery range due to the incomplete desorption of electrode during regeneration. Cut-off mode operation, in which salt removal efficiency is maximized, achieves higher SEC and TEE compared to equilibrium mode. Pump losses are dominant in equilibrium mode especially with long cell length, while external resistive losses are dominant under high water recovery in cut-off mode. Energy stored in EDL during desalination accounts for 20-40% of the total SEC. TEE decreases with increasing water productivity, and is competitive to RO for desalination near-fresh water under high water recovery. Overall, CV mode MCDI is more energy efficient under moderate water recovery compared to CC mode MCDI.

In Chapter 5, the process model of Chapter 3 is extended to incorporate ion exclusion effects and used to simulate the ion selectivity of potassium in potassium-sodium-chloride solution. Trade-offs between ion selectivity and ion removal efficiency in cut-off CV mode MCDI under varying feed water concentration ratio of cations and varying applied voltage are evaluated. This extended process model is then employed to investigate the selectivity and removal efficiency of hardness ions and the respective energy consumption in multicomponent system. Overall, MCDI is feasible for partially softening industrial cooling tower blowdown water and slightly softening domestic tap water under moderate water recovery with a satisfactory energy consumption.

6.2 Future work

6.2.1 Faradaic reactions

Redox reactions, also known as Faradaic reactions, occur in CDI and become significant under relatively high applied voltage. Zhang et al. [1] summarized the mechanisms of three types of Faradaic reactions including anodic oxidation, cathodic reduction and Faradaic ion adsorption shown in Figure 6.1. Specifically, anodic oxidation involves carbon, chloride and water in anode, while cathodic reduction involves oxygen, carbon and heavy metals in cathode. The reversible Faradaic ion adsorption, however, largely contributes to the adsorption of specific ions by assembling intercalation electrodes in CDI [2].

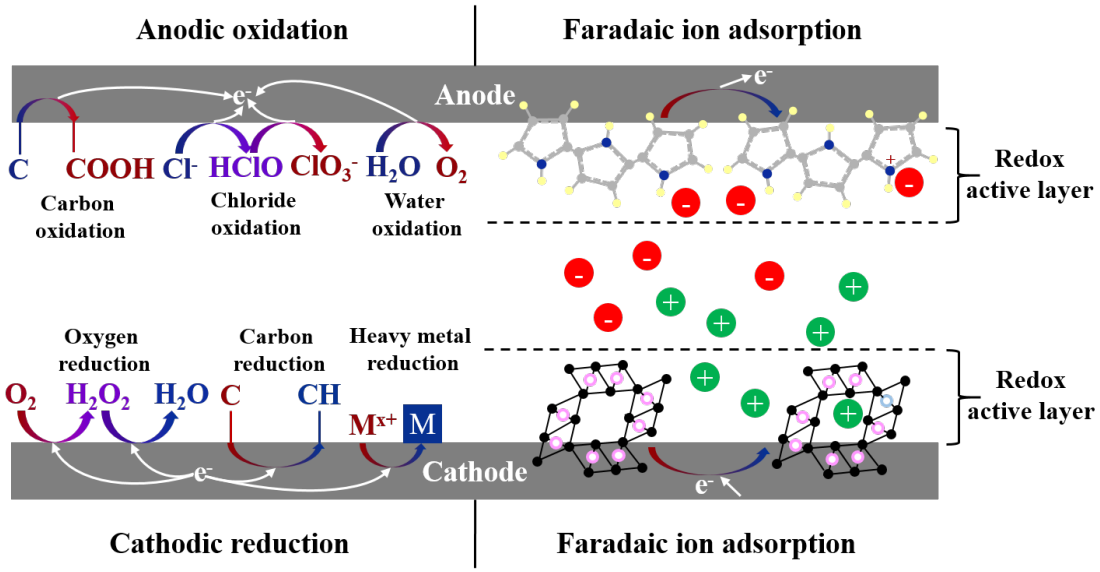

Figure 6.1. Schematic diagram of Faradaic reactions mechanisms in CDI [3].

The effects of Faradaic reactions and the respective changes of pH and chemical charge density on electrode surface have been incorporated into a few CDI models [4-7]. The current version of our fully coupled two-dimension MCDI process model does not incorporate Faradaic reactions considering the charging voltage in our study is within the safe range [1, 8-10]. However, incorporating Faradaic reactions is a necessity for determining the maximum adsorption capacity with high charging voltage. Faradaic adsorption via intercalation electrodes in CDI has been studied more in the past decade due to the enhanced adsorption capacity and high ion selectivity [11]. There is also a need to develop fully coupled two-dimensional process model for intercalation electrode assembled CDI. The Frumkin isotherm and its modifications can be employed to simulate ion adsorption in intercalation electrodes [12-14].

6.2.2 Electrode and cell architecture modifications

The electrode surface can be modified with functional groups to either enhance adsorption capacity and selectivity toward specific ions. To account for the extra chemical charges on electrode surface, chemical charge density can be incorporated into the micropore charge balance equation [15]. Our model can be extended to capture the extra chemical charges on electrode surface for simulating the enhanced cell performance and energy behaviors in CDI with functionalized electrodes. Our model can also be modified to simulate ion transport and adsorption dynamics of the recently developed alternative CDI architectures [11], which have improved the desalination performance and energy efficiency, and have broadened the application scope.

6.3 References

[1] C. Zhang, D. He, J. Ma, W. Tang, and T. D. Waite, "Faradaic reactions in capacitive deionization (CDI)-problems and possibilities: A review," *Water research,* vol. 128, pp. 314-330, 2018.

[2] K. Singh, S. Porada, H. De Gier, P. Biesheuvel, and L. De Smet, "Timeline on the application of intercalation materials in Capacitive Deionization," *Desalination,* vol. 455, pp. 115-134, 2019.

[3] S. Honarparvar, X. Zhang, T. Chen, A. Alborzi, K. Afroz, and D. Reible, "Frontiers of Membrane Desalination Processes for Brackish Water Treatment: A Review," *Membranes,* vol. 11, no. 4, p. 246, 2021.

[4] J. Dykstra, K. Keesman, P. Biesheuvel, and A. Van der Wal, "Theory of pH changes in water desalination by capacitive deionization," *Water research,* vol. 119, pp. 178-186, 2017.

[5] P. Biesheuvel, Y. Fu, and M. Bazant, "Electrochemistry and capacitive charging of porous electrodes in asymmetric multicomponent electrolytes," *Russian Journal of Electrochemistry,* vol. 48, no. 6, pp. 580-592, 2012.

[6] A. Hemmatifar, D. I. Oyarzun, J. W. Palko, S. A. Hawks, M. Stadermann, and J. G. Santiago, "Equilibria model for pH variations and ion adsorption in capacitive deionization electrodes," *Water research,* vol. 122, pp. 387-397, 2017.

[7] F. He, P. Biesheuvel, M. Z. Bazant, and T. A. Hatton, "Theory of water treatment by capacitive deionization with redox active porous electrodes," *Water Res.,* vol. 132, pp. 282-291, 2018.

[8] W. Tang, D. He, C. Zhang, P. Kovalsky, and T. D. Waite, "Comparison of Faradaic reactions in capacitive deionization (CDI) and membrane capacitive deionization (MCDI) water treatment processes," *Water Res.,* vol. 120, pp. 229-237, 2017.

[9] F. Yu, L. Wang, Y. Wang, X. Shen, Y. Cheng, and J. Ma, "Faradaic reactions in capacitive deionization for desalination and ion separation," *Journal of Materials Chemistry A,* vol. 7, no. 27, pp. 15999-16027, 2019.

[10] D. Lu, W. Cai, and Y. Wang, "Optimization of the voltage window for long-term capacitive deionization stability," *Desalination,* vol. 424, pp. 53-61, 2017.

[11] W. Tang, J. Liang, D. He, J. Gong, L. Tang, Z. Liu, D. Wang, and G. Zeng, "Various cell architectures of capacitive deionization: Recent advances and future trends," *Water Res.,* 2018.

[12] K. Singh, H. Bouwmeester, L. de Smet, M. Bazant, and P. Biesheuvel, "Theory of water desalination with intercalation materials," *Physical Review Applied,* vol. 9, no. 6, p. 064036, 2018.

[13] K. Singh, L. Zhang, H. Zuilhof, and L. de Smet, "Water desalination with nickel hexacyanoferrate electrodes in capacitive deionization: Experiment, model and comparison with carbon," *Desalination,* vol. 496, p. 114647, 2020.

[14] J. Gamaethiralalage, K. Singh, S. Sahin, J. Yoon, M. Elimelech, M. Suss, P. Liang, P. Biesheuvel, R. Zornitta, and L. de Smet, "Recent advances in ion selectivity with capacitive deionization," *Energy & Environmental Science,* 2021.

[15] P. Biesheuvel, H. Hamelers, and M. Suss, "Theory of water desalination by porous electrodes with immobile chemical charge," *Colloids and Interface Science Communications,* vol. 9, pp. 1-5, 2015.

APPENDIX A

SUPPORTING INFORMATION FOR CHAPTER 4

A.1 Transient effluent concentration curves of MCDI in five consecutive cycles

Transient effluent concentrations, C_{out}, of five consecutive cycles in both cut-off mode and equilibrium mode with water recovery fraction from 0.5 to 0.9 are shown in Figure A.1. Desalination and regeneration processes are not symmetric, especially with high water recovery. With water recovery fraction higher than 0.5, flow rate in regeneration step is lower compared to that of desalination step, which slows down the desorption process and results in incomplete desorption of the electrode. However, the prolonged residence time leads to a higher value of the maximum effluent concentration during regeneration. Dynamic steady state is achieved within five cycles, which is marked by the repeatable transient effluent concentration curves.

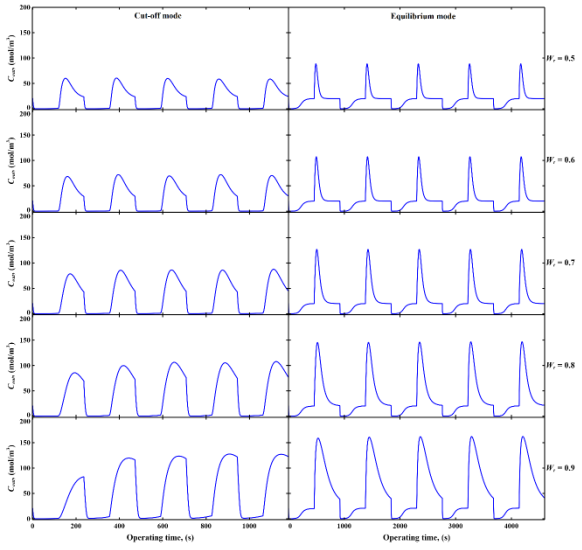

Figure A.1. Transient effluent concentration curves in both cut-off mode and equilibrium mode with water recovery of 0.5, 0.6, 0.7, 0.8, and 0.9. Applied voltage is 0.8 V, and cell length is 10 cm.

A.2 Transient electrochemical properties of MCDI in dynamic steady state

Transient external current curves in desalination step of the fifth cycle in both cut-off and equilibrium modes with varying water recovery fraction from 0.5 to 0.9 are displayed in Figure A.2.

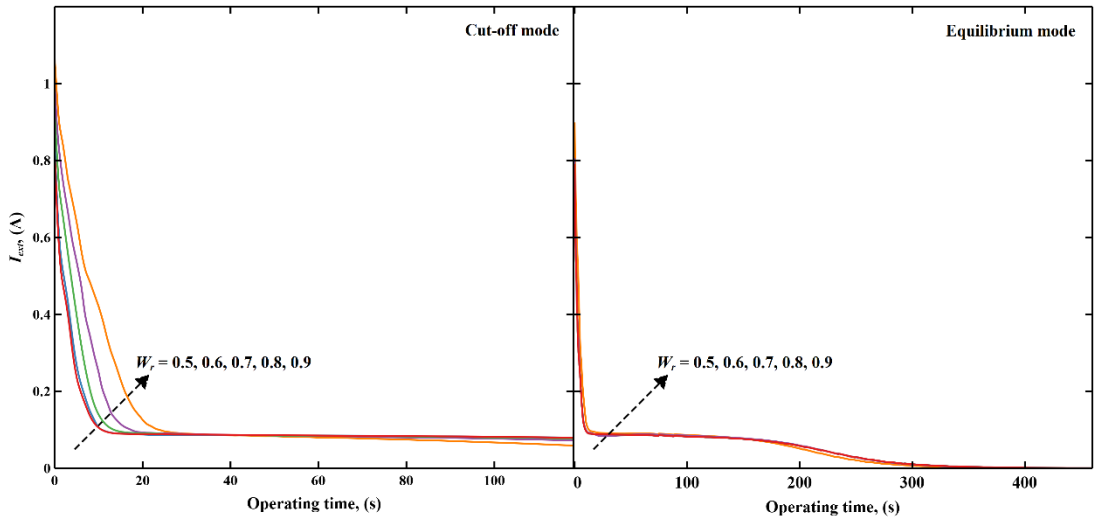

Figure A.2. Transient external current curves in desalination step of the fifth cycle in both cut-off mode and equilibrium mode with water recovery of 0.5, 0.6, 0.7, 0.8, and 0.9. Applied voltage is 0.8 V, and cell length is 10 cm.

External current drops sharply first and then slowly decreases until adsorption saturation is reached. External current increases with increasing water recovery at the beginning of desalination in cut-off mode. This is in accord with the relatively high concentration at the beginning of desalination at high water recovery, which is caused by the intensified incomplete desorption of the electrode in the previous regeneration step.

There're no significant deviations of transient external current curves under varying water recovery in equilibrium mode.

Transient Stern layer potential drop (φ_{St}) and Donnan potential (φ_D) of one electrode, and the accumulated potential in EDL of both electrodes (ΔV) in desalination step of the fifth cycle in both cut-off and equilibrium modes with varying water recovery from 0.5 to 0.9 are displayed in Figure A.3.

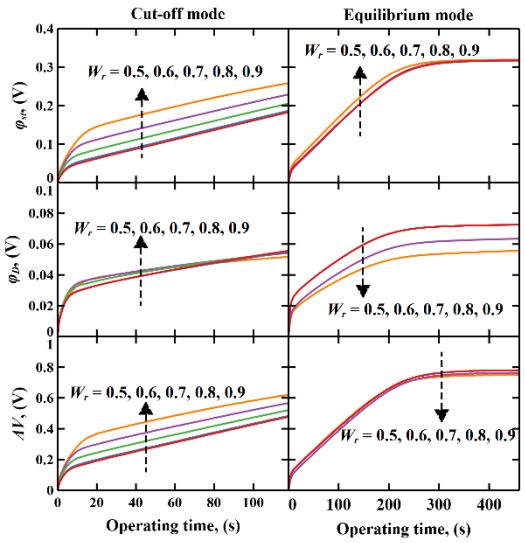

Figure A.3. Transient Stern layer potential drop and Donnan potential of one electrode, and the accumulated potential in EDL of both electrodes in desalination step of the fifth cycle in both cut-off mode and equilibrium mode with water recovery of 0.5, 0.6, 0.7, 0.8, and 0.9. Applied voltage is 0.8 V, and cell length is 10 cm.

Stern layer potential drop is much higher than Donnan potential. Stern layer potential drop increases significantly with increasing water recovery in cut-off mode. This is due to the incomplete desorption of the electrode during regeneration at high water recovery, resulting in a relatively high total charge at the beginning of next desalination step.

Donnan potential decreases with increasing water recovery in equilibrium mode but does not show significant changes in cut-off mode. The accumulated potential in EDL increases with increasing water recovery in cut-off mode, and decreases marginally with increasing water recovery in equilibrium mode.

A.3 Comparisons of pressure drop between MCDI and ED channels

Pressure drop through a porous spacer can be calculated by Eq. (4.13). ED mainly uses an open channel or a channel assembled with mechanical spacers [1]. Pressure drop through an open channel is given by [2]:

$$\Delta P = \frac{12\mu QL}{{L_{ch}}^2 A_c} \tag{A.1}$$

where μ is the viscosity of the feed water, Q is the flow rate, L is the channel length, L_{ch} is the channel thickness, and A_c is the cross-sectional area, which is the multiplication of channel thickness and channel width. Pressure drop through a channel with a mechanical spacer is given by [2]:

$$\Delta P = \frac{12\mu QL}{\frac{1}{4}d_{ch}^2 \varepsilon_s A_c} \tag{A.2}$$

where ε_s is the porosity of the spacer-filled channel, and d_{ch} is the modified channel hydraulic diameter, which is given by:

$$d_{ch} = \frac{4\varepsilon_s}{\frac{2}{L_{ch}} + (1-\varepsilon_s)\frac{8}{L_{ch}}} \tag{A.3}$$

Pressure drop increases with increasing channel length, flow rate and porosity, and decreasing width and thickness of the channel in all the three types of channels. Under

a fixed flow rate and channel geometry, the ratio of pressure drop through each channel only depends on porosity, channel thickness and permeability, which is a function of porosity and critical pore size or fiber radius. Here, we assume that fibrous porous media with fiber radius of 3.5×10^{-3} mm are used, so permeability is only related to porosity.

Pressure drops through an open channel, a channel with mechanical spacer, and a channel with porous media spacer versus porosity of the spacer-filled channel, channel thickness, flow rate and channel length are displayed in Figure A.4.

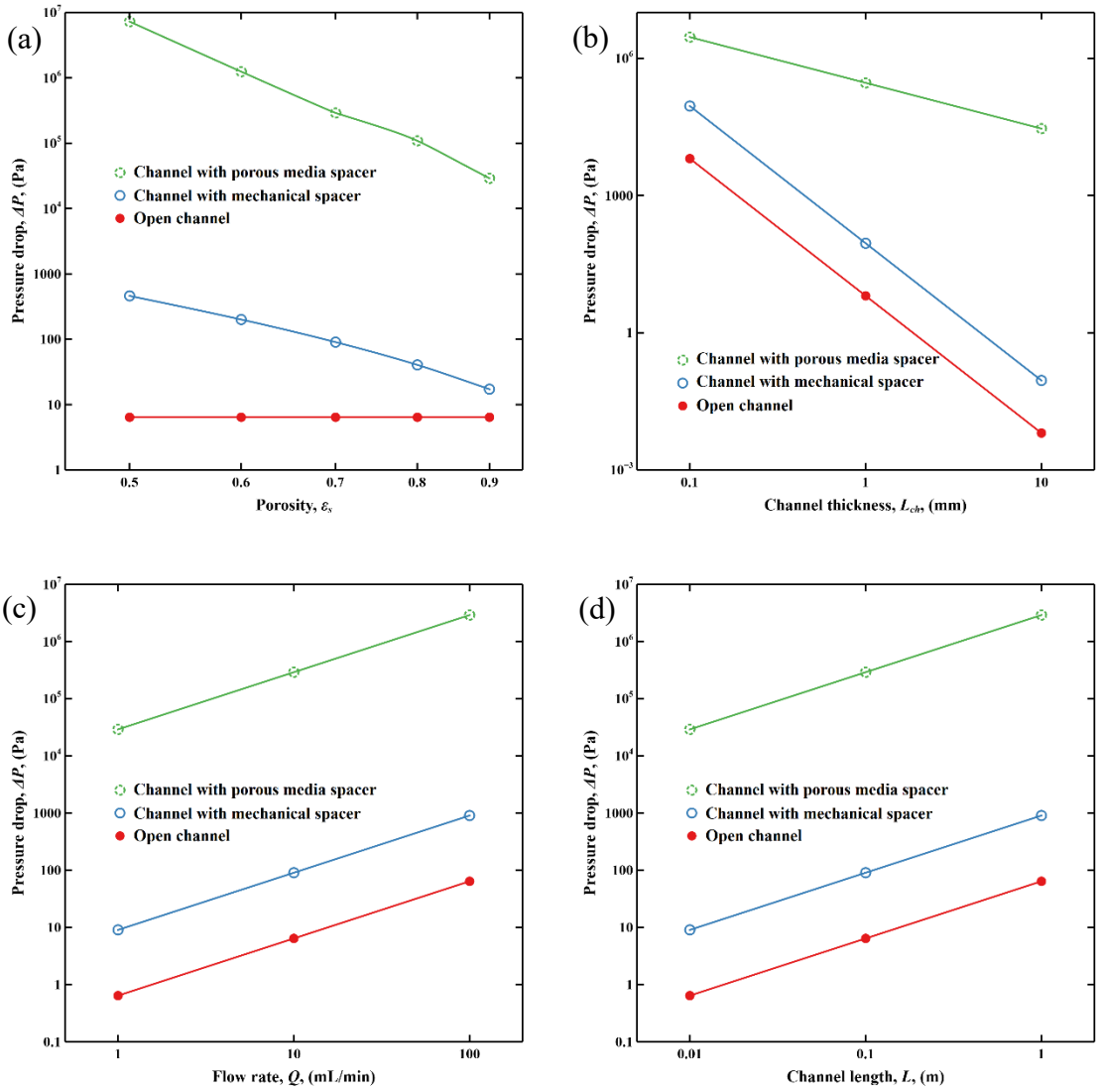

Figure A.4. Pressure drop through an open channel, a channel with mechanical spacer, and a channel with porous media spacer versus (a) porosity of 0.5, 0.6, 0.7, 0.8 and 0.9 with channel thickness of 1 mm, flow rate of 10 mL/min and channel length of 0.1 m; (b) channel thickness of 0.1 mm, 1 mm, and 10 mm with porosity of 0.7, flow rate of 10 mL/min and channel length of 0.1 m; (c) flow rate of 1 mL/min, 10 mL/min and 100 mL/min with porosity of 0.7, channel thickness of 1 mm and channel length of 0.1 m; (d) channel length of 0.01 m, 0.1 m and 1 m with porosity of 0.7, channel thickness of 1 mm and flow rate of 10 mL/min. Channel width is set as 0.1 m for all the cases. Lines are used for guiding the eyes.

Pressure drop through porous media spacer is several orders of magnitude higher compared to that of a channel with mechanical spacer and open channel. Improving porosity significantly reduces the pressure drop through the spacer. The pressure drop through channel with mechanical spacer is generally an order of magnitude higher than that of an open channel with a porosity of 0.7. Enlarging channel thickness significantly brings down the pressure drops through channel with mechanical spacer and open channel to negligible values, but does not exert that much effect on the pressure drop through channel with porous media spacer. Varying flow rates and channel lengths have similar effects on pressure drops of all the three types of channels. Overall, the pressure drop of channel with porous media spacer is high compared to that of channel with mechanical spacer or open channel, especially under high flow rate, long channel length and thin channel thickness. This limits the scale-up of MCDI. Hence, spacer materials with high porosity and large critical pore size or large fiber radius to significantly reduce the permeability are urged to be synthesized and applied in MCDI to address the high pressure drop challenge.

A.4 References

[1] Y. Kim, W. S. Walker, and D. F. Lawler, "Electrodialysis with spacers: effects of variation and correlation of boundary layer thickness," *Desalination,* vol. 274, no. 1, pp. 54-63, 2011.

[2] S. Pawlowski, J. G. Crespo, and S. Velizarov, "Pressure drop in reverse electrodialysis: Experimental and modeling studies for stacks with variable number of cell pairs," *Journal of Membrane Science,* vol. 462, pp. 96-111, 2014.

APPENDIX B

SUPPORTING INFORMATION FOR CHAPTER 5

B.1 Transient effluent concentration curves of cations in K^+-Na^+-Cl^- solution with and without considering ion excluded volume effects

Transient effluent concentration curves of cations with and without ion excluded volume effects during desalination in (M)CDI are displayed in Figure B.1. In K^+-Na^+-Cl^- solution, CDI approaches equilibrium within 400 s, which is almost twice as much as that of MCDI. However, Ca^{2+}-Na^+-Cl^- solution takes longer time to reach equilibrium due to the competitive substitution of Na^+ by Ca^{2+} even after electrode saturation is achieved. Transient effluent concentration curves with and without considering ion excluded volume effects have negligible deviations in both CDI and MCDI. The transport and adsorption rate of K^+ is a bit faster compared to that of Na^+ in CDI but is almost the same as that of Na^+ in MCDI. This is due to the equally enhanced transport rate of both cations through IEM due to the same valence of K^+ and Na^+.

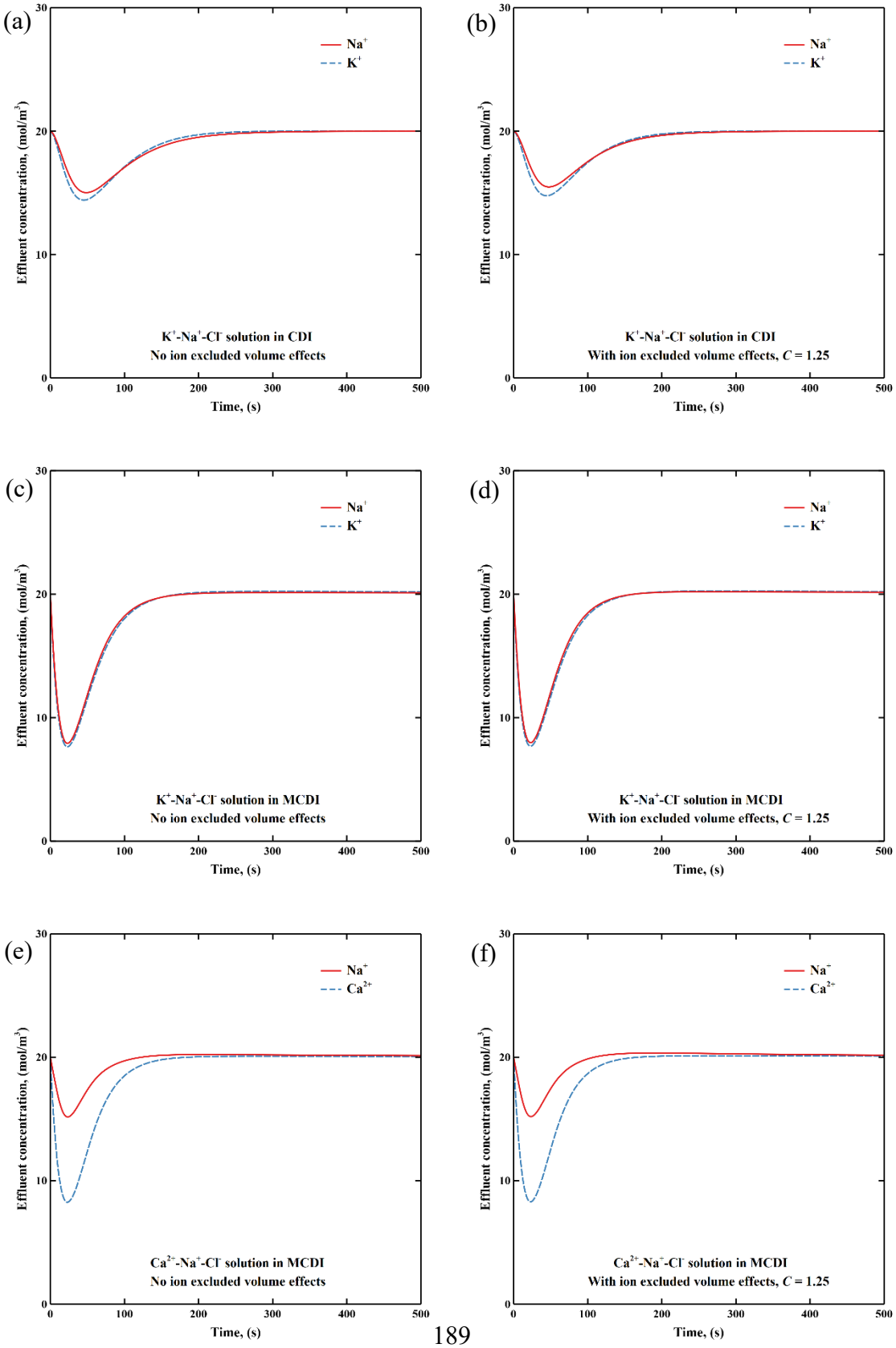
(a)
Na+
K+
Effluent concentration, (mol/m3)
K+-Na+-Cl- solution in CDI
No ion excluded volume effects
Time, (s)
(b)
Na+
K+
Effluent concentration, (mol/m3)
K+-Na+-Cl- solution in CDI
With ion excluded volume effects, C = 1.25
Time, (s)
(c)
Na+
K+
Effluent concentration, (mol/m3)
K+-Na+-Cl- solution in MCDI
No ion excluded volume effects
Time, (s)
(d)
Na+
K+
Effluent concentration, (mol/m3)
K+-Na+-Cl- solution in MCDI
With ion excluded volume effects, C = 1.25
Time, (s)
(e)
Na+
Ca2+
Effluent concentration, (mol/m3)
Ca2+-Na+-Cl- solution in MCDI
No ion excluded volume effects
Time, (s)
(f)
Na+
Ca2+
Effluent concentration, (mol/m3)
Ca2+-Na+-Cl- solution in MCDI
With ion excluded volume effects, C = 1.25
Time, (s)

Figure B.1. Transient effluent concentration curves of cations in K+-Na+-Cl- solution in CDI (a) without ion excluded volume effects, (b) with ion excluded volume effects (C = 1.25); Transient effluent concentration curves of cations in K^+-Na^+-Cl^- solution in MCDI (c) without ion excluded volume effects, (d) with ion excluded volume effects (C = 1.25); Transient effluent concentration curves of cations in Ca^{2+}-Na^+-Cl^- solution in MCDI (e) without ion excluded volume effects, (f) with ion excluded volume effects (C = 1.25); Applied voltage is 0.3 V. Feed concentration of each cation is 20 mol/m^3.

B.2 Transient effluent concentration curves of cations in Ca^{2+}-Na^+-Cl^- solution under varying applied voltage

The simulated transient effluent concentration curves of cations in Ca^{2+}-Na^+-Cl^- solution under varying applied voltage of 0.1 V, 0.2 V and 0.3 V during desalination in MCDI are displayed in Figure B.2. The adsorption amount of both cations increase with the increasing applied voltage due to the increased adsorption capacity of the electrode. The adsorption amount of Ca^{2+} is much higher than Na^+. The effluent concentration of Na^+ goes slightly beyond its initial concentration when electrode saturation is approached, indicating the occurrence of a competitive substitution of Na^+ by Ca^{2+}. This phenomena is more significant under a higher applied voltage.

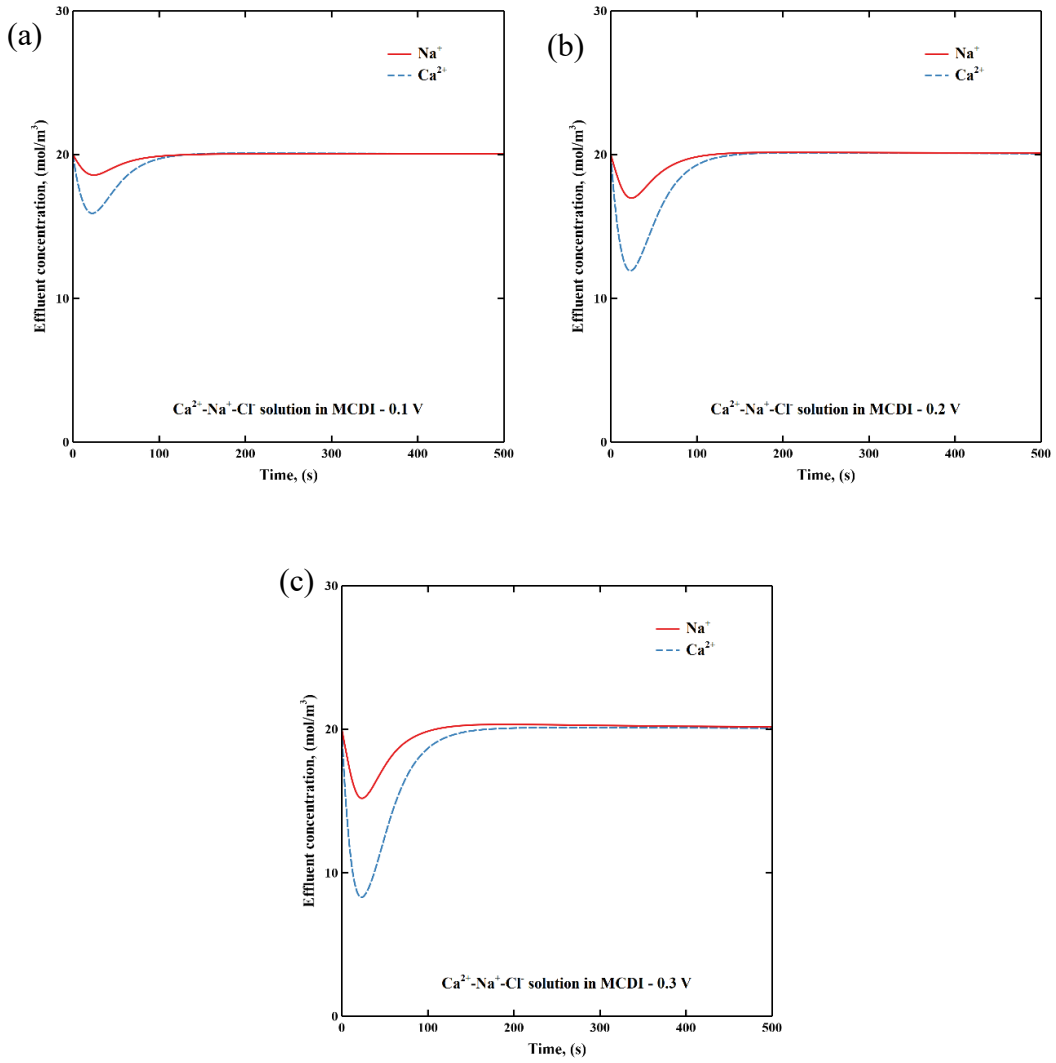

Figure B.2. Simulated transient effluent concentration curves of cations in Ca^{2+}-Na^{+}-Cl^{-} solution under varying applied voltage of (a) 0.1 V, (b) 0.2 V, and (c) 0.3 V during desalination in MCDI. The adjustable variable *C* is set to 1.25. Feed concentration of each cation ion is 20 mol/m^3.

B.3 Transient effluent concentration curves of cations in Ca^{2+}-Na^{+}-Cl^{-} solution under varying initial concentration ratios of cations

The simulated transient effluent concentration curves of cations in Ca^{2+}-Na^{+}-Cl^{-} solution under varying initial concentration ratios of cations during desalination in MCDI are displayed in Figure B.3. The initial concentration ratio of cations is tuned by adjusting the feed concentration of Ca^{2+} from 20 mol/m^3 to 2 mol/m^3 and fixing the feed concentration of Na^{+} at 20 mol/m^3 at the same time. As the initial concentration ratio of Na^{+} to Ca^{2+} increases, the adsorption amount of Na^{+} increases, while the adsorption amount of Ca^{2+} decreases. Meanwhile, the competitive substitution of Na^{+} by Ca^{2+} becomes severe, resulting in a longer time for Na^{+} to return to its initial concentration. Hence, the final equilibrium will be reached after a very long time.

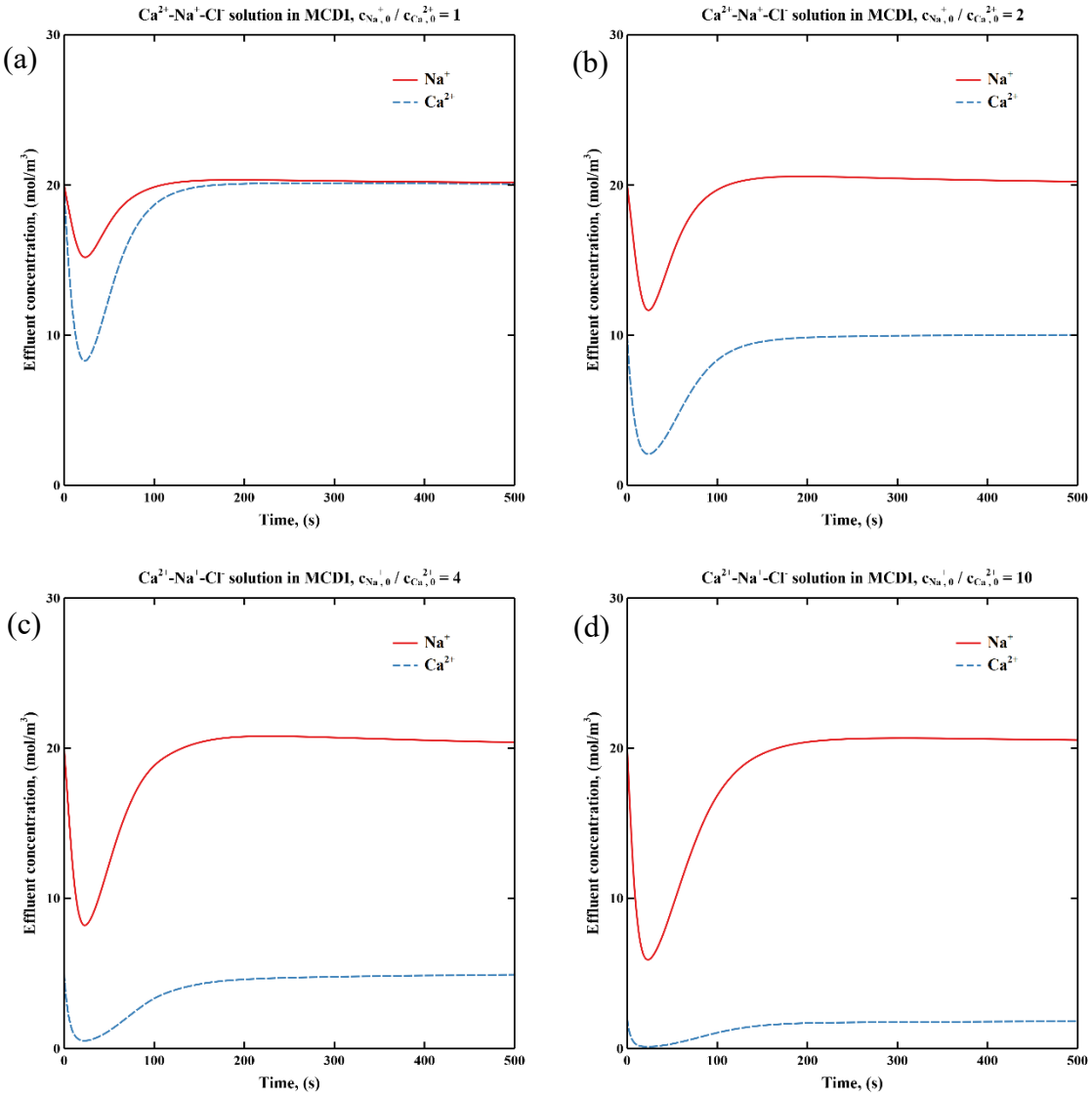

Figure B.3. Simulated transient effluent concentration curves of cations under varying initial concentration ratios of cations at (a) $c_{Na^+,0}/c_{Ca^{2+},0} = 1$, (b) $c_{Na^+,0}/c_{Ca^{2+},0} = 2$, (c) $c_{Na^+,0}/c_{Ca^{2+},0} = 4$ and (d) $c_{Na^+,0}/c_{Ca^{2+},0} = 10$ in Ca^{2+}-Na^+-Cl^- solution during desalination in MCDI. The adjustable variable C is set to 1.25. Applied voltage is 0.3 V.

B.4 Transient effluent concentration curves of cations and anions in MCDI when softening industrial cooling tower blowdown water and domestic tap water

The simulated transient effluent concentration curves of cations and anions in five consecutive cycles containing Na^+, Ca^{2+}, Cl^-, NO_3^- and SO_4^{2-} under varying water recovery from 0.3 to 0.7 in cut-off CV mode MCDI for softening industrial cooling tower blowdown water are displayed in Figure B.4. A full cycle includes a desalination step followed by a regeneration step. In this study, the regeneration of MCDI is operated by short-circuiting the cell. MCDI reaches quasi-steady state within five consecutive cycles. Water recovery is tuned by adjusting the operating time of regeneration step and fixing the flow rate for both desalination and regeneration steps. As water recovery increases, the desalination capacity of MCDI decreases due to the aggravating incomplete regeneration of the electrodes, causing a decreased adsorption of all the ions. The effects of water recovery on ion adsorption amount are more severe on monovalent ions compared to divalent ions.

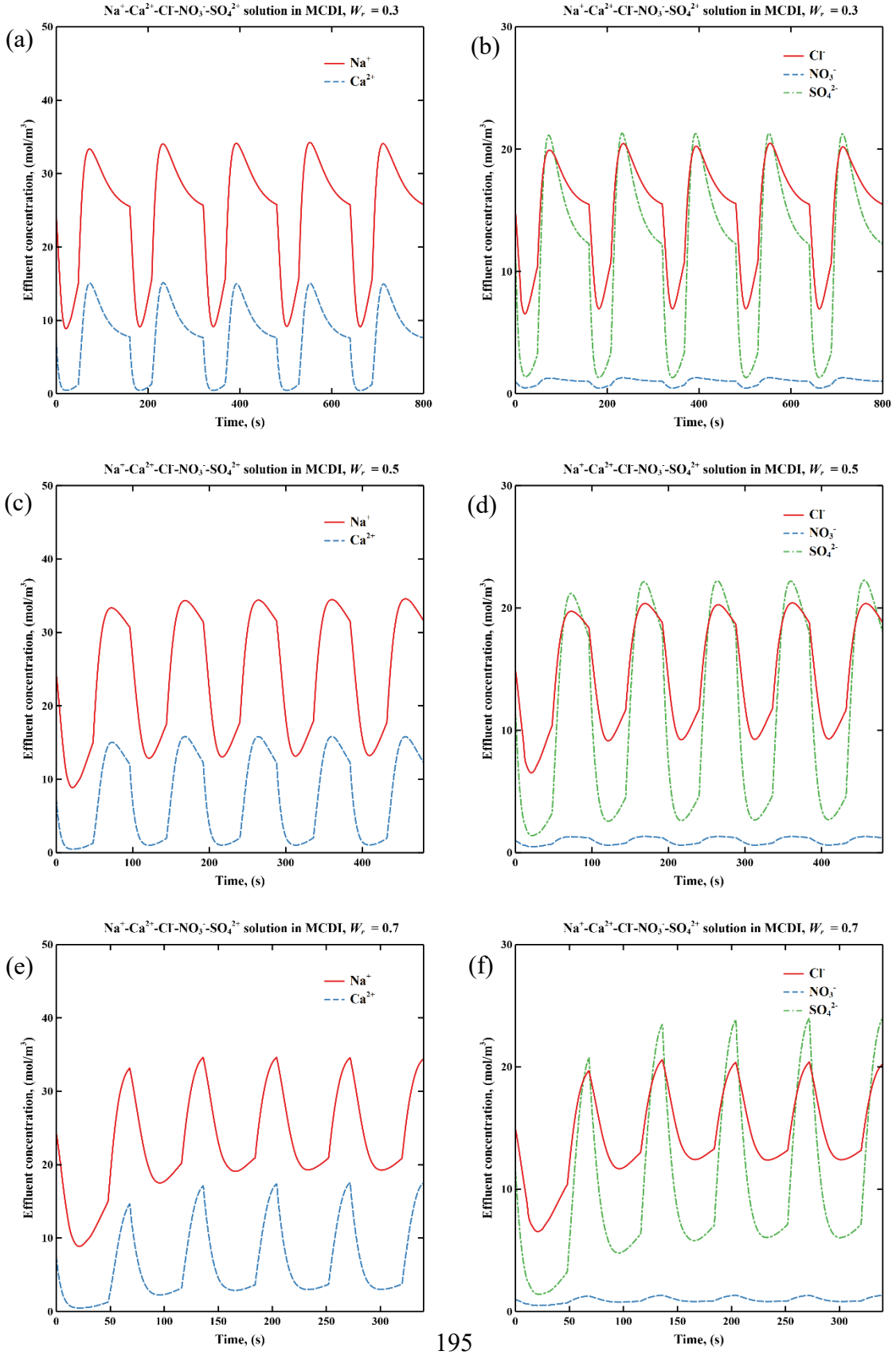
(a)
Na+-Ca2+-Cl--NO3--SO42+ solution in MCDI, Wr = 0.3
Na+
Ca2+
Effluent concentration, (mol/m3)
Time, (s)
(b)
Na+-Ca2+-Cl--NO3--SO42+ solution in MCDI, Wr = 0.3
Cl-
NO3-
SO42-
Effluent concentration, (mol/m3)
Time, (s)
(c)
Na+-Ca2+-Cl--NO3--SO42+ solution in MCDI, Wr = 0.5
Na+
Ca2+
Effluent concentration, (mol/m3)
Time, (s)
(d)
Na+-Ca2+-Cl--NO3--SO42+ solution in MCDI, Wr = 0.5
Cl-
NO3-
SO42-
Effluent concentration, (mol/m3)
Time, (s)
(e)
Na+-Ca2+-Cl--NO3--SO42+ solution in MCDI, Wr = 0.7
Na+
Ca2+
Effluent concentration, (mol/m3)
Time, (s)
(f)
Na+-Ca2+-Cl--NO3--SO42+ solution in MCDI, Wr = 0.7
Cl-
NO3-
SO42-
Effluent concentration, (mol/m3)
Time, (s)

Figure B.4. Simulated transient effluent concentration curves of cations under water recovery of (a) 0.3, (c) 0.5, and (e) 0.7, respectively, and anions under water recovery of (b) 0.3, (d) 0.5, and (f) 0.7, respectively, in five consecutive cycles in cut-off CV mode MCDI when softening industrial cooling tower blowdown water. The adjustable variable *C* is set to 1.25. Applied voltage is 0.4 V.

The simulated transient effluent concentration curves of cations and anions in five consecutive cycles containing Na^+, Ca^{2+}, K^+, Mg^{2+} and Cl^- under varying water recovery from 0.5 to 0.7 in cut-off CV mode MCDI for softening domestic tap water are displayed in Figure B.5. MCDI reaches quasi-steady state within five consecutive cycles. The concentrations of ionic species in domestic tap water are much smaller compared to those in industrial cooling tower blowdown water. So a small applied voltage can meet the requirement of partial desalination. In this case study, the increase of water recovery also reduces ion adsorption amount due to the aggravating incomplete regeneration of the electrodes from the shortened operating time during regeneration.

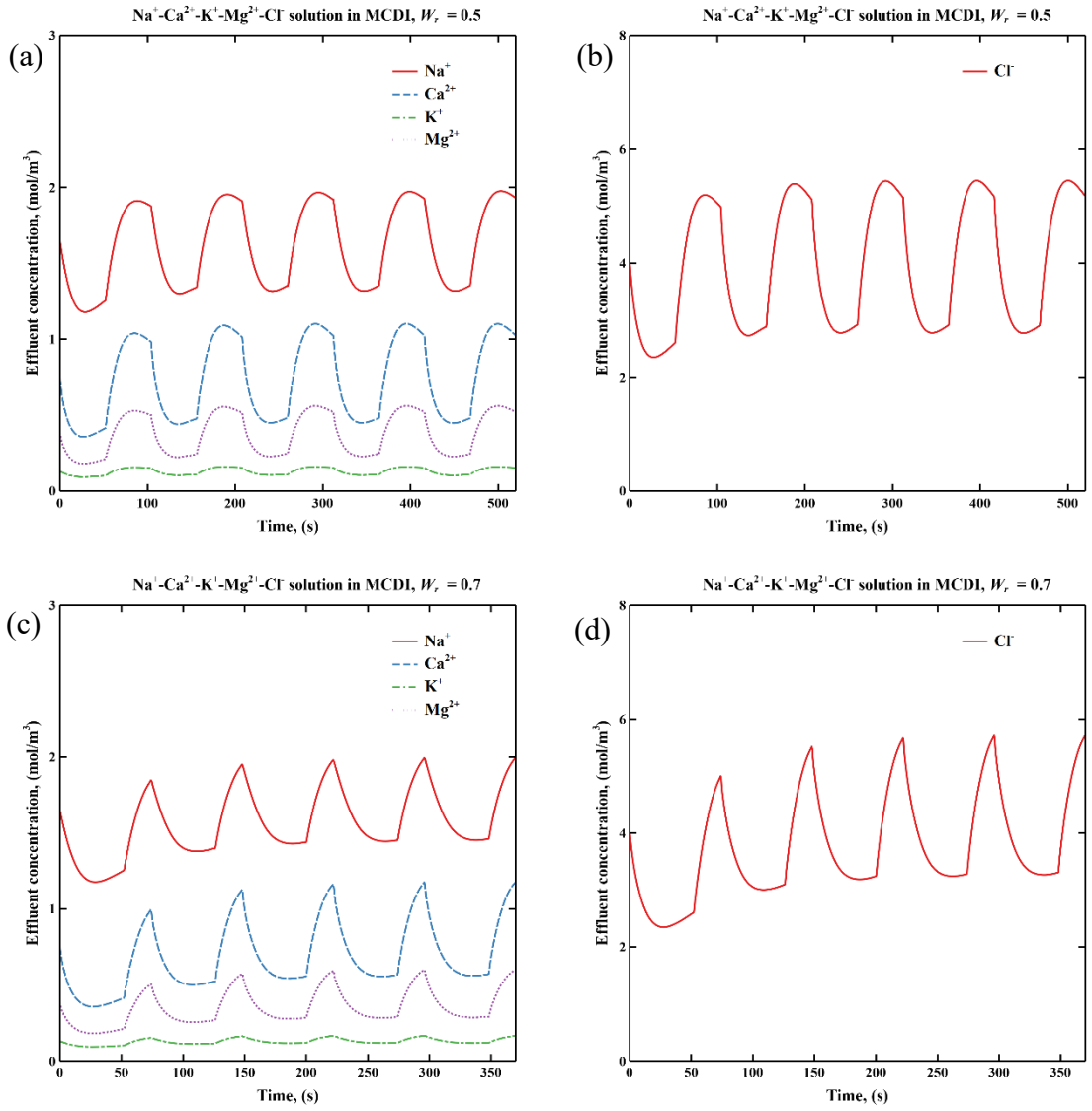

Figure B.5. Simulated transient effluent concentration curves of cations under water recovery of (a) 0.5 and (c) 0.7, and anions under water recovery of (b) 0.5 and (d) 0.7, in five consecutive cycles in cut-off CV mode MCDI for softening domestic tap water. The adjustable variable *C* is set to 1.25. Applied voltage is 0.08 V.

B.5 Energy consumption components of MCDI

The source of energy consumption in MCDI include energy consumed for charging the electrodes and pumping the flowing solution. In this study, the components of energy

consumption include pump losses, external resistive losses and cell pair energy consumption, and are expressed as a specific energy consumption (SEC) form by dividing the volume of product water.

Pump losses represent the pump energy used for pumping feed water through the porous spacer-filled channel in both desalination and regeneration steps. Energy consumption of pump is given by:

$$E_{pump} = \frac{\sum_{j=d,r} \Delta P_j Q_j t_j}{Q_d t_d} \tag{B.1}$$

where ΔP_j, Q_j, and t_j are the pressure drop through the channel, flow rate, and operating time of operating step, j, including desalination step, d, and regeneration step, r, respectively.

Pressure drop through the porous channel is given by:

$$\Delta P_i = \frac{\mu Q_i L}{k A_c} \tag{B.2}$$

Where μ is the viscosity of feed water, L is the cell length, k is the permeability of the porous spacer, and A_c is the cross-sectional area of the channel, width times thickness ($W \times L_{ch}$).

External resistive losses account for energy losses on contact resistance between current collector and electrode, wire resistance and current collector resistance, and can be expressed by:

$$E_{ext} = \frac{\int_0^{t_d} I_{ext}^2 R_{ext} dt}{Q_d t_d} \tag{B.3}$$

Energy consumed in cell pairs is used for ion transport and adsorption in the cell, and is given by:

$$E_{cell} = E_{eps} - E_{ext} = \frac{\int_0^{t_d} V_{cell} I_{ext} dt}{Q_d t_d} - E_{ext} \quad \text{(B.4)}$$

where V_{cell} is the applied voltage including the potential drop on the external resistance and the cell pair.

The total SEC is the sum of the three components mentioned above:

$$SEC = E_{pump} + E_{ext} + E_{cell} \quad \text{(B.5)}$$

Along with ion adsorption, part of the input energy is temporarily stored in EDL. This energy is the maximum recoverable energy and can be partially harvested during regeneration. This energy storage amount is given by [1]:

$$E_{EDL} = \frac{\int_0^{t_d} I_{ext}(\varphi_{st}+\varphi_D) dt}{Q_d t_d} \quad \text{(B.6)}$$

where φ_{st} is the Stern layer potential drop, and φ_D is the Donnan potential.

B.6 References

[1] Y. Salamat and C. H. Hidrovo, "A parametric study of multiscale transport phenomena and performance characteristics of capacitive deionization systems," *Desalination,* vol. 438, pp. 24-36, 2018.